SANDIA REPORT
SAND2002-8008
Unlimited Release
Printed January 2002

Crack Nucleation and Growth: Combined Validated Atomistic and Continued Modeling

J. A. Zimmerman, P. A. Klein, E. P. Chen, R. Q. Hwang, J. C. Hamilton,
J. E. Houston, S. M. Foiles

Prepared by
Sandia National Laboratories
Albuquerque, New Mexico 87185 and Livermore, California 94550

Sandia is a multiprogram laboratory operated by Sandia Corporation,
a Lockheed Martin Company, for the United States Department of
Energy under Contract DE-AC04-94AL85000.

Issued by Sandia National Laboratories, operated for the United States Department of Energy by Sandia Corporation.

Available to DOE and DOE contractors from
U.S. Department of Energy
Office of Scientific and Technical Information
P.O. Box 62
Oak Ridge, TN 37831

Telephone: (865)576-8401
Facsimile: (865)576-5728
E-Mail: reports@adonis.osti.gov
Online ordering: http://www.doe.gov/bridge

Available to the public from
U.S. Department of Commerce
National Technical Information Service
5285 Port Royal Rd
Springfield, VA 22161

Telephone: (800)553-6847
Facsimile: (703)605-6900
E-Mail: orders@ntis.fedworld.gov
Online order: http://www.ntis.gov/ordering.htm

SAND2002-8008
Unlimited Release
Printed January 2002

Crack Nucleation and Growth: Combined Validated Atomistic and Continuum Modeling

J.A. Zimmerman P.A. Klein E.P. Chen
Science-based Materials Modeling Department

R.Q. Hwang J.C. Hamilton
Thin-Film & Interface Science Department

Sandia National Laboratories
P.O. Box 969
Livermore, CA 94551

J.E. Houston
Surface & Interface Science Department

S.M. Foiles
Materials & Process Modeling Department

Sandia National Laboratories
P.O. Box 5800
Albuquerque,NM 87158

Abstract

Ductile and brittle fracture are critical material failure modes that impact areas ranging from advanced system development to the aging of stockpile components. Consequently, computational models of these processes are essential to Sandia's programmatic interests. The wide range of length scales involved has dramatically hampered the computer modeling of fracture. For example, ductile fracture involves the interactions between dislocations (defects in the atomic crystal lattice) and crack tips, producing long-range elastic forces at micro- and macroscopic scales. Similarly, brittle fracture entails atomic and molecular bond breaking caused by the concentration of stress fields at the crack tip, where the origin of these stresses is at remote boundaries. Thus, it is imperative to couple the atomistic understanding provided by solid-state physics with the stress analysis provided by continuum mechanics. We have conducted a coordinated project in which experimental investigation of prototypical fracture events guides the use of atomistic and continuum modeling techniques. Our goals are to achieve a common working vocabulary that merges the ideas of atomistic and continuum analyses, to determine the areas in which continuum models need to be enriched to reflect atomic-scale processes, and to validate these methods by comparison with nano-scale experiments.

We began by investigating the relationship between atomic-level processes and the longer-range behavior of the stress field present during nanoindentation near steps on a metal surface. Our motivation is to examine defect nucleation requiring a stress concentration. The stress concentration at the step is by its nature an atomic-level property while the behavior of the stress field away from the step is better characterized by a continuum approach. How the plastic yield of the metal is affected by a stress applied by a neighboring indenter will help us understand the interplay between the atomic- and continuum-level effects. Efforts were then made to study nanoindentation of a brittle material, usually resulting in the development of cracks within the material that possess specific, characteristic shapes. Atomistic simulation of nanoindentation of an ionic crystal, MgO, has been performed, as have experiments on that same material. We have also analyzed and compared the static and dynamic responses of atomistic and continuum models of steady-state, 2-dimensional crack propagation. This model problem allowed us to characterize the inherent traits of the two simulation methods, and identify specific directions in which continuum simulation needs to be enhanced.

Keywords: Brittle fracture, dislocations, atomistic simulation, nanoindentation, cohesive modeling.

Contents

List of Figures

List of Tables

This page intentionally left blank.

Chapter 1

Introduction

Ductile and brittle fracture are critical material failure modes which impact areas ranging from advanced system development to the aging of stockpile components. Consequently, computational models of these processes are essential to Sandia's programmatic interests. Indeed, the current goal of materials engineering is to develop computational methods capable of duplicating and predicting various modes of defect nucleation and evolution. The wide range of length scales involved has been the primary obstacle to predictive modeling of fracture. For example, ductile fracture in crystalline materials involves the interactions between dislocations, line imperfections within an otherwise perfect crystal lattice, and crack tips, producing long-range elastic forces at micro- and macroscopic scales. Similarly, brittle fracture entails atomic and molecular bond breaking caused by the concentration of stress fields at a crack tip, where the origin of these stresses is at remote boundaries. Methods used to analyze such material defects operate at specific length-scale regimes. Macroscopic dimensions (1 mm to 10 m) are modeled using classical continuum plasticity methods while the mesoscopic regime (100 μm to 1 cm) is well suited to crystal plasticity constitutive relations. Microscopic features (0.1 to 10 μm) can be analyzed with dislocation dynamics, and nanoscopic structures (1 Å to 100 nm) can only be treated fully with atomistic simulation. Thus, it is imperative to couple the atomistic understanding provided by solid-state physics to the stress analysis provided by continuum mechanics.

We have completed a coordinated project in which experimental investigation of prototypical fracture events was used to guide modeling using atomistic and continuum techniques. Our goals were to achieve a common working vocabulary that merged the ideas of atomistic and continuum analyses, to determine the areas in which continuum models need to be enriched to reflect atomic-scale processes, and to validate these methods by comparison with nano-scale experiments.

We have obtained nanoindentation results with the interfacial force microscope (IFM) exploring the plastic yield threshold for Au(111) single-crystal surfaces as a function of the distance to neighboring surface steps. These studies involved obtaining constant force images of the surface in order to establish the location and properties of steps on the Au surface. We have created loading curves, *i.e.* measurements of indentation force *vs.* relative displacement,

with a parabolic probe and identify the onset of plastic yield by the deviation of the loading curve from the classic Hertzian behavior. Values for the yield stress and the contact area at yield are then tabulated, along with the height of the step, as a function of the distance from the tip center to the step edge. We find that on broad terraces the average yield stress is 7 GPa approaching the theoretical strength of the Au lattice. However when the probe is placed at the step edge, the yield stress is reduced by almost a factor of two. The surface step represents a very controllable defect. Surprisingly, we find that the reduction of the yield stress by the neighboring step extends over a range of approximately three times the contact radius at yield.

Quasistatic atomistic simulations of a Au(111) surface with a step provided insight into dislocation nucleation during nanoindentation. The results are similar to those seen in nanoindentation experiments, although length-scale differences result in subtle contrasts. The "long-range" effect observed in experiments is discovered to originate from contact between the indenter and the step edge. A geometric expression was developed which predicts results in both atomistic simulation and experiments. We developed a new simulation metric, the slip vector, to identify the Burgers vector content of the dislocation structures that form. Combining the precise direction of slip with a locally defined atomic stress tensor permits calculation of the resolved shear stress needed for dislocation nucleation. We compared stress fields in the atomistic simulation with those in a finite element calculation using a constitutive model derived from the same interatomic potential. The fields agree well quantitatively.

We have performed further validation of our atomistic models by comparing additional nanoindentation simulations with recent experiments showing the formation of sub-Å height hillocks on Scanning Tunnelling Microscope (STM) indented, Au(001) surfaces. These hillocks are positioned at significant distances away from the indentation region. It has been theorized that these hillocks are produced by the dissociation of V-shaped dislocation loops that form, and then propagate away from the indentation region [2]. Atomistic simulation confirms this sub-surface structure and connects the hillocks to the underlying stacking faults bounded by the dissociated partial dislocations. The heights of the hillocks observed in simulation, approximately 0.6 Å, are in agreement with experimental measurements.

We have developed an atomistic simulation code capable of modeling ionic crystals. This code uses a charge-neutralization, truncated-radius formalism to evaluate the Coulomb portion of the interatomic potential. Simulations of the nanoindentation of MgO exhibit Hertzian behavior and a critical load at which material failure occurs. Images of these simulations do not display dislocation structures, but further analysis is needed to clarify if any material defects are created. For comparison, nanoindentation experiments using a diamond-tip indenter were performed; however, irregular behavior in the loading curve, failure to detect any defect formation, and SEM examination of the indenter suggests the tip used possessed a complex shape resulting in a larger than expected tip radius.

We have qualitatively and quantitatively analyzed and compared the static and dynamic responses of atomistic and continuum models of steady-state, 2-dimensional crack propagation. The parameters for the two material models are selected to produce identical elastic modulus, fracture energy and cohesive strength, derived from a standard interatomic poten-

tial. Under quasistatic loading, the two models possess nearly identical traction distributions on the cleavage plane and fail due to brittle fracture at the same crack driving force. However, whereas dynamic loading of the continuum model results in brittle cleavage, the response of the atomistic model is strain-rate dependent and displays multiple mechanisms of dissipation such as material vibration and, at high strain-rates, dislocation emission. A detailed analysis of the two models exhibiting brittle cleavage shows the continuum crack accelerating to the continuum limiting speed of the Rayleigh wave speed. In contrast, the atomistic crack reaches a speed of one fifth this value, and then propagates at constant speed. The rate of kinetic energy generation increases proportionately to the applied strain in the atomistic model, while this rate vanishes for the continuum model as the limiting speed is approached. For the atomistic simulation, Fourier spectral analysis of displacements perpendicular to the cleavage plane for atoms in front of, and behind, the crack tip shows that the moving crack concentrates kinetic motion to a specific wavelength approximately five times the lattice parameter. Reduction of the interaction range of the interatomic potential produces only slight alterations of both the terminal crack speed and the concentration wavelength. We conclude that a local continuum description does not or cannot produce dispersive behavior. The addition of dissipation mechanisms for the energy converted into "heat" does not make the cohesive simulations behave like the atomistics.

Chapter 2 will present the atomistic and continuum simulation methods used for this research. Chapter 3 will discuss our atomistic modeling of nanoindentation of Au(111) and Au(001). Chapter 4 will show our first attempt to examine failure of a brittle material, specifically sodium silicate glass. In Chapter 5, our computational and experimental research on the nanoindentation of MgO will be discussed. Chapter 6 will present our study of 2-dimensional steady-state crack growth using atomistic and continuum methodologies. Finally, in Chapter 7, we summarize our findings and present a list of publications produced as a result of this research.

This page intentionally left blank.

Chapter 2

Simulation Methods

Use of particle simulation methods is widespread in today's age of computational materials analysis. There are many research problems in the study of both fluids and solids which require examination of the behavior of individual particles, in place of the continuum mechanical approach of treating a material as a continuous and homogeneous medium. Such work includes study of the mechanics of fracture at a crack tip [3, 4, 5, 6, 7] as well as the effect of defects such as dislocations, vacancies, interstitials, voids and inclusions on mechanical behavior.

A more common approach to materials simulation is the use of continuum mechanics. Modern continuum simulations consist of material models that are cohesive in nature, *i.e.* the constitutive model is based on a traction-separation relation, and described by a finite work of separation a maximum value of stress for material response. This allows the natural evolution of material failure rather than by introducing a separate, phenomenological failure criterion. Two such cohesive approaches are Cauchy-Born elasticity and the use of cohesive surfaces.

The first section of this chapter will explain the methods of atomistic simulation used for this project, including molecular dynamics (MD) and energy minimization using the conjugate gradient (CG) algorithm. This section will also discuss boundary conditions, particle ensembles and neighbor lists. A listing of interatomic potentials will be presented showing the different empirical models available and used for this work. The second section of this chapter will present the cohesive continuum mechanical models used in this project.

2.1 Atomistic Simulation

This section will discuss the computational techniques used for simulations of material deformation at the atomic scale. Among the important concepts to understand are the time step limitations, the type of boundary conditions applied to the system, isothermal versus adiabatic simulations, and interatomic potential models.

2.1.1 Molecular dynamics

Molecular dynamics is perhaps the most straightforward type of simulation method used by researchers to analyze materials problems. It involves deriving the equations of motion for a system comprised of a large number of particles, which results in a set of coupled ordinary differential equations, and solving these equations by discretization of time and approximation of time derivatives. The governing equation of motion is Newton's 2^{nd} law,

$$F_i^\alpha = m_\alpha \ddot{x}_i^\alpha. \tag{2.1}$$

In this expression, F_i^α denotes the force in the i^{th} direction acting on particle α, m_α denotes that particle's mass, and x_i^α denotes the i^{th} component of the particle's position. The notation $\ddot{z}$ is equivalent to the second time derivative, $\frac{d^2z}{dt^2}$, of the variable z. As a convention, lower case roman letters (i, j, k) denote a Cartesian coordinate direction ($i = 1, 2, 3$) and lower case greek letters (α, β) denote the number designation for a particle belonging to a system of N particles.

The equations of motion can also be derived using more advanced methods such as Hamiltonian dynamics. This type of mechanics uses a function of particle positions and momenta which is known to be constant for a particular system. Such is the case for an isolated system of particles in which that function, the Hamiltonian $\mathcal{H}$, is known to be the total (kinetic plus potential) energy of the system...

$$\mathcal{H} = \sum_{\alpha=1}^{N} \frac{p_k^\alpha p_k^\alpha}{2m_\alpha} + \mathcal{U}\left(\mathbf{x}^N\right) = E. \tag{2.2}$$

Here, p_k^α denotes the momentum of particle α in the k^{th} direction,

$$p_k^\alpha = m_\alpha \dot{x}_k^\alpha, \tag{2.3}$$

repeated occurrence of a Cartesian index implies summation over that index , $\mathcal{U}$ denotes the potential energy of the system of N particles and E is the total energy of the system, a constant. The differentiation of the Hamiltonian with respect to time, which equals zero, can be performed to derive two partial differential equations. The first equation,

$$\frac{\partial \mathcal{H}}{\partial p_j^\alpha} = \dot{x}_j^\alpha, \tag{2.4}$$

is just the relation defining momentum as the product of mass and velocity. The second equation,

$$\frac{\partial \mathcal{H}}{\partial x_j^\alpha} = -\dot{p}_j^\alpha, \tag{2.5}$$

reproduces Newton's 2^{nd} law (2.1) provided the force acting on particle α is conservative,

$$F_j^\alpha = -\frac{\partial \mathcal{U}}{\partial x_j^\alpha}, \tag{2.6}$$

which is true for an isolated system of particles.

The equation of motion (2.1) of particle α is coupled to the equations of motion of all the other particles in the system ($\beta = 1, 2, ..., \alpha-1, \alpha+1, ..., N$) through the conservative forces (2.6) present. Thus, a closed-form solution that defines the particle's motion for all time generally cannot be found. Instead, the coupled equations of motion are discretized in time and positions are found at a specific time step $t = n\Delta t$ based on positions and velocities at previous time steps. This is known as the finite-difference method. A commonly used finite-difference algorithm is the one developed by Gear [8, 9], which uses a Taylor series expansion with higher-order derivatives to predict future motion, relying on force calculations to correct these predictions. This algorithm has three steps. The first is to *predict* the position of an atom at the next time step by using a fifth-order Taylor series expansion about the atom's current values of position, velocity and acceleration:

$$x_i^\alpha(t+\Delta t) = x_i^\alpha(t) + \dot{x}_\alpha^i(t)\,\Delta t + \frac{1}{2!}\ddot{x}_i^\alpha(t)\,(\Delta t)^2 + \frac{1}{3!}\frac{d^3x_i^\alpha(t)}{dt^3}(\Delta t)^3 + \frac{1}{4!}\frac{d^4x_i^\alpha(t)}{dt^4}(\Delta t)^4 + \frac{1}{5!}\frac{d^5x_i^\alpha(t)}{dt^5}(\Delta t)^5 \tag{2.7}$$

$$\dot{x}_i^\alpha(t+\Delta t) = \dot{x}_\alpha^i(t) + \ddot{x}_i^\alpha(t)\,\Delta t + \frac{1}{2!}\frac{d^3x_i^\alpha(t)}{dt^3}(\Delta t)^2 + \frac{1}{3!}\frac{d^4x_i^\alpha(t)}{dt^4}(\Delta t)^3 + \frac{1}{4!}\frac{d^5x_i^\alpha(t)}{dt^5}(\Delta t)^4 \tag{2.8}$$

$$\ddot{x}_i^\alpha(t+\Delta t) = \ddot{x}_\alpha^i(t) + \frac{d^3x_i^\alpha(t)}{dt^3}\Delta t + \frac{1}{2!}\frac{d^4x_i^\alpha(t)}{dt^4}(\Delta t)^2 + \frac{1}{3!}\frac{d^5x_i^\alpha(t)}{dt^5}(\Delta t)^3 \tag{2.9}$$

$$\frac{d^3x_i^\alpha(t+\Delta t)}{dt^3} = \frac{d^3x_i^\alpha(t)}{dt^3} + \frac{d^4x_i^\alpha(t)}{dt^4}\Delta t + \frac{1}{2!}\frac{d^5x_i^\alpha(t)}{dt^5}(\Delta t)^2 \tag{2.10}$$

$$\frac{d^4x_i^\alpha(t+\Delta t)}{dt^4} = \frac{d^4x_i^\alpha(t)}{dt^4} + \frac{d^5x_i^\alpha(t)}{dt^5}\Delta t \tag{2.11}$$

$$\frac{d^5x_i^\alpha(t+\Delta t)}{dt^5} = \frac{d^5x_i^\alpha(t)}{dt^5} \tag{2.12}$$

The second step is to *evaluate* the forces on each atom, thus obtaining the true value of $\{\ddot{x}_i^\alpha(t+\Delta t)\}$. This provides the correction $\Lambda_i^\alpha = \left[\ddot{x}_i^\alpha(t+\Delta t) - \ddot{x}_i^{P,\alpha}(t+\Delta t)\right]$ where $\ddot{x}_i^{P,\alpha}(t+\Delta t)$ is the prediction calculated in (2.9). The final step is to *correct* each term in

the Taylor expansion by the factor:

$$x_i^\alpha(t+\Delta t) = x_i^{P,\alpha}(t+\Delta t) + \frac{1}{2!}\alpha_0 \Lambda_i^\alpha (\Delta t)^2 \tag{2.13}$$

$$\dot{x}_i^\alpha(t+\Delta t) = \dot{x}_i^{P,\alpha}(t+\Delta t) + \frac{1}{2!}\alpha_1 \Lambda_i^\alpha \Delta t \tag{2.14}$$

$$\ddot{x}_i^\alpha(t+\Delta t) = \ddot{x}_i^{P,\alpha}(t+\Delta t) + \alpha_2 \Lambda_i^\alpha \tag{2.15}$$

$$\frac{d^3 x_i^\alpha(t+\Delta t)}{dt^3} = \frac{d^3 x_i^{P,\alpha}(t+\Delta t)}{dt^3} + \frac{3!}{2!}\alpha_3 \Lambda_i^\alpha (\Delta t)^{-1} \tag{2.16}$$

$$\frac{d^4 x_i^\alpha(t+\Delta t)}{dt^4} = \frac{d^4 x_i^{P,\alpha}(t+\Delta t)}{dt^4} + \frac{4!}{2!}\alpha_4 \Lambda_i^\alpha (\Delta t)^{-2} \tag{2.17}$$

$$\frac{d^5 x_i^\alpha(t+\Delta t)}{dt^5} = \frac{d^5 x_i^{P,\alpha}(t+\Delta t)}{dt^5} + \frac{5!}{2!}\alpha_5 \Lambda_i^\alpha (\Delta t)^{-3} \tag{2.18}$$

where $\alpha_0 = \frac{3}{16}$, $\alpha_1 = \frac{251}{360}$, $\alpha_2 = 1$, $\alpha_3 = \frac{11}{18}$, $\alpha_4 = \frac{1}{6}$ and $\alpha_5 = \frac{1}{60}$.

It is necessary to know how large to make the time step Δt. Naturally, it would be desirable to have the time step be arbitrarily large, so phenomena that occur over any time scales could be modeled. However, the particle forces at a given time step are really average values over this increment, so the time step cannot be too large. This limitation is best seen by looking at the variation of the total energy of an isolated system. For such a system this variation should be identically zero, but realistically the variation will be finite with a monotonic dependence on the time step. The variation can be minimized by the use of double-precision arithmetic over single-precision when the time step is sufficiently small.

A further complication arises from the dimensional units of the system being simulated. When the time step is said to be "too large" or "too small", this has to be interpreted with respect to a characteristic value of time intrinsic to the material system. Such a dimensional factor of time is calculated from the quantity

$$\tau = \sigma\sqrt{\frac{m}{\epsilon}}. \tag{2.19}$$

In multi-particle systems where the particles are atoms, the values of σ, m and ϵ represent bond length, atomic mass, and cohesive energy of a bulk atom, respectively. The time step can then be expressed in the nondimensional form

$$\Delta t^* = \frac{\Delta t}{\tau}. \tag{2.20}$$

For this research a value of $\tau = 10^{-12}$ sec was chosen. Once this time scale is chosen, an analysis of the variation of system energy was performed to choose an acceptable value of Δt^*. Typically, this value was chosen to be between 0.0001 and 0.005, depending upon the choice of material.

2.1.2 Energy minimization

Although molecular dynamics gives interesting and useful information about the motion of atomic systems, it is limited by the time scale requirements of modeling atoms. Some materials phenomena are observed to occur over time scales which are outside of this range. Additionally, there are some instances in which it is desirable to know if a particular material behavior is energetically favorable to occur at all. For these cases, methods of energy minimization are used. These types of simulations determine particle configurations with lower potential energy, searching in an unphysical way which cannot necessarily be tied to a time scale. One such method is the conjugate gradient method [10, 11, 12], which determines specific trajectories for the system's particles which are conjugate to all previous trajectories, *i.e.* the set of displacements for all particles at a given step is conjugate to all previous sets of displacements. For a system of particles with the set of positions $\{\boldsymbol{x}^\alpha\}_{(n)}$ at timestep $t = n\Delta t$, the CG algorithm determines the new positions, $\{\boldsymbol{x}^\alpha\}_{(n+1)}$ by using the directions of the forces, $\{\boldsymbol{F}^\alpha\}_{(n)}$ as well as the previous step directions:

$$\{\boldsymbol{x}^\alpha\}_{(n+1)} = \{\boldsymbol{x}^\alpha\}_{(n)} + \alpha_{(n)} \{\boldsymbol{d}^\alpha\}_{(n)} , \tag{2.21}$$

where $\{\boldsymbol{d}^\alpha\}_{(n)}$ is the step direction and

$$\{\boldsymbol{d}^\alpha\}_{(n)} = \{\boldsymbol{F}^\alpha\}_{(n)} + \beta_{(n)} \{\boldsymbol{d}^\alpha\}_{(n-1)} . \tag{2.22}$$

In the expressions above, $\alpha_{(n)}$ is the magnitude of the step taken in the direction $\{\boldsymbol{d}^\alpha\}_{(n)}$ to minimize the potential energy function, while $\beta_{(n)}$ is a quantity derived from the vector dot products of the current and previous residuals, a name used for the negative of gradient of the energy function, the forces $\{\boldsymbol{F}^\alpha\}$. A more comprehensive explanation of the CG algorithm, and its implementation, can be found in the references listed above.

2.1.3 Ensembles and boundary conditions

Although the equations of motion and the numerical techniques used to solve those equations are of the utmost importance in examining the behavior of a system of particles, also of significance are the constraints applied to the system. This involves a discussion of two additional topics, ensemble type and boundary conditions. This section will address these issues as they relate to a MD simulation.

The explanation of atomistic simulation necessitates a discussion about statistical mechanics. Statistical mechanics is the method by which individual properties of particles from a system are used to calculate macroscopically observable and measurable quantities. A well known example is temperature, which is merely a measurement of the average kinetic energy of all particles that make up a system or body. These systems are referred to as ensembles and the observable quantities as ensemble averages. An atomistic simulation is usually constrained such that certain ensemble averages remain constant. For instance, the equations discussed in section 2.1.1 are valid for an ensemble in which the number of particles, N, and total energy, E, are constants. In most MD simulations, a constant volume, V, is specified

either by employing rigid boundaries which provide external forces on some atoms, or by enforcing periodic boundary conditions. Techniques for both will be discussed within this section. Such systems are called NVE ensembles, the three system quantities held constant, or *microcanonical* ensembles.

A common alternative is a system in which temperature, T, is held constant instead of system energy. These are called NVT or *canonical* ensembles and are used in Monte Carlo simulations. Other systems commonly analyzed are the isothermal-isobaric or NPT ensemble, where P denotes pressure or, in general, stress applied to the system, and the *grand canonical* or μVT ensemble. μ denotes the system's chemical potential which is held fixed as particles leave or enter the system. Proper treatment of the NVT and NPT ensembles has been covered by authors such as Andersen [13], Hoover [14]. Nosé [15, 16] and Allen and Tildesley [17]. These treatments involve the addition of several scaling variables as extra degrees of freedom of the system needed to enforce the constant pressure or temperature conditions.

Constant volume simulations are the most common since they do not require extra scaling variables in the MD algorithm. Also, physical experiments performed with "fixed-grip" methods of loading lead to more stable dynamical behavior in materials than do "fixed-load" conditions. Thus, fixed volume simulations accurately model many experimental systems. In general, constant volume implies a constant shape. For simulations in which shape changes occur (*e.g.* martensitic phase transformation), extra scaling variables should be used. In order to maintain constant volume conditions, special care must be taken in modeling the boundaries of the simulation region. Two options available are rigid boundary conditions and periodic boundary conditions.

Rigid boundaries stem from walls beyond which atoms cannot travel. They are usually implemented by restricting a layer or two of atoms bordering the walls to have limited degrees of freedom. A picture of such a system appears in Figure 2.1, where color denotes the type of restriction being applied to a particular atom. This system is a two dimensional model of a constrained thin film with a free surface and a surface trough which is three atomic spaces in width and a single layer in depth. For such a system, colors represent a numerical value of a separate variable which would be evaluated in routines to calculate new positions. Rigid boundary conditions are sometimes used to model an atomistic region embedded in a continuum where the rigidly constrained atoms constitute only a small percentage of the total number of atoms in the system. One advantage of using rigid boundary conditions is the ability to model single defect systems which cannot be done using periodic boundary conditions. However, energies and forces of atoms that make up the rigid boundary are not equivalent to bulk atom energies and forces. Thus, calculations of energy and stress for such a system might be misinterpreted.

More commonly used in simulations are periodic boundary conditions. In such systems, the lengths of the system in the constrained directions are constant. If an atom is moved beyond the system's boundaries, then its position is recalculated with the appropriate length subtracted, effectively moving the atom to other side of the simulation region. In this way, it can be considered that the atom has left the simulation region while its periodic image

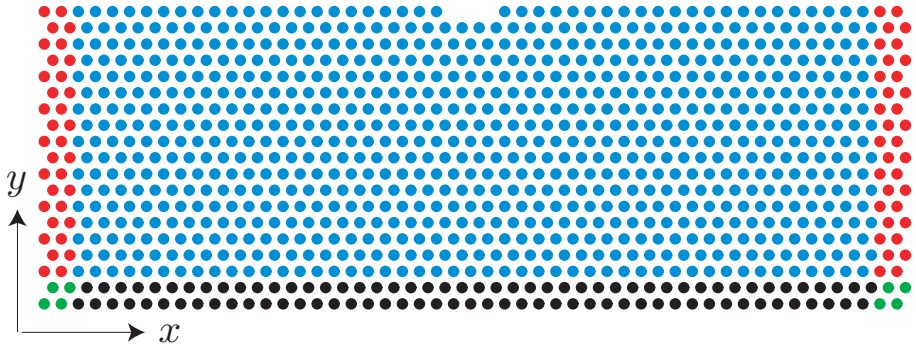

Figure 2.1: A two dimensional triangular lattice atomistic system where different colors denote different boundary conditions - Red: motion in x-direction is constrained, black: motion in y-direction is constrained, green: motions in x- and y-directions are constrained, blue: atom is free in both directions

has entered it. This is shown pictorially in Figure 2.2. Atoms near the periodic boundaries in these systems have the same energies and forces as bulk atoms because they effectively "feel" the periodic images of other atoms as their nearest neighbors. Thus, periodic boundary conditions allow a small simulation region with a limited number of particles to successfully model bulk material, enabling calculation of bulk properties.

It is useful to mention here the concept of "neighbor lists" which is customarily used for particle simulations which involve short-range interactions among particles. For a system of N atoms, each atom will generally interact with every other atom, resulting in a total of approximately $\frac{N^2}{2}$ interactions. Realistically, however, empirical potentials are defined such that there is a limited range of interaction. For example, many interatomic potentials use a radial cutoff parameter, r_{cut}. Any atoms that are separated by a greater distance than r_{cut} have zero interaction and do not need to be considered in energy and force calculations. If the simulation region is spatially divided into sub-regions which are just over r_{cut} in width, then for a given particle only its sub-region and adjacent sub-regions are searched for possible neighbors. This results in a total of $9N_cN$ interactions for 2-dimensional systems and $27N_cN$ interactions for 3-dimensional systems, where N_c is the characteristic number of particles in a sub-region, which remains constant with increasing system size as long as the sub-region width remains constant. In MD simulation, a list of neighbors is created according to this search strategy. The list does not have to be updated every time step, but only every 10 to 20 time steps depending on the motion of the atoms in the system.

2.1.4 Interatomic potentials

The motion of each particle is obtained from Newton's 2^{nd} law (2.1) and the total potential energy of the system $\mathcal{U}$, (2.6), which is assumed to depend only upon atomic positions $\{\mathbf{x}^\alpha\}$. It is the task of the analyst to create a functional form of $\mathcal{U}$ and adjust parameters used

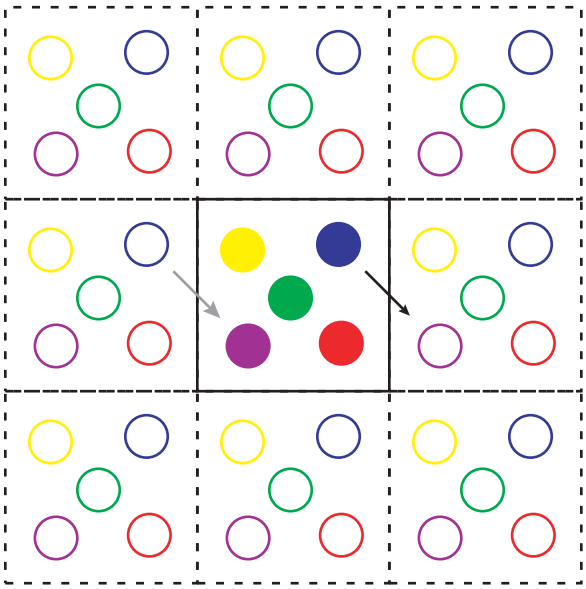

Figure 2.2: A two dimensional system with periodic boundary conditions. The black arrow shows the blue particle moving out of the real simulation system, denoted by the solid square, while the gray arrow shows its periodic image moving into the system.

in the function to reproduce either experimentally measured material constants or *ab initio* calculations. This section will review the development of two interatomic potentials, the functional forms of $\mathcal{U}$, namely the Lennard-Jones pair potential and the embedded atom method, both of which were used in this work.

The Lennard-Jones pair potential

Early efforts at developing interatomic potentials involved simple pair potentials where the total potential energy is a summation of pairwise interactions,

$$\mathcal{U} = \frac{1}{2}\sum_{\alpha=1}^{N}\sum_{\beta\neq\alpha}^{N} U\left(r^{\alpha\beta}\right). \tag{2.23}$$

Here, $r^{\alpha\beta} = \left|\vec{x}^{\alpha} - \vec{x}^{\beta}\right|$. The factor of $\frac{1}{2}$ compensates for double-counting the interaction between every pair of atoms. One of the most successful models is the one by Lennard-Jones [18, 19],

$$U\left(r\right) = k\varepsilon\left[\left(\frac{\sigma}{r}\right)^{n} - \left(\frac{\sigma}{r}\right)^{m}\right], \tag{2.24}$$

where n and m are integers with $n > m$, σ represents a characteristic distance at which the interaction has zero energy, ε represents the cohesive energy of the atomic bond, and

$$k = \frac{n}{n-m}\left(\frac{n}{m}\right)^{(m/(n-m))}. \tag{2.25}$$

This model is called a "soft-sphere" potential because it can model both the repulsive force of atoms too near to each other as well as the attractive force the atoms feel if they are stretched too far apart. The Lennard-Jones model is most often used with the values $n = 12$ and $m = 6$, resulting in $k = 4$ and

$$U(r) = 4\varepsilon\left[\left(\frac{\sigma}{r}\right)^{12} - \left(\frac{\sigma}{r}\right)^{6}\right]. \tag{2.26}$$

The equilibrium distance for this potential can be determined to be $r_{eq} = 2^{\frac{1}{6}}\,\sigma \approx 1.1225\,\sigma$. The Lennard-Jones model has been shown to be very effective in modeling inert-gas solids, although it is commonly used to model generic behavior in all types of solid materials.

Two common criticisms of the pair potential arise because it is often used inappropriately. The first criticism is that the potential is only a function of bond distance ($r^{\alpha\beta}$) and not of bond orientation. Thus, it is inappropriate to use pair potentials to model covalent solids such as carbon and silicon. Other types of empirical potentials have been developed for modeling covalent crystals, such as the Stillinger-Weber model [20] in which the total energy is the sum of pair interactions *and* triplet interactions. It is these triplet interactions which associate an energy with the orientation of the atomic bonds. The second criticism is that pair potentials lead to Cauchy symmetry of the elastic constants, a symmetry not generally found in solids such as FCC metals. The Cauchy symmetry condition is the property that

$$C_{IJKL} = C_{IKJL}, \tag{2.27}$$

where C_{IJKL} are the initial tangent moduli, the elastic stiffness constants for an equilibrium lattice. Note that this symmetry condition is neither the major ($C_{IJKL} = C_{KLIJ}$) nor the minor ($C_{IJKL} = C_{JIKL} = C_{IJLK} = C_{JILK}$) symmetries known to be true for cubic crystals. In cubic crystals, Cauchy symmetry amounts to the condition

$$C_{12} = C_{44}, \tag{2.28}$$

which restricts the anisotropy of the material being modeled. Although such a material has only two independent elastic constants, the material is *not* isotropic. Isotropic materials are those for which elastic properties are independent of direction. Such materials have an anisotropy ratio,

$$A = \frac{2C_{44}}{C_{11} - C_{12}}, \tag{2.29}$$

equal to unity, and have only two independent elastic constants. For a material with Cauchy symmetry, the anisotropy ratio is fixed once the underlying structure of the material is specified. For example, in an amorphous material, $C_{12} = \frac{1}{3}\,C_{11}$, so $A = 1$, while for a FCC lattice in which only nearest neighbors interact $C_{12} = \frac{1}{2}\,C_{11}$ and $A = 2$.

The Embedded Atom Method

In the 1980's, Daw, Baskes and Foiles [21, 22, 23, 24] created a new empirical potential specifically designed to model metals with accurate elastic properties. This potential was based on a technique named the embedded atom method (EAM). EAM describes the total potential energy of a system of atoms as

$$\mathcal{U} = \sum_{\alpha=1}^{N} F_\alpha(\rho_\alpha) + \frac{1}{2}\sum_{\alpha=1}^{N}\sum_{\beta\neq\alpha}^{N} U_{\alpha\beta}(r^{\alpha\beta}). \tag{2.30}$$

F_α is the energy necessary to "embed" atom α in an electron gas of some density ρ_α composed of contributions from all the neighbors β of the atom. The electron density is assumed to be a linear superposition of spherically-averaged atomic charge densities,

$$\rho_\alpha = \sum_{\beta\neq\alpha}^{N} f_\beta\left(r^{\alpha\beta}\right). \tag{2.31}$$

It is this assumption that is both the strength and the weakness of the embedded atom method. By assuming the electron density has this form, the number of calculations to be performed is comparable to, although still greater than, that for a pair potential simulation. However, this form limits the applicability of EAM. Only simple metals and early or late transition metals can be modeled correctly with EAM. Covalent solids and metals in which bond hybridization is an important effect cannot be properly modeled by EAM.

The second term in equation (2.30) is a standard pair potential. For the Daw, Baskes and Foiles model, this pair potential represents the Coulombic repulsion between atomic cores (nuclei and inner electron shells). Both the pair potential and the atomic charge density function are predefined functions; they are in the references mentioned above. The embedding function is derived by equating a system's total energy with some equation-of-state, such as that by Rose *et al.* [25], and deducing the form of $F(\rho)$ by considering the case of hydrostatic deformation of a single-crystal material.

By using both embedding energy and pair potential terms, the EAM avoids producing elastic stiffnesses with Cauchy symmetry. Expressions for stiffness are shown [22] to have terms proportional to the slope and curvature of the embedding function $F(\rho)$. Without the embedding function, or if the embedding function is a linear function of electron density, effectively making another pair potential, then the Cauchy symmetry is recovered. The pair potential function is also vital; without it the unphysical relations $C_{11} = C_{12}$ and $C_{44} = 0$ result.

Potentials for ionic crystals

Some of our simulations will be nanoindentation of MgO. MgO is an ionic crystal, for which the primary mode of bonding is the Coulomb interaction of + and − charged ions. Interatomic potential models for ionic crystals use the Coulomb potential as the dominant

term,

$$\mathcal{U}_C = \frac{1}{2}\sum_{\alpha=1}^{N}\sum_{\beta\neq\alpha}^{N}\frac{q_\alpha q_\beta e^2}{r^{\alpha\beta}}, \tag{2.32}$$

where q_α is the net charge of ion α in units of e, the magnitude of charge for an electron. The Coulomb potential is known to be a "long-range" potential for two reasons. First, the r^{-1} singularity dies off very slowly, so the energy for an interaction is still significant even at large distances. Second, since these energy terms have alternating signs, ions of like sign provide a positive energy while ions of differing sign provide a negative energy, their accumulation into a total energy per atom for a crystal lattice is a slowly-converging summation. In order to use the Coulomb potential over a limited range, mathematical "tricks" have to be introduced. One such method is the one by Ewald [17] which imposes structural periodicity on the physical system and breaks the total energy into the sum of two rapidly converging contributions, one for real space and one for reciprocal-space. This method requires a large computational effort to evaluate the reciprocal-space summation, although still less than doing $\mathcal{O}\left(N^2\right)$ calculations. An alternative method has been developed by Wolf *et al.* [26, 27], which uses a spherically truncated potential and image charges in order to convert the Coulomb potential into a short-range potential. These authors show that by truncating the Coulomb potential at a cut-off radius R_c and by placing image charges for each ion at R_c, the slowly converging summation rapidly converges and the interaction energy smoothly approaches zero at R_c. Also, a damping factor is used to compensate for the r^{-1} singularity and a self-energy term is added to obtain the full energy of the lattice. The resulting expression for potential energy is:

$$\mathcal{U}_W = \frac{1}{2}\sum_{\alpha=1}^{N}\sum_{\substack{\beta\neq\alpha \\ \left(r^{\alpha\beta}\leq R_c\right)}}^{N} U_{\alpha\beta}\left(r^{\alpha\beta}\right) - \sum_{\alpha=1}^{N}\mathcal{E}_\alpha, \tag{2.33}$$

where

$$U_{\alpha\beta}\left(r^{\alpha\beta}\right) = \frac{q_\alpha q_\beta e^2\ \mathrm{erfc}\left(\alpha_D\ r^{\alpha\beta}\right)}{r^{\alpha\beta}} - \lim_{r^{\alpha\beta}\to R_c}\left\{\frac{q_\alpha q_\beta e^2\ \mathrm{erfc}\left(\alpha_D\ r^{\alpha\beta}\right)}{r^{\alpha\beta}}\right\} \tag{2.34}$$

and

$$\mathcal{E}_\alpha = \left(\frac{\mathrm{erfc}\left(\alpha_D\ R_c\right)}{2R_c} + \frac{\alpha_D}{\sqrt{\pi}}\right) q_a^2. \tag{2.35}$$

In these expressions, α_D is the damping factor, and values of α_D and R_c are chosen such that $\alpha_D R_c = 3.5$. The use of $\lim\{\}$ is interpreted as not evaluating $r^{\alpha\beta}$ as R_c until any differentiation occurs. Thus,

$$U'_{\alpha\beta}\left(r^{\alpha\beta}\right) = \frac{\partial}{\partial r^{\alpha\beta}}\left(\frac{q_\alpha q_\beta e^2\ \mathrm{erfc}\left(\alpha_D\ r^{\alpha\beta}\right)}{r^{\alpha\beta}}\right) - \lim_{r^{\alpha\beta}\to R_c}\left\{\frac{\partial}{\partial r^{\alpha\beta}}\left(\frac{q_\alpha q_\beta e^2\ \mathrm{erfc}\left(\alpha_D\ r^{\alpha\beta}\right)}{r^{\alpha\beta}}\right)\right\} \tag{2.36}$$

so,

$$U'_{\alpha\beta}\left(r^{\alpha\beta}\right) = -\,q_\alpha q_\beta e^2 \left(\frac{\operatorname{erfc}\left(\alpha_D\, r^{\alpha\beta}\right)}{\left(r^{\alpha\beta}\right)^2} + \frac{2\alpha_D}{\sqrt{\pi}} \frac{\operatorname{erfc}\left(-\alpha_D^2\ \left(r^{\alpha\beta}\right)^2\right)}{r^{\alpha\beta}} - \frac{\operatorname{erfc}\left(\alpha_D\, R_c\right)}{R_c^2} - \frac{2\alpha_D}{\sqrt{\pi}} \frac{\operatorname{erfc}\left(-\alpha_D^2\, R_c^2\right)}{R_c} \right) \tag{2.37}$$

Although equation (2.37) is not identical to the derivative of (2.34) once the limit is taken, the authors of [27] have found that system energy is conserved rather well, nonetheless. The accuracy of using this method was measured by comparing the average energy per ion pair as calculated using (2.33) – (2.35) with the value obtained analytically with the expression derived by Madelung [17] and with a calculation using the Ewald sum [28]. It was determined that this energy differed from both the Madelung energy and the Ewald calculation by only a fraction of a percent, approximately 8.7 $\times$ 10^{-5} % and 8.2 $\times$ 10^{-2} %, respectively. The lattice parameter a_0 at zero temperature and pressure is also very close between the Wolf and Ewald methods, 4.129795 Å and 4.1263 Å, respectively.

It is common that additional pair potential terms are used in addition to the Coulomb potential to model ionic crystals. The potential model chosen for this research is the one by Matsui [29, 30]. The full potential is written as:

$$\mathcal{U} = \mathcal{U}_W + \frac{1}{2}\sum_{\alpha=1}^{N} \sum_{\substack{\beta\neq\alpha \\ \left(r^{\alpha\beta}\leq R_c\right)}}^{N} f_o\left(b_\alpha + b_\beta\right) \exp\left(\frac{a_\alpha + a_\beta - r^{\alpha\beta}}{b_\alpha + b_\beta}\right) - \frac{c_\alpha c_\beta}{\left(r^{\alpha\beta}\right)^6}, \tag{2.38}$$

where $a_{Mg} = 0.894$ Å, $a_O = 1.8215$ Å, $b_{Mg} = 0.04$ Å, $b_O = 0.138$ Å, $c_{Mg} = 29.05$ Å$^3\sqrt{\text{kJ/mol}}$, $c_O = 90.61$ Å$^3\sqrt{\text{kJ/mol}}$ and $f_o = 4.184$ kJ/mol. In addition, the values of q_{Mg} and q_O for use in $\mathcal{U}_W$ are 0.945 and -0.945, respectively. The units of the non-Coulombic terms in 2.38 are kJ/mol and need to be converted to eV/atom. These non-Coulombic terms are added to fit specific properties of the MgO material, such as bulk modulus. They change the total energy/atom by only a small amount, approximately 6 %.

Although this potential was used for nanoindentation simulations, it should be noted that it does not adequately model the elastic and mechanical properties of MgO crystals. While the bulk modulus value, 190.12 GPa, is fairly close to experimental estimates (as reported in [31]), 175.2 GPa, the values for initial elastic moduli differ. This potential produces $C_{11} = 397.65$ GPa and $C_{12} = 86.35$ GPa. Since the Matsui potential is just a summation of pair potential terms, including the Coulomb potential, it too produces Cauchy symmetry, hence $C_{44} = C_{12} = 86.35$ GPa. The values referenced in [31] are $C_{11} = 329.8$ GPa, $C_{12} = 97.9$ GPa and $C_{44} = 164.7$ GPa. These are differences of 21 %, -12 % and -48 %. Clearly, the state of the art in ionic crystal atomistic simulation needs to be improved by the inclusion of many-body effects in the interatomic potentials.

2.1.5 Atomistic metrics

A tensor variable used in the analysis of atomistic simulations is the *atomic stress*. The theorems developed by Clausius [32] and Maxwell [33] relate the Cauchy stress tensor $\boldsymbol{\sigma}$ applied to the boundary of a volume V containing N atoms to the kinetic motion and interatomic forces between those atoms,

$$\boldsymbol{\sigma} = -\frac{1}{V}\overline{\left\{\frac{1}{2}\sum_{\alpha=1}^{N}\sum_{\beta\neq\alpha}^{N}\mathbf{x}^{\alpha\beta}\otimes\mathbf{F}^{\alpha\beta}+\sum_{\alpha=1}^{N}m_{\alpha}\dot{\mathbf{x}}^{\alpha}\otimes\dot{\mathbf{x}}^{\alpha}\right\}}. \tag{2.39}$$

In this expression, $\mathbf{x}^{\alpha}$ denotes atom α's current position, $\mathbf{x}^{\alpha\beta}\equiv\mathbf{x}^{\alpha}-\mathbf{x}^{\beta}$, $\mathbf{F}^{\alpha\beta}$ is the force atom β exerts on atom $\alpha/\alpha,\beta=1,2,...,N/$, and $\otimes$ is the dyad product. The overline denotes the taking of a long time average. This expression is commonly used to define a local, instantaneous atomic stress,

$$\boldsymbol{\pi}^{\alpha} = -\frac{1}{V_{\alpha}}\left\{\frac{1}{2}\sum_{\beta\neq\alpha}^{N}\mathbf{x}^{\alpha\beta}\otimes\mathbf{F}^{\alpha\beta}+m_{\alpha}\dot{\mathbf{x}}^{\alpha}\otimes\dot{\mathbf{x}}^{\alpha}\right\}, \tag{2.40}$$

where $\boldsymbol{\sigma}$ is the time and ensemble average of $\boldsymbol{\pi}^{\alpha}$. In this expression, V_{α} is the volume associated with atom α. This atomic stress is the most meaningful measure of continuum mechanical stress in atomistic simulations, although it does display some anomalous behavior at free surfaces [34].

A useful metric for the visualization of atomistic systems is the centrosymmetry parameter, P^{α}, developed by Kelchner *et al.* [35]. The expression for P^{α} is

$$P^{\alpha} = \frac{1}{a_0^2}\sum_{\beta\neq\alpha}^{n/2}\left(\mathbf{x}^{\alpha\beta}+\mathbf{x}^{\alpha\beta^{*}}\right)^2, \tag{2.41}$$

where a_0 is the lattice parameter for the simulated crystal, n is the number of nearest neighbors to atom α and β^{*} represents the neighbor of atom α which is radially opposite the neighbor β. This summation equals zero for a radially symmetric crystal, such as FCC or BCC, which has undergone a homogeneous deformation. However for atoms which no longer possess radial symmetry of near neighbors, such as those on surfaces, dislocation cores and stacking faults, P^{α} will be a significant value greater than zero. Such a quantity is necessary in order to create images which distinguish defects from bulk material.

To provide information on the Burgers vectors of dislocations, we developed the *slip vector*, defined as

$$\boldsymbol{s}^{\alpha} = -\frac{1}{n_s}\sum_{\beta\neq\alpha}^{n}\left(\mathbf{x}^{\alpha\beta}-\mathbf{X}^{\alpha\beta}\right). \tag{2.42}$$

In this expression, n_s is the number of slipped neighbors, and $\mathbf{X}^{\alpha\beta}$ is the vector differences of atoms α and β reference positions, respectively. The reference configuration is the arrangement of atomic positions associated with zero mechanical stress. Although the term "slip

vector" has been used as a synonym for the Burgers vector [36], in the present context its meaning is given by (2.42). This expression will result in the Burgers vector for the slip of adjacent atomic planes where the atom lies on one of those planes. The slip vector will have a large magnitude for any inhomogeneous deformation near an atom and provides quantitative information about the deformation. The slip vector can be used for any material microstructure, making it more generally applicable than the centrosymmetry parameter. Together, the slip vector and the atomic stress expression can provide an estimate of the resolved shear stress acting in the direction of slip.

2.2 Continuum Simulation

In this section, we introduce selected concepts from the mechanics of a continuum subject to finite deformations. The opening section introduces measures of deformation. Green elastic theory then provides the framework in which the stress response and material tangent moduli are derived from changes in the elastic stored energy as a function of the deformation. All the constitutive models presented in later chapters rely on the Green elastic constitutive assumption. We then develop a class of constitutive models using the Cauchy-Born rule. The motivation for this approach is to develop constitutive models for single crystal materials which display realistic elastic properties at finite strains. The approach is inherently multiscale, the link between microstructural and continuum length scales being made using an equivalence of energy. The continuum notion of strain energy density is equated to the energy stored in the bonds of a representative volume of the material at the microstructural level. A brief history of the method and its applications will be presented. Several examples follow to demonstrate the application of the method to different types of semi-empirical potentials originally developed for static and dynamic molecular simulations. An alternative approach for continuum-scale simulation is that of cohesive surfaces. This method allows a traction-separation relation reflecting a finite work to decohesion to be used to model the propagation of cracks. The description of the cohesive surface formulation is also presented in this section.

2.2.1 Kinematics of deformation

In the hyperelastic theory of continuum mechanics[37, 38], material points in the undeformed configuration are described by their reference (Lagrangian) coordinates $\mathbf{X} = (X_1, X_2, X_3)$, while points in the deformed body are described by spatial (Eulerian) coordinates $\mathbf{x} = (x_1, x_2, x_3)$. Throughout this discussion, we will make use of the convention that upper case variables refer to quantities in their material representation, while lowercase variables refer to the corresponding spatial representations. The motion of a point X_I in the Lagrangian coordinates to a point $\mathbf{x}_i$ in Eulerian coordinates is described by the motion

$$\mathbf{x}(\mathbf{X}, t) = \boldsymbol{\varphi}(\mathbf{X}, t)\,. \tag{2.43}$$

Using the motion (2.43), we can describe the deformation of a small fiber $d\mathbf{X}$ emanating from the material point $\mathbf{X}$. The deformed vector $d\mathbf{x}$ can be approximated with a Taylor expansion

$$\begin{aligned} d\mathbf{x} &= \boldsymbol{\varphi}(\mathbf{X} + d\mathbf{X}, t) - \boldsymbol{\varphi}(\mathbf{X}, t) \\ &= \left[\boldsymbol{\varphi}(\mathbf{X}, t) + \frac{\partial \boldsymbol{\varphi}(\mathbf{X}, t)}{\partial \mathbf{X}} \, d\mathbf{X} + \frac{1}{2} \, d\mathbf{X} \cdot \frac{\partial^2 \boldsymbol{\varphi}(\mathbf{X}, t)}{\partial \mathbf{X}^2} \, d\mathbf{X} + \dots \right] - \boldsymbol{\varphi}(\mathbf{X}, t) \, . \end{aligned} \tag{2.44}$$

Neglecting higher order terms in (2.44), the vector $d\mathbf{X}$ is mapped to its deformed configuration by

$$d\mathbf{x}(\mathbf{X}, t) = \mathbf{F}(\mathbf{X}, t) \, d\mathbf{X}, \tag{2.45}$$

where we have defined the deformation gradient $\mathbf{F}$ as

$$F_{iI}(\mathbf{X}, t) = \frac{\partial \varphi_i(\mathbf{X}, t)}{\partial X_I}. \tag{2.46}$$

The length of the deformed vector $d\mathbf{x}$ is

$$dx = \sqrt{d\mathbf{X} \cdot \mathbf{F}^{\mathrm{T}} \mathbf{F} \, d\mathbf{X}}, \tag{2.47}$$

which gives rise to the definition of the right Cauchy-Green stretch tensor

$$\mathbf{C} = \mathbf{F}^{\mathrm{T}} \mathbf{F}. \tag{2.48}$$

By expressing $d\mathbf{X}$ in terms of its length dX and direction $\boldsymbol{\Xi}$, the deformed length can be written as

$$dx = dX \, \sqrt{\boldsymbol{\Xi} \cdot \mathbf{C} \, \boldsymbol{\Xi}}, \tag{2.49}$$

where the direction $\boldsymbol{\Xi}$ in two dimensions may be represented in polar coordinates as

$$\boldsymbol{\Xi}(\phi) = \begin{Bmatrix} \cos \phi \\ \sin \phi \end{Bmatrix} \qquad (-\pi \leq \phi \leq \pi) \, , \tag{2.50}$$

and in three dimensions using spherical coordinates as

$$\boldsymbol{\Xi}(\theta, \phi) = \begin{Bmatrix} \sin \theta \, \cos \phi \\ \sin \theta \, \sin \phi \\ \cos \theta \end{Bmatrix} \qquad (0 \leq \theta \leq \pi, -\pi \leq \phi \leq \pi) \, . \tag{2.51}$$

From a spatial description, we can map an infinitesimal vector back to its corresponding undeformed description by inverting (2.45) to give

$$d\mathbf{X}(\mathbf{x}, t) = \mathbf{F}^{-1}(\mathbf{x}, t) \, d\mathbf{x}. \tag{2.52}$$

The expression for the original length of $d\mathbf{x}$,

$$dX = \sqrt{d\mathbf{x} \cdot \mathbf{F}^{-\mathrm{T}}\mathbf{F}^{-1}\, d\mathbf{x}}, \tag{2.53}$$

gives rise to the definition of the left Cauchy-Green stretch tensor

$$\mathbf{b} = \mathbf{F}\,\mathbf{F}^{\mathrm{T}}. \tag{2.54}$$

Making use of the polar decomposition of $\mathbf{F}$,

$$\mathbf{F} = \mathbf{R}\,\mathbf{U} = \mathbf{V}\,\mathbf{R}, \tag{2.55}$$

where $\mathbf{R}$ is a proper orthogonal transformation, and $\mathbf{U}$ and $\mathbf{V}$ are symmetric and positive definite, we can derive

$$\mathbf{U} = \mathbf{C}^{1/2}, \qquad \mathbf{V} = \mathbf{b}^{1/2}, \quad \text{and} \qquad \mathbf{U} = \mathbf{R}^{\mathrm{T}}\,\mathbf{V}\,\mathbf{R}. \tag{2.56}$$

From the relations (2.56), we can see that the stretch tensors $\mathbf{C}$ and $\mathbf{b}$ have the same eigenvalues and that their principal directions are related by the rotation $\mathbf{R}$.

2.2.2 Green elastic theory

The basic postulate of Green elastic materials is the existence of a strain energy density $\mathcal{W}(\mathbf{F})$ which defines the stress and modulus at a point $\mathbf{X}$ as a function of the local state of deformation. In order to satisfy the requirement for material frame indifference, we limit our discussion to strain energy densities which are expressed as a function of the right stretch $\mathbf{C}$, that is

$$\mathcal{W}(\mathbf{F}) = \Phi(\mathbf{C})\,. \tag{2.57}$$

To illustrate the reason for this choice, we imagine modifying a motion given by $\boldsymbol{\varphi}(\mathbf{X}, t)$ with an additional rigid body motion such that the final motion is given by

$$\boldsymbol{\varphi}^{+}(\mathbf{X}, t) = \mathbf{g}(t) + \mathbf{r}(t)\ \boldsymbol{\varphi}(\mathbf{X}, t)\,. \tag{2.58}$$

where $\mathbf{g}(t)$ represents a rigid body translation, and $\mathbf{r}(t)$ is a rigid body rotation satisfying $\mathbf{r}^{-1} = \mathbf{r}^{\mathrm{T}}$ and $\det[\mathbf{r}(t)] = 1$. We may also interpret this situation as corresponding to observations of the same deformation from two different material reference frames. The observation of $\boldsymbol{\varphi}^{+}$ can be thought of as occurring in a reference frame which is translating and rotating with respect to the frame in which we observe $\boldsymbol{\varphi}$. In this second reference frame, the deformation gradient is

$$\mathbf{F}^{+} = \mathbf{r}(t)\,\mathbf{F}, \tag{2.59}$$

from which we can see that the right stretch is invariant with respect to the rigid body rotation $\mathbf{r}$ since

$$\mathbf{C}^{+} = \left(\mathbf{F}^{+}\right)^{\mathrm{T}}\mathbf{F}^{+} = \mathbf{F}^{\mathrm{T}}\,\mathbf{r}^{\mathrm{T}}\mathbf{r}\,\mathbf{F} = \mathbf{C}. \tag{2.60}$$

As we would expect, the deformation is therefore observed to be the same by observers in either frame.

From the theory of Green elastic materials, the strain energy function $\Phi(\mathbf{C})$ defines the symmetric (2^{nd}) Piola-Kirchhoff stress tensor,

$$S_{IJ} = 2\frac{\partial \Phi}{\partial C_{IJ}}, \tag{2.61}$$

as the work-conjugate of $\mathbf{C}$. The "slope" of the $\mathbf{S}$-$\mathbf{C}$ relationship,

$$\mathsf{C}_{IJKL} = 2\frac{\partial S_{IJ}}{\partial C_{KL}} = 4\frac{\partial^2 \Phi}{\partial C_{IJ}\partial C_{KL}}, \tag{2.62}$$

is the material tangent modulus. Due to the distinction between the reference and current configurations, stress and tangent modulus are not uniquely defined. The asymmetric (1^{st}) Piola-Kirchhoff stress tensor is defined by

$$P_{iJ} = \frac{\partial \mathcal{W}}{\partial F_{iJ}}. \tag{2.63}$$

$\mathbf{P}$ is related to $\mathbf{S}$ by

$$P_{iJ} = F_{iI} S_{IJ}. \tag{2.64}$$

The pair $\{\mathbf{P}, \mathbf{F}\}$, like $\{\mathbf{S}, \mathbf{C}\}$, is work-conjugate in the thermodynamic sense. The "slope" of the $\mathbf{P}$-$\mathbf{F}$ diagram,

$$\mathsf{B}_{iJkL} = \frac{\partial P_{iJ}}{\partial F_{kL}} = \delta_{ik} S_{JL} + \mathsf{C}_{IJKL} F_{iI} F_{kK}, \tag{2.65}$$

is the effective tangent modulus. Note that B, unlike C, does not possess minor symmetry with respect to its indices.

The true (Cauchy) stress tensor $\boldsymbol{\sigma}$ is uniquely determined from the traction vector

$$t_i = n_j \, \sigma_{ji}, \tag{2.66}$$

that represents the force per unit deformed area exerted on a surface element with outward normal $\mathbf{n}$. The stress tensors $\boldsymbol{\sigma}$, $\mathbf{S}$, and $\mathbf{P}$ are related by

$$J\sigma_{ij} = P_{iJ} F_{jJ} = F_{iI} S_{IJ} F_{jJ}, \tag{2.67}$$

where

$$J = \det \mathbf{F} \tag{2.68}$$

is the Jacobian determinant of deformation. Admissible states of deformation are those for which $J > 0$, meaning we do not admit deformations which "fold" the continuum over, or through, itself. The corresponding "stiffness"

$$\mathsf{c}_{ijkl} = \frac{1}{J} \, F_{iI} \, F_{jJ} \, F_{kK} \, F_{lL} \, \mathsf{C}_{IJKL} \tag{2.69}$$

is the spatial tangent modulus.

2.2.3 Cauchy-Born elasticity

Historical overview

The Cauchy-Born rule has a history that dates back to the 1940's. Since that time, the method itself has undergone little change, although the purpose of its use has been transformed with shifting interests and the advent of numerical techniques and capabilities. The method was originally described by Born[39] as a means for estimating the theoretical strength of crystals and for assessing the stability of cubic crystal configurations subject to simple deformations. The deformations considered were limited to those that could be described as single parameter mappings of the atoms from their undeformed positions. Configurations for which the second derivative of the potential energy with respect to the deformation parameter were positive were considered stable. Attempts to make connections between the atomistic and continuum descriptions of materials followed[40, 41, 42]. The focus was on predicting elastic moduli for crystals in the small strain regime, that is, elastic "constants" of the crystals in their undeformed state.

By the time of Hill[43], there emerged an interest in predicting the elastic moduli of crystals subject to larger deformations, as well as stability limits as a function of deformation[44]. Milstein and Hill[45, 46, 47] computed theoretical crystal properties of simple cubic, face-centered cubic, and body-centered cubic crystals under the action of Morse potentials subject to equitriaxial, single parameter deformation states. They predicted bulk and shear moduli and mapped the stability of crystals as a function of the loading parameter. Subsequently, Milstein and coworkers studied more general deformations, deriving expressions for the elastic moduli and assessing stability of face-centered cubic crystals subject to extension along the [110][48] and [111][49] crystal directions. Using the same techniques, they also studied phase transformations between face-centered and body-centered cubic crystal structures under prescribed [100] load paths[50].

More recently[51], the Cauchy-Born rule emerged again, but for the first time, as a means to derive nonlinear, hyperelastic constitutive models for use in numerical simulations to predict stress and deformation under physically realistic loading conditions. Previous application of the theory employed only pairwise potentials with lattices having primitive unit cells, that is, unit cells containing only one atom, and deformation states were limited to those that could be characterized as mappings of at most two parameters. Tadmor and coworkers used the term "quasicontinuum" to describe the constitutive models derived for aluminum using the embedded atom method[22] (EAM) with interatomic potentials derived from first-principles calculations[52]. The complete stress response and tangent moduli were derived for general states of deformation using Green elastic theory with a strain energy density function constructed using the Cauchy-Born rule.

Cauchy-Born rule for crystalline materials

The Cauchy-Born rule is a multiscale assumption about how the motion of many atoms can be related to continuum deformation measures. Under the assumption, the atoms in

a crystal subject to a homogeneous deformation move according to a single mapping from the undeformed to the deformed configuration. From the continuum level, this mapping is taken to be the deformation gradient $\mathbf{F}(\mathbf{X}, t)$ (2.46). As shown in Figure 2.3, the continuum region surrounding a point $\mathbf{X}$ in the undeformed configuration distorts as described by the

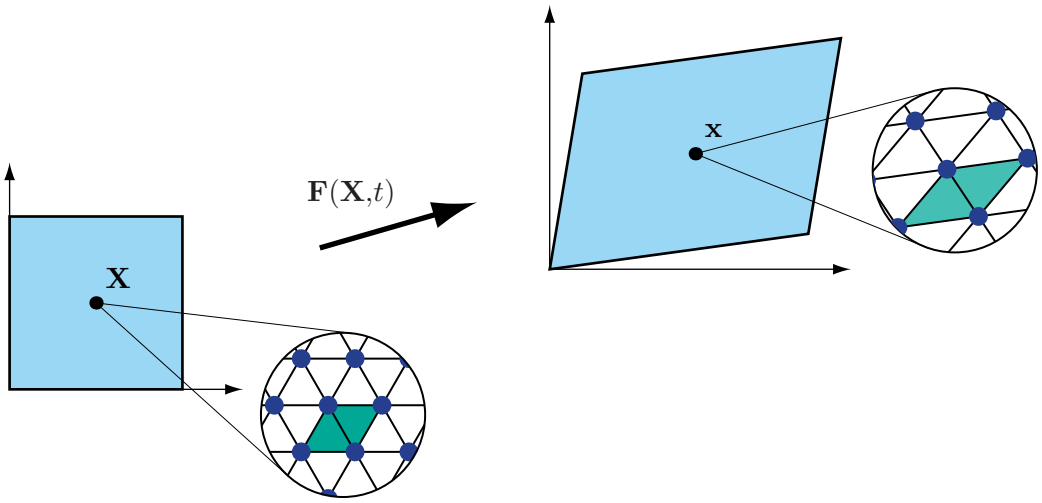

Figure 2.3: Deformation of the underlying microstructure as prescribed by the Cauchy-Born rule.

deformation gradient. The coordinate of the continuum point in the deformed configuration is denoted by $\mathbf{x}$. At a microstructural length scale below the continuum level, we assume the deformation of an underlying crystal lattice undergoes the same homogeneous transformation. The deformation gradient at a point at the continuum length scale is assumed to be constant over a boundless crystal at the microstructural length scale. The microstructural description of a crystalline material and the corresponding continuum constitutive properties are linked using an equivalence in strain energy density. The continuum-level strain energy density is equated to the energy in a representative volume of the microstructure. Since the deformation is homogeneous, the behavior of an arbitrarily large crystal can be studied by considering only the representative volume subject to periodic boundary conditions. For crystalline materials of a single species with a primitive unit cell, this representative volume is the atomic volume. The change in energy per unit volume for a given deformation predicted by this procedure corresponds to the bulk behavior of the crystal at zero Kelvin. There are no surface or temperature-dependent effects. The atoms in the crystal interact as determined by assumed bonding potential functions. Taken from atomistic calculations, these semi-empirical relationships may be in the form of pairwise potentials, or multi-body potentials such as the embedded atom method. The number of bonds contributing to the energy in the representative volume depends on the range of influence of the bonding potentials.

As a first illustration, we consider a crystal whose atoms interact only through pair

potentials. For this case, the strain energy density is

$$\Phi_2(\mathbf{C}) = \frac{1}{\Omega_0} \sum_{i=1}^{n_b} U^{(i)}\big(r^{(i)}(\mathbf{C})\big), \tag{2.70}$$

where $\mathbf{C}$ is the right Cauchy-Green stretch tensor (2.48), n_b is the number of bonds, Ω_0 is the representative volume, $r^{(i)}$ is the deformed bond length, and $U^{(i)}(r)$ is a pairwise bond potential. Typically, all the bonds are assumed to be governed by the same potential function $U(r)$. Since the deformation is assumed homogeneous over the crystal, the transformation defined by $\mathbf{F}$ can be applied to vectors of finite length. For each bond in the undeformed unit cell, we define a bond vector

$$\mathbf{R} = R\,\boldsymbol{\Xi}, \tag{2.71}$$

where R and $\boldsymbol{\Xi}$ are the undeformed bond length and direction, respectively. Using (2.49) from the kinematics of large deformations, we can express the deformed bond length as

$$r(\mathbf{C}) = R\,\sqrt{\boldsymbol{\Xi} \cdot \mathbf{C}\,\boldsymbol{\Xi}}. \tag{2.72}$$

Given the strain energy density function (2.70), we can derive a complete description of the stress response and elastic tangent moduli using Green elastic theory. As a function of the stretch tensor $\mathbf{C}$, the 2$^{\text{nd}}$ Piola-Kirchhoff stress can be derived using (2.61) to yield

$$\mathbf{S} = 2\,\frac{\partial \Phi_2}{\partial \mathbf{C}} = \frac{2}{\Omega_0} \sum_{i=1}^{n_b} \left[U'\big(r^{(i)}\big)\,\frac{\partial r^{(i)}}{\partial \mathbf{C}} \right]. \tag{2.73}$$

From (2.62), the material tangent modulus is given by

$$\mathsf{C} = 2\,\frac{\partial \mathbf{S}}{\partial \mathbf{C}} = \frac{4}{\Omega_0} \sum_{i=1}^{n_b} \left[U''\big(r^{(i)}\big)\,\frac{\partial r^{(i)}}{\partial \mathbf{C}} \otimes \frac{\partial r^{(i)}}{\partial \mathbf{C}} + U'\big(r^{(i)}\big)\,\frac{\partial^2 r^{(i)}}{\partial \mathbf{C}\,\partial \mathbf{C}} \right]. \tag{2.74}$$

The derivatives of the deformed bond length (2.72) with respect to $\mathbf{C}$ are given by

$$\frac{\partial r}{\partial \mathbf{C}} = \frac{R^2}{2\,r}\,\boldsymbol{\Xi} \otimes \boldsymbol{\Xi} \qquad \text{and} \qquad \frac{\partial^2 r}{\partial \mathbf{C}\,\partial \mathbf{C}} = -\frac{R^4}{2\,r^3}\,\boldsymbol{\Xi} \otimes \boldsymbol{\Xi} \otimes \boldsymbol{\Xi} \otimes \boldsymbol{\Xi}. \tag{2.75}$$

Substituting (2.75) into (2.73) and (2.74) yields the expressions

$$\mathbf{S} = \frac{1}{\Omega_0} \sum_{i=1}^{n_b} \left[\frac{U'(r)}{r}\,R^2\,\boldsymbol{\Xi} \otimes \boldsymbol{\Xi} \right]^{(i)} \tag{2.76}$$

and

$$\mathsf{C} = \frac{1}{\Omega_0} \sum_{i=1}^{n_b} \left[\left(\frac{U''(r)}{r^2} - \frac{U'(r)}{r^3} \right) R^4\,\boldsymbol{\Xi} \otimes \boldsymbol{\Xi} \otimes \boldsymbol{\Xi} \otimes \boldsymbol{\Xi} \right]^{(i)}, \tag{2.77}$$

which define the material description of the stress response and tangent moduli as a function of $\mathbf{C}$ and the configuration of the undeformed lattice. Using (2.67) and (2.69), we can transform $\mathbf{S}$ (2.76) and C (2.77) to their corresponding spatial representations, giving the Cauchy stress

$$\boldsymbol{\sigma} = \frac{1}{\Omega} \sum_{i=1}^{n_b} \left[r\, U'(r)\, \boldsymbol{\xi} \otimes \boldsymbol{\xi} \right]^{(i)} \tag{2.78}$$

and the spatial tangent modulus

$$\mathbf{c} = \frac{1}{\Omega} \sum_{i=1}^{n_b} \left[\left(r^2\, U''(r) - r\, U'(r) \right) \boldsymbol{\xi} \otimes \boldsymbol{\xi} \otimes \boldsymbol{\xi} \otimes \boldsymbol{\xi} \right]^{(i)}, \tag{2.79}$$

where $\Omega = J\,\Omega_0$ is the deformed volume. The deformed bond vectors are represented as

$$\begin{aligned} \mathbf{r} &= R\,\mathbf{F}\,\boldsymbol{\Xi} \\ &= r\,\boldsymbol{\xi} \qquad \text{where}\, \boldsymbol{\xi} \cdot \boldsymbol{\xi} = 1. \end{aligned} \tag{2.80}$$

The expressions for the material (2.77) and spatial (2.79) tangent moduli possess the standard symmetries of elasticity, as well as Cauchy symmetry, meaning symmetry with respect to any pair of indices. Using the material tangent modulus for illustration, we have the major and minor symmetries

$$\mathsf{C}_{IJKL} = \mathsf{C}_{KLIJ} \qquad \mathsf{C}_{IJKL} = \mathsf{C}_{JIKL} \qquad \mathsf{C}_{IJKL} = \mathsf{C}_{IJLK}, \tag{2.81}$$

as well as the Cauchy relation

$$\mathsf{C}_{IJKL} = \mathsf{C}_{IKJL}. \tag{2.82}$$

Historically, the Cauchy relation has received considerable attention. First noted by Born[39] for undeformed crystals, Stakgold[41] later showed that the Cauchy relation will be satisfied for a crystal which is centrosymmetric and whose atoms interact only with a two body potential. As can be seen in expressions (2.77) and (2.79) for the moduli, the symmetry results from the assumption of pair potential interactions and holds for any state of deformation, regardless of the form of the pair potential. Weiner[53] made use of the Hellmann-Feynman theorem in quantum mechanics to show that the Cauchy relation is satisfied if, in a centrosymmetric crystal, the electron density distribution undergoes the same affine deformation as does the lattice of nuclei. In reality, few if any crystals display Cauchy symmetry, indicating that pair bonding does not accurately describe the atomic interactions in most crystalline materials.

The question of stability for crystals governed by pair potentials has also been the topic of extensive discussions from the early work of Born[39] through the summary work by Milstein[54]. Though stability will not be the subject of a detailed discussion here, we make some general comments to motivate the lattice structures that are introduced later and the

types of bonding that are employed. Briefly, Hill[55] interpreted the loss of strong ellipticity of the strain energy density function as a loss of stability of the solid. At the critical point, one or more of the eigenvalues of the acoustical tensor $\mathbf{q}(\mathbf{N})$ (2.79) vanish, signaling a loss of uniqueness in the admissible modes of deformation. Using the Cauchy-Born stress and modulus, we can assess instantaneous stability of a crystal subject to arbitrary deformations from an analysis of the acoustical tensor.

For simple crystal structures, we can assess stability based on intuitive arguments. A simple cubic (SC) lattice with only nearest neighbor bonds has no stiffness in shear since the lattice can collapse by rotating bonds without stretching them. Including bonds to the second nearest neighbors stabilizes the crystal. Instability of the SC lattice to shear deformations has been used to explain why no monatomic crystals with this structure exist in nature[56]. A body-centered cubic (BCC) lattice can also collapse by simply rotating pair bonds between nearest neighbors. Atomistic simulations of BCC metals typically use embedded atom method potentials, which will be discussed in more detail below. In the examples that follow, we consider only microstructures that are stable in the undeformed configuration.

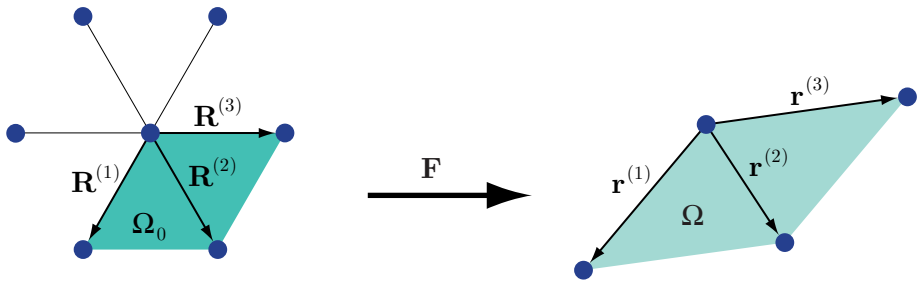

Figure 2.4: Deformation of a unit cell under the Cauchy-Born rule.

Figure 2.4 shows the primitive unit cell of a two-dimensional, triangular lattice with nearest neighbor bonding for which $n_b = 3$. In the undeformed configuration, the bond vectors are given by

$$\mathbf{R}^{(1)} = a_0 \begin{Bmatrix} -1/2 \\ -\sqrt{3}/2 \end{Bmatrix} \quad \mathbf{R}^{(2)} = a_0 \begin{Bmatrix} 1/2 \\ -\sqrt{3}/2 \end{Bmatrix} \quad \mathbf{R}^{(3)} = a_0 \begin{Bmatrix} 1 \\ 0 \end{Bmatrix}, \tag{2.83}$$

where a_0 is the undeformed lattice parameter. Including any more of the six nearest neighbors in the strain energy density (2.70) is redundant since the stretch in any additional bond is already represented by one of the three bonds in (2.83). Figure 2.5 illustrates the change in the neighbor bonding configuration for a range of influence in the interaction potential between a_0 to $2a_0$. From the assumption of homogeneity in the deformation, every bond in the crystal described by a unique pair $(R^{(i)}, \boldsymbol{\Xi}^{(i)})$ is represented by a single interaction in the strain energy density. Since this crystal is centrosymmetric, the bonds appear in pairs as reflections through an atom at the local coordinate origin. Although the range of influence of the bonding potential affects the number of interactions in the energy expression, the

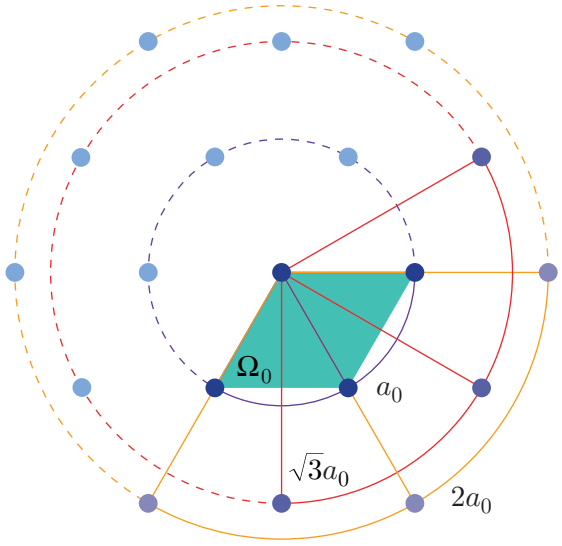

Figure 2.5: The effect of extended bonding potentials.

representative volume $\Omega_0 = \sqrt{3}\, a_0^2/2$ stays fixed, as determined by the crystal structure. This triangular arrangement of atoms also appears in three-dimensional crystals on the [111] plane of the face-centered cubic lattice and on the basal plane of the hexagonal close-packed lattice. These lattice structures, as well as the body-centered cubic or tetragonal structures, can all be described with a primitive unit cell for which the representative volume Ω_0 is the atomic volume. In the analysis of infinitesimal deformations, the plane of close-packed atoms is assumed to be isotropic. From the expressions for the moduli, we see that for arbitrary deformations at finite strain, the crystal will develop generally anisotropic response with six-fold symmetry. In more precise terms, this close-packed lattice arrangement only displays instantaneously isotropic response for deformations that do not disturb the symmetry of the undeformed lattice. For illustration, we present the Cauchy stress and spatial tangent modulus for the two-dimensional, triangular lattice subject to equibiaxial stretching. For this case, the deformation gradient is given by $\mathbf{F} = \lambda \mathbf{1}$, where λ is the stretch. This state of deformation was used by Milstein and Hill[45, 46, 47] in their extensive studies of theoretical crystal properties. Under equibiaxial stretching, the analysis becomes simplified because the sums of the bond orientation terms can be evaluated explicitly for any level of deformation. From (2.78) and (2.79), the Cauchy stress and spatial tangent modulus are given by

$$\boldsymbol{\sigma} = \sigma \mathbf{1}, \tag{2.84}$$

where the magnitude of the equibiaxial stress is

$$\sigma = \frac{3}{2} \frac{a_0}{\lambda \Omega_0} U'(\lambda a_0)\,, \tag{2.85}$$

and

$$\mathbf{c} = \mu \left[\mathbf{1} \otimes \mathbf{1} + 2\,\mathbf{I} \right], \tag{2.86}$$

where the instantaneous shear modulus is

$$\mu = \frac{3}{8\,\Omega_0} \left[a_0^2\, U''(\lambda a_0) - \frac{a_0}{\lambda}\, U'(\lambda a_0) \right]. \tag{2.87}$$

With instantaneous isotropic response under the restriction of Cauchy symmetry, the complete description of the modulus involves only the single parameter μ from (2.87).

The earliest potentials used in lattice modeling were constructed to display the essential features of cohesive interactions between atoms with parameters fitted to available experimental data, such as lattice parameters and elastic properties in the undeformed state. Born[39] employed an "inverse power" potential of the form

$$U(r) = D \frac{nm}{n-m} \left[\frac{1}{n} \left(\frac{r_0}{r} \right)^n - \frac{1}{m} \left(\frac{r_0}{r} \right)^m \right], \tag{2.88}$$

where $n > m$, D, and r_0 were chosen to match experimental data. In particular, the well-known Lennard-Jones potential results from (2.88) with $m = 6$ and $n = 12$. Because of its simplicity, the Lennard-Jones potential is still widely used in simulations, though the continuum properties it produces are best-suited to frozen rare gases. In the extensive studies of Milstein and coworkers cited earlier, the so-called Morse function

$$U(r) = \frac{D}{m-1} \left[e^{-m\alpha(r-r_0)} - m e^{-\alpha(r-r_0)} \right] \tag{2.89}$$

was chosen to model the interatomic bonding. These functional forms were motivated by simple physical considerations. Quoting directly from conditions outlined in an early work by Girifalco[57]:

(1) The force $-\partial U/\partial r$ must be attractive at large r and repulsive at small r; therefore, $U(r)$ must have a minimum at some point $r = r_0$;

(2) The magnitude of U must decrease more rapidly with r than r^{-3};

(3) All elastic constants are positive.

The first condition arises from the existence of condensed phases while the second ensures that the work to complete dissociation of an interaction is finite. From this general description, we can construct any number of acceptable potentials with characteristics described by Figure 2.6. For both (2.88) and (2.89), the "force" between atoms vanishes when $r = r_0$, and the work to complete separation, or the depth of the potential well, is given by $-U(r_0) = U_0$. The continuum notions of cohesive stress and fracture energy cannot be determined from the bond potential function alone. As we will show later, both of these quantities depend not

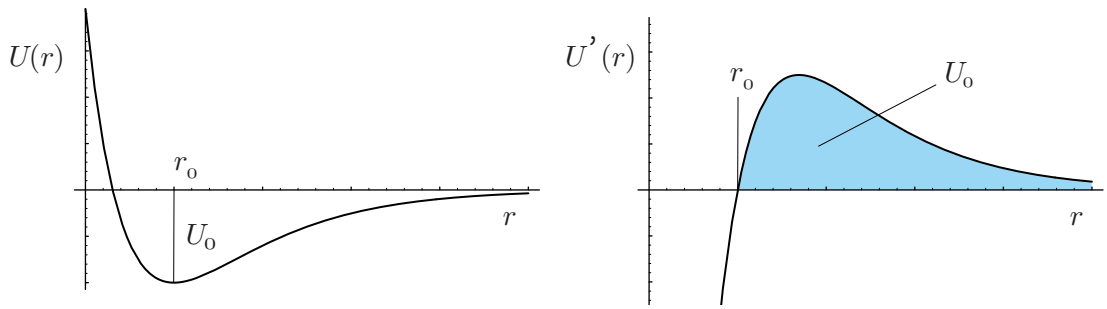

Figure 2.6: The bond energy and force-separation characteristics of a cohesive interaction potential.

only on the assumed bonding arrangement, but also on the assumed state of deformation. The third condition of Girifalco indicates that the earlier investigators did not consider the Cauchy-Born rule as a method for studying fracture though the form of the potentials clearly results in unstable lattice configurations at sufficiently large deformations.

The embedded atom method[22] (EAM) was developed in an attempt to incorporate more physical understanding into the bond potential functions. Originally motivated by the view of metals as nuclei in a sea of electrons, the total energy of any atom in the crystal is comprised of a contribution due to the nuclear repulsion and an embedding energy representing the attraction of the nucleus to the background electron density. In fitting a set of EAM potentials to a particular material, one must define three functions: a pair potential describing nuclear interactions, the electron density distribution around each nucleus, and a function describing the interaction between a nucleus and the background electron density. Although quite different from simple pair interactions, EAM potentials may be incorporated into the procedures for deriving constitutive properties without any modifications to the assumptions of the Cauchy-Born rule.

Using EAM potentials, the strain energy density has two contributions,

$$\Phi_{\text{EAM}} = \Phi_2 + \Phi_e, \tag{2.90}$$

where Φ_2 is the contribution from the nuclear interactions given by the pair potential expression (2.70) and Φ_e is the embedding energy. This additive split in the total energy results in additive contributions to the stress response and tangent moduli. Therefore, all expressions derived from (2.70) still apply, and we only need to discuss the additional contribution due to the embedding energy. The contribution to the total energy (2.90) due to the embedding energy may be written as

$$\Phi_e = \frac{1}{\Omega_0} F(\rho) \tag{2.91}$$

where ρ is the background electron density, that is, the electron density at the nucleus of a particular atom resulting from all neighbors of the atom, but not the atom itself. As a first

approximation, the electron density is assumed to be centrosymmetric

$$\rho = \sum_{i=1}^{n_b} f\left(r^{(i)}\right). \tag{2.92}$$

From even cursory knowledge of electrodynamics, we understand that representing the electron density as a spherically averaged distribution is a gross oversimplification; however, determining the distribution more accurately using quantum mechanical calculations is far too costly to be considered for large scale simulations. In more recent work by Baskes and coworkers[58, 59], some angular dependence is introduced into the electron density distributions in an attempt to generate better agreement with experimental values for the elastic moduli of certain metals.

Considering only centrosymmetric electron density distributions (2.92), the additional contribution to the 2$^{\text{nd}}$ Piola-Kirchhoff stress due the embedding energy is given by

$$\mathbf{S}_e = \frac{1}{\Omega_0} F'(\rho)\, \hat{\mathbf{S}}_e, \tag{2.93}$$

where

$$\hat{\mathbf{S}}_e = \sum_{i=1}^{n_b} \left[\frac{f'(r)}{r} R^2\, \boldsymbol{\Xi} \otimes \boldsymbol{\Xi} \right]^{(i)}. \tag{2.94}$$

The additional contribution to the material tangent modulus is

$$\mathbf{C}_e = \frac{1}{\Omega_0} \left[F'(\rho)\, \hat{\mathbf{C}}_e + F''(\rho)\, \hat{\mathbf{S}}_e \otimes \hat{\mathbf{S}}_e \right], \tag{2.95}$$

where

$$\hat{\mathbf{C}}_e = \sum_{i=1}^{n_b} \left[\left(\frac{f''(r)}{r^2} - \frac{f'(r)}{r^3} \right) R^4\, \boldsymbol{\Xi} \otimes \boldsymbol{\Xi} \otimes \boldsymbol{\Xi} \otimes \boldsymbol{\Xi} \right]^{(i)}. \tag{2.96}$$

It should be noted that this additional contribution to the tangent modulus does not possess Cauchy symmetry, as is evident from the term involving $\hat{\mathbf{S}}_e \otimes \hat{\mathbf{S}}_e$ in (2.95). The contribution to the energy from the embedding term represents a multibody interaction, rather than a simple pair interaction. However, Cauchy symmetry would be preserved if the embedding energy function F were selected to be at most linear in the background electron density.

Combining the classical Cauchy-Born rule with atomistic potentials results in the modern application of the Cauchy-Born rule as a means for linking microstructure to nonlinear continuum constitutive models. The procedure outlined above may be applied to any of the available EAM potentials. Many methods exist for deriving EAM potentials. Some potentials are developed by assuming functional forms in which adjustable parameters are selected to match experimental measurements[22, 60]. Other potentials are developed by calculating

fitted functions based on *ab initio* simulations[52]. Though the first principle calculations are "exact", the accuracy of the resulting Cauchy-Born constitutive models is still limited by the centrosymmetric assumption used to represent the nuclear interactions and the electron density distribution. The range of deformation for which the Cauchy-Born models are applicable is limited in metals by the onset of plastic flow, even for single crystal specimens. In the presence of dislocations, the deformation of the crystal is no longer homogeneous and therefore cannot be represented by a single mapping given by the deformation gradient $\mathbf{F}$. Tadmor and coworkers[51] developed the "nonlocal quasicontinuum" formulation to bridge the transition between homogeneous crystal deformation and the formation of individual dislocations. The accuracy of Cauchy-Born constitutive models in response to homogeneous deformations is determined by the accuracy of the interatomic potentials being employed. The kinematics of the crystal deformation are represented exactly though they are devoid of surface or size effects since the assumption of homogeneous deformation implies that the point of observation experiences ideal bulk surroundings.

2.2.4 Cohesive surface formulation

The description of the cohesive surface formulation is presented in two parts. First, we present the expressions for the element force vector and its consistent tangent stiffness. This element formulation allows all constitutive behavior to be evaluated in a local coordinate frame defined with respect to the deforming surface facets. The following section describes the rate-independent cohesive models used for this body of work.

Element formulation

At every point along a cohesive surface, we define a local coordinate frame which resolves the opening displacements across the surface into normal and shear components. As shown in Figure 2.7, this coordinate frame is not uniquely defined for finite deformations. We

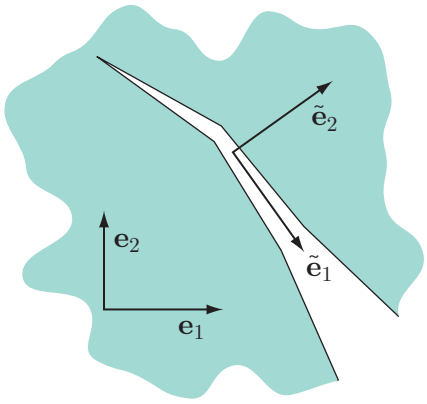

Figure 2.7: Local coordinate frame $\tilde{\mathbf{e}}_i$ constructed along the surface where $\mathbf{e}_i$ is the global cartesian frame.

choose to define this coordinate system with respect to the mid-plane between the displaced surfaces. Alternately, this frame may be fixed to the upper or lower facet. The discussion that follows is independent of the particular choice of local coordinate system though we present specific expressions for the mid-plane. Let the transformation of the gap vector from its representation in the global coordinate frame $\boldsymbol{\Delta}$ to its local representation $\tilde{\boldsymbol{\Delta}}$ in a frame defined with respect to the cohesive surface be given by

$$\tilde{\boldsymbol{\Delta}} = \mathbf{Q}^{\mathrm{T}}\, \boldsymbol{\Delta}. \tag{2.97}$$

The transformation resolves the opening displacement into normal and shear components relative to the current orientation of the surface. This distinction allows for the definition of mixed-mode, surface constitutive relations that show a dependence on the character of the opening displacement. In a variational setting, the contribution to the virtual work from cohesive surface elements is

$$\delta w^{\mathrm{CSE}} = \int_{\Gamma_0} \mathbf{T} \cdot \delta \boldsymbol{\Delta}\, d\Gamma, \tag{2.98}$$

where the integration domain Γ_0 is defined in the undeformed configuration and $\delta\boldsymbol{\Delta}$ is the variation in the surface opening displacement. We review the formulation of several surface constitutive models in Section 2.2.4. The discussion that follows applies to all displacement-driven cohesive relations $\tilde{\mathbf{T}}(\tilde{\boldsymbol{\Delta}})$ defined in the local surface frame. From (2.97), the traction in the global coordinate frame is given by the transformation

$$\mathbf{T} = \mathbf{Q}\, \tilde{\mathbf{T}}. \tag{2.99}$$

With these preliminaries, we derive the expressions for the element level nodal force and stiffness contributions arising from discretization of the cohesive surfaces. Assuming the displacement field is expressed in terms of an expansion of nodal values and shape functions, the opening displacement vector may be written as

$$\begin{aligned} \boldsymbol{\Delta}(\boldsymbol{\xi}) &= \mathbf{u}^{+}(\boldsymbol{\xi}) - \mathbf{u}^{-}(\boldsymbol{\xi}) \\ &= \sum_{A \in N^{+}} \Phi_A(\boldsymbol{\xi})\, \mathbf{u}_A - \sum_{A \in N^{-}} \Phi_A(\boldsymbol{\xi})\, \mathbf{u}_A, \end{aligned} \tag{2.100}$$

where $\mathbf{u}^{+}$ and $\mathbf{u}^{-}$ denote the displacement fields of the upper and lower surfaces, respectively, defined by sets of nodes N^{+} and N^{-}, Φ_A is the shape function associated with local node A on upper or lower surface, $\mathbf{u}_A$ is the nodal displacement, and $\boldsymbol{\xi}$ are coordinates parametrizing the surface. This expression for the opening displacement and the expressions for the nodal force and stiffness that follow are valid within a framework using standard finite element shape functions as well as a framework using meshfree shape functions. In terms of the variation in the nodal displacements $\mathbf{u}_A$, we can rewrite the work increment (2.98) as

$$\delta w_A^{\mathrm{CSE}} = \mathbf{f}_A^{\mathrm{CSE}} \cdot \delta \mathbf{u}_A, \tag{2.101}$$

where the components of the nodal force

$$f_{rA}^{\mathrm{CSE}} = \int_{\Gamma_0} \frac{\partial \Delta_i}{\partial u_{rA}} \, Q_{ij} \, \tilde{T}_j \, d\Gamma \tag{2.102}$$

only receive contributions from cohesive surfaces that fall within the support of node A and

$$\frac{\partial \Delta_i}{\partial u_{jA}} = \begin{cases} \frac{\partial \Phi_A}{\partial \xi} \, \delta_{ij} & \text{for } A \in N^+, \\ -\frac{\partial \Phi_A}{\partial \xi} \, \delta_{ij} & \text{for } A \in N^- \end{cases} \tag{2.103}$$

follows from the definition of the opening displacement (2.100).

The transformation to a representation of the displacement jump and tractions in a coordinate frame fixed to the current configuration of the surfaces is often neglected in an analog to small strain bulk deformation. Though omitting this changing transformation reduces computational effort, the resulting nodal forces will be incorrect in situations for which the surfaces undergo appreciable reorientation due to local crack tip deformations or rigid rotations of the entire body. Tracking the current orientation of the surfaces adds relatively little complication of the element force vector, but produces a considerable increase in the complexity of the tangent stiffness. Not only does the transformation introduce additional contributions to the stiffness, but the resulting matrix is not symmetric.

The tangent stiffness matrix is derived from the linearization of (2.102) as

$$\delta \mathbf{f}_A^{\mathrm{CSE}} = \mathbf{K}_{AB}^{\mathrm{CSE}} \delta \mathbf{u}_B \tag{2.104}$$

where

$$\begin{aligned} \left[\mathbf{K}_{AB}^{\mathrm{CSE}}\right]_{rs} &= \frac{\partial f_{rA}^{\mathrm{CSE}}}{\partial u_{sB}} \\ &= \int_{\Gamma_0} \frac{\partial \Delta_i}{\partial u_{rA}} \left(\frac{\partial Q_{ij}}{\partial u_{sB}} \, \tilde{T}_j + Q_{ij} \, \frac{\partial \tilde{T}_j}{\partial \tilde{\Delta}_k} \, \frac{\partial \tilde{\Delta}_k}{\partial u_{sB}} \right) d\Gamma. \end{aligned} \tag{2.105}$$

From (2.97), we may write

$$\frac{\partial \tilde{\Delta}_i}{\partial u_{sA}} = \frac{\partial Q_{ji}}{\partial u_{sA}} \, \Delta_j + Q_{ji} \, \frac{\partial \Delta_j}{\partial u_{sA}}. \tag{2.106}$$

Substituting (2.106) into (2.105), the tangent may be expressed as

$$\begin{aligned} \left[\mathbf{K}_{AB}^{\mathrm{CSE}}\right]_{rs} = \int_{\Gamma_0} \Bigg(& \frac{\partial \Delta_p}{\partial u_{rA}} \, Q_{pi} \, \frac{\partial \tilde{T}_i}{\partial \tilde{\Delta}_j} \, Q_{qj} \, \frac{\partial \Delta_q}{\partial u_{sB}} \\ & + \frac{\partial \Delta_p}{\partial u_{rA}} \, Q_{pi} \, \frac{\partial \tilde{T}_i}{\partial \tilde{\Delta}_j} \, \frac{\partial Q_{qj}}{\partial u_{sB}} \, \Delta_q \\ & + \frac{\partial \Delta_i}{\partial u_{rA}} \, \frac{\partial Q_{ij}}{\partial u_{sB}} \, \tilde{T}_j \Bigg) \, d\Gamma. \end{aligned} \tag{2.107}$$

In order to complete the formulation of $\mathbf{K}_A^{\mathrm{CSE}}$, we need to derive an expression for the third-rank tensor $\frac{\partial \mathbf{Q}}{\partial \mathbf{u}_A}$. In two dimensions, the transformation tensor $\mathbf{Q}$ may be expanded as

$$Q_{ij}^{\mathrm{2D}} = \hat{t}_i\, \delta_{1j} + \hat{n}_i\, \delta_{2j}, \tag{2.108}$$

where the unit tangent direction in the deformed configuration

$$\hat{\mathbf{t}} = \frac{\mathbf{t}}{|\mathbf{t}|} \tag{2.109}$$

is defined from the jacobian of the surface parametrization

$$\mathbf{t}(\xi) = \frac{\partial \mathbf{x}(\xi)}{\partial \xi}. \tag{2.110}$$

The mid-plane surface is

$$\mathbf{x}(\xi) = \frac{1}{2}\left(\sum_{A \in N^+} \Phi_A(\xi)\ \mathbf{x}_A + \sum_{A \in N^-} \Phi_A(\xi)\ \mathbf{x}_A \right), \tag{2.111}$$

where the nodes on upper and lower facets of the element are denoted by N^+ and N^- as in (2.100) and the current coordinates are defined with respect to the undeformed coordinates $\mathbf{X}_A$ as

$$\mathbf{x}_A = \mathbf{X}_A + \mathbf{u}_A. \tag{2.112}$$

From (2.111), the tangent (2.110) may be expanded as

$$\mathbf{t}(\xi) = \frac{1}{2}\left(\sum_{A \in N^+} \frac{\partial \Phi_A}{\partial \xi}\, \mathbf{x}_A + \sum_{A \in N^-} \frac{\partial \Phi_A}{\partial \xi}\, \mathbf{x}_A \right). \tag{2.113}$$

The normal direction may be written as

$$\hat{\mathbf{n}} = \begin{bmatrix} 0 & -1 \\ 1 & 0 \end{bmatrix} \hat{\mathbf{t}} = \mathbf{Q}^{(\frac{\pi}{2})}\, \hat{\mathbf{t}}. \tag{2.114}$$

From (2.108) and (2.114), we can therefore express $\frac{\partial \mathbf{Q}}{\partial \mathbf{u}_A}$ needed in (2.107) for the two-dimensional case as

$$\frac{\partial Q_{ij}^{\mathrm{2D}}}{\partial u_{kA}} = \frac{\partial \hat{t}_i}{\partial u_{kA}}\, \delta_{1j} + Q_{ir}^{(\frac{\pi}{2})}\, \frac{\partial \hat{t}_r}{\partial u_{kA}}\, \delta_{2j}, \tag{2.115}$$

where

$$\frac{\partial \hat{t}_i}{\partial u_{kA}} = \left[\frac{\partial}{\partial \mathbf{u}_A} \frac{\mathbf{t}}{|\mathbf{t}|} \right]_{ik} = \frac{1}{|\mathbf{t}|}\left(\frac{\partial t_i}{\partial u_{kA}} - \hat{t}_i\, \frac{\partial t_r}{\partial u_{kA}}\, \hat{t}_r \right). \tag{2.116}$$

The derivative of the tangent $\mathbf{t}$ follows from (2.113) as

$$\frac{\partial \mathbf{t}}{\partial \mathbf{u}_A} = \frac{1}{2}\,\frac{\partial \Phi_A}{\partial \xi}\,\mathbf{1}. \tag{2.117}$$

In three dimensions, the transformation tensor $\mathbf{Q}$ may be expanded as

$$Q_{ij}^{\mathrm{3D}} = \hat{t}_i^{(1)}\,\delta_{1j} + \hat{t}_i^{(2)}\,\delta_{2j} + \hat{n}_i\,\delta_{3j}, \tag{2.118}$$

where the local normal direction $\hat{\mathbf{n}}$ and the two tangent directions $\hat{\mathbf{t}}^{(1)}$ and $\hat{\mathbf{t}}^{(2)}$ are defined using the parameterization of the surface with respect to $\boldsymbol{\xi} = [\xi\ \eta]^{\mathrm{T}}$. At any point on the surface, two tangential, but not necessarily orthogonal, directions are defined by the columns of the surface jacobian

$$\mathbf{m}^{(1)}(\boldsymbol{\xi}) = \frac{\partial \mathbf{x}(\boldsymbol{\xi})}{\partial \xi} \qquad \text{and} \qquad \mathbf{m}^{(2)}(\boldsymbol{\xi}) = \frac{\partial \mathbf{x}(\boldsymbol{\xi})}{\partial \eta}. \tag{2.119}$$

Using the mid-plane construction, we can expand these tangent directions as

$$\mathbf{m}^{(1)}(\boldsymbol{\xi}) = \frac{1}{2}\left(\sum_{A\in N^+} \frac{\partial \Phi_A(\xi,\eta)}{\partial \xi}\,\mathbf{x}_A + \sum_{A\in N^-} \frac{\partial \Phi_A(\xi,\eta)}{\partial \xi}\,\mathbf{x}_A\right) \tag{2.120}$$

and

$$\mathbf{m}^{(2)}(\boldsymbol{\xi}) = \frac{1}{2}\left(\sum_{A\in N^+} \frac{\partial \Phi_A(\xi,\eta)}{\partial \eta}\,\mathbf{x}_A + \sum_{A\in N^-} \frac{\partial \Phi_A(\xi,\eta)}{\partial \eta}\,\mathbf{x}_A\right) \tag{2.121}$$

Using these results, we can construct the unit normal to the surface as

$$\hat{\mathbf{n}} = \frac{\mathbf{n}}{|\mathbf{n}|} = \frac{\mathbf{m}^{(1)} \times \mathbf{m}^{(2)}}{|\mathbf{m}^{(1)} \times \mathbf{m}^{(2)}|}, \tag{2.122}$$

and the remaining, mutually orthogonal, directions are chosen as

$$\hat{\mathbf{t}}^{(1)} = \frac{\mathbf{m}^{(1)}}{|\mathbf{m}^{(1)}|} \tag{2.123}$$

$$\hat{\mathbf{t}}^{(2)} = \hat{\mathbf{n}} \times \hat{\mathbf{t}}^{(1)}. \tag{2.124}$$

In order to derive an expression for $\frac{\partial \mathbf{Q}^{\mathrm{3D}}}{\partial \mathbf{u}_A}$ from (2.118), we need the derivatives of each of the directions (2.122)–(2.124) with respect to $\mathbf{u}_A$. The derivatives of the coordinate directions are given by

$$\frac{\partial \hat{t}_i^{(1)}}{\partial u_{kA}} = \frac{1}{|\mathbf{m}^{(1)}|}\left(\frac{\partial m_i^{(1)}}{\partial u_{kA}} - \hat{t}_i^{(1)}\,\frac{\partial m_r^{(1)}}{\partial u_{kA}}\,\hat{t}_r^{(1)}\right), \tag{2.125}$$

$$\frac{\partial \hat{t}_i^{(2)}}{\partial u_{kA}} = \epsilon_{irs}\left(\frac{\partial \hat{n}_r}{\partial u_{kA}}\hat{t}_s^{(1)} + \hat{n}_r\frac{\partial \hat{t}_s^{(1)}}{\partial u_{kA}}\right), \text{ and} \tag{2.126}$$

$$\frac{\partial \hat{n}_i}{\partial u_{kA}} = \frac{1}{|\mathbf{n}|}\left(\frac{\partial n_i}{\partial u_{kA}} - \hat{n}_i\,\frac{\partial n_r}{\partial u_{kA}}\,\hat{n}_r\right), \tag{2.127}$$

where ϵ_{ijk} is the permutation symbol defined by

$$\epsilon_{ijk} = \begin{cases} 1 & \text{for even permutations of } i,\ j, \text{ and } k, \\ -1 & \text{for odd permutations of } i,\ j, \text{ and } k, \\ 0 & \text{otherwise} \end{cases} \tag{2.128}$$

and the derivatives of the tangent vectors (2.119) are

$$\frac{\partial \mathbf{m}^{(1)}}{\partial \mathbf{u}_A} = \frac{1}{2}\frac{\partial \Phi_A}{\partial \xi}\mathbf{1} \qquad \text{and} \qquad \frac{\partial \mathbf{m}^{(2)}}{\partial \mathbf{u}_A} = \frac{1}{2}\frac{\partial \Phi_A}{\partial \eta}\mathbf{1}. \tag{2.129}$$

The expression for $\frac{\partial \mathbf{n}}{\partial \mathbf{u}_A}$ in (2.127) follows from the definition of $\mathbf{n}$ in (2.122) as

$$\frac{\partial n_i}{\partial u_{kA}} = \epsilon_{irs}\left(\frac{\partial m_r^{(1)}}{\partial u_{kA}} m_s^{(2)} + m_r^{(1)}\frac{\partial m_s^{(2)}}{\partial u_{kA}}\right). \tag{2.130}$$

With these results, the formulation of the element level nodal force vector and consistent tangent matrix is complete. These expressions are valid for cohesive surfaces within a standard finite element framework.

Cohesive surface relations

The element formulation presented in Section 2.2.4 makes use of a local coordinate frame defined with respect the deforming facets of the cohesive surface. This construction allows all surface constitutive relations to define the evolution of the local traction $\tilde{\mathbf{T}}$ with respect to the local opening displacement $\tilde{\boldsymbol{\Delta}}$, while the kinematics of large deformation and surface rotations are accounted for at the element level. For the case of an elastic, or reversible, cohesive relation, the traction is derived from a free energy potential φ as

$$\tilde{\mathbf{T}} = \frac{\partial \varphi}{\partial \tilde{\boldsymbol{\Delta}}} \tag{2.131}$$

while the surface stiffness may be expressed as

$$\frac{\partial \tilde{\mathbf{T}}}{\partial \tilde{\boldsymbol{\Delta}}} = \frac{\partial^2 \varphi}{\partial \tilde{\boldsymbol{\Delta}} \partial \tilde{\boldsymbol{\Delta}}}. \tag{2.132}$$

Throughout this section we will use φ to denote a cohesive potential. Using (2.132), we see that the first term contributing to the element stiffness (2.107) is symmetric, while the remaining terms are generally nonsymmetric.

Chapter 3

Nanoindention of Au

3.1 Background

The indentation of a crystal by a hard, nanometer-sized object is a benchmark problem for determining critical energies and stresses needed for defect creation and propagation within materials. Indentation has been rigorously treated in isotropic elasticity [61] and extensively studied in experiments at the nanoscale [62, 63, 64]. Few of these experiments have produced information about the initial formation of dislocation loops, which signifies the onset of plasticity. Kiely *et al.* [65] have experimentally observed that surface steps play a role in the development of dislocations as the amount of load necessary to create dislocations lessens when the indenter is close to these steps. Our objective is to use atomistic simulation to gain knowledge about how surface geometry affects dislocation formation. We perform a series of simulations of a Au(111) crystal with indentation at various distances from a surface step. A new deformation parameter, the slip vector, is used to quantify the dislocation content of nanoindentation defects. It is used with the atomic stress fields to determine the critical amount and direction of resolved shear stress (CRSS) necessary for dislocation nucleation. Our simulations reveal that physical contact between an indenter and a surface step explains the drop in indentation force when the indenter is close to the step, altering the details of dislocation nucleation without necessarily changing the magnitude of the CRSS. This magnitude is observed to vary only in cases of high deformation or where the crystallography conflicts with the surface step geometry. A contact-based geometrical expression is used to explain both simulation results and experimental data.

A number of simulations of nanoindentation have been performed in recent years. Robertson and Fivel [66] compared dislocations produced from experimental nanoindentation of Cu(100) with those seen in a dislocation dynamics simulation with boundary conditions dictated by isotropic elasticity and the finite element method. At the atomic scale, Tadmor *et al.* [67, 68] used the quasicontinuum method to study two dimensional nanoindentation from a rigid punch. These simulations led to several insights about the contribution of image forces and surface energies to dislocation nucleation; however, the types of dislocations formed were restricted by the geometry of the simulation region. These restrictions no doubt alter any

estimation of the CRSS. Kelchner, Plimpton and Hamilton [35] used a repulsive potential to model a spherical indenter penetrating the passivated surface of a Au(111) crystal modeled with the embedded atom method (EAM) [23]. This work showed that complex dislocation loops formed within the crystal and grew to intercept the crystal surface. Visualization of dislocations and stacking faults, a difficult task accomplished by only a few researchers [69], was achieved by the development of the centrosymmetry parameter.

3.2 Indentation of Au(111)

3.2.1 Simulation set-up

In this work, atomistic simulations of nanoindentation were performed on a 199 Å wide by 400 Å long by 125 Å thick single crystal containing approximately 560,000 atoms. The top surface was traction free and contained a step one atomic layer in height through the width. The bottom surface was held fixed while periodic boundary conditions were applied to the side surfaces. The crystal was composed of gold modeled with EAM potentials [23]. The FCC crystal was oriented such that the top surface was the (111) plane, and the step was oriented along the $\left[1\bar{1}0\right]$ direction, perpendicular to the $\left[11\bar{2}\right]$ direction. Two different step orientations were used, (A) $\langle 110\rangle$ / $\{100\}$ and (B) $\langle 110\rangle$ / $\{111\}$ [70], because of the three-fold symmetry of the (111) surface. The same repulsive potential used in [35] emulated a spherical indenter of tip radius $R = 40$ Å. The indentations were performed quasistatically at zero temperature using the conjugate gradient method [11] to minimize the system's potential energy. The indenter was lowered in increments ranging from 0.1 to 0.5 Å. The indenter center was positioned at various distances d from the surface step, on both the low and high sides, respectively defined as $d < 0$ and $d > 0$.

3.2.2 Indentation results

In the simulations, data were calculated for several force-depth curves, such as those seen in Figure 3.1. For distances far from the step where $|d| \geq 20$ Å, elastic Hertzian behavior persists until a yield load F_y is reached at a penetration depth δ_y and dislocations are nucleated upon further loading. This nucleation is characterized by a drop of 30 to 40 % in indentation load. Although their elastic responses are identical, once dislocations are generated the load behavior differs for A- and B-steps due to the difference in the orientation of their slip systems. Similar behavior is seen for indentation near a surface step, although a reduced stiffness is observed and either a small drop of less than 15% in load or an appreciable change in slope of the force-depth curve characterizes the yield load. Figures shown in this report will display data both at loads corresponding to the "initial event", which indicates the first formation of dislocations, and at load drops. The features shown in Figure 3.1 are qualitatively similar to those seen in experiment [65], although load drops for indentation far from a step are more extreme in experiment, producing nearly complete unloading.

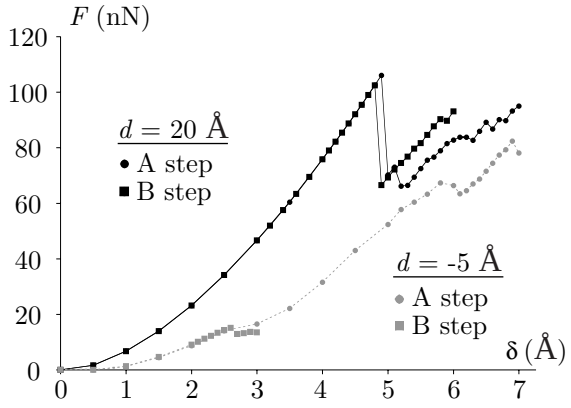

Figure 3.1: Indentation force as a function of depth for both types of steps at different distances from the step.

When indenting far from a step, F_y approximately equals 105 nN. F_y decreases when the indenter is centered less than 20 Å from the step, down to values between 10 and 20 nN. The lowest yield loads are observed when -10 Å $\leq d \leq 0$. To interpret this behavior, the surfaces of these systems were viewed with atoms colored according to whether or not they were in contact with the indenter tip. A few of these images are shown in Figure 3.2, and reveal that a portion of the contact area lies on the step when the indenter is positioned on

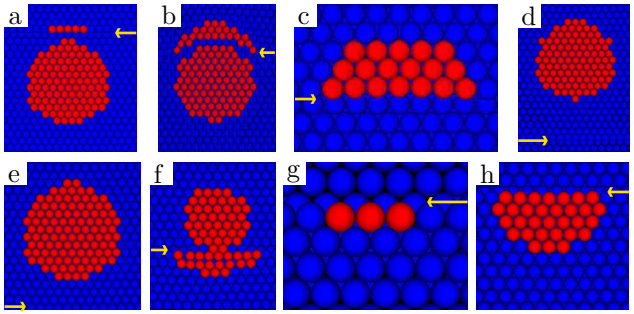

Figure 3.2: Contact area at the yield load for the A-step at distances d = (a) -20 Å, (b) -10 Å, (c) -5 Å, (d) 30 Å and for the B-step at distances d = (e) -30 Å, (f) -10 Å, (g) -5 Å, (h) 0. Yellow arrows highlight the position of the step line.

the low side of the step. For $|d| \leq 20$ Å, contact with the step alters the load necessary to nucleate dislocations. The most extreme situations occur in frames (c) and (g) of Figure 3.2, in which all of the initial contact occurs on the step edge, although the indenter is centered off-step. These images were used to estimate the contact area and a contact radius a_y at the onset of dislocation formation. Figure 3.3 shows F_y as a function of distance from the step normalized by a_y. F_y decreases abruptly at normalized distances closer than 1.5, with the most prominent effects felt at distances closer than or equal to 1.

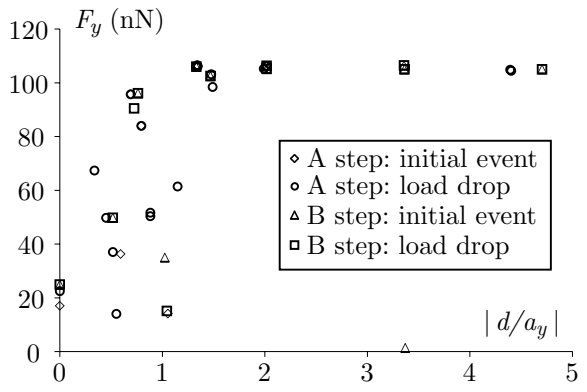

Figure 3.3: Indenter load at initial plasticity events and load drops as a function of distance from the step normalized by contact radius.

Figures 3.2 and 3.3 suggest caution should be used when estimating contact area in order to calculate mean pressure beneath the indenter, $\sigma_y = F_y \,/\, \left(\pi\, a_y^2\right)$. Experimental measurements [65] showed σ_y decreasing significantly for values of $|d/a_y| < 3$, indicating a long-range effect of the step. However, those values were obtained by calculating contact area with the Hertzian relation $a_y = \sqrt{R\delta_y}$. Use of this relation at the nano-scale is questionable, as a_y is not so well defined near a step. This is clearly observed in Figure 3.4, which compares A- and B-step data with the Hertzian relation. Although some of the points do coincide with

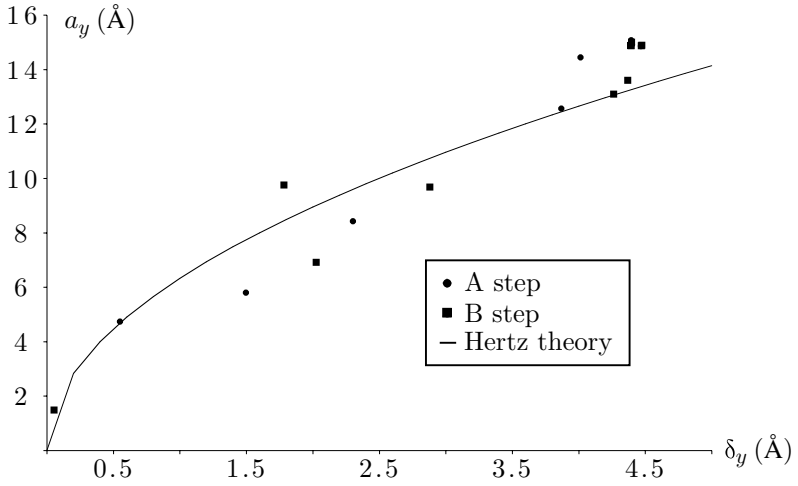

Figure 3.4: Contact radius as a function of indentation depth at the yield load. The Hertzian relation is shown as a solid curve for comparison.

the Hertzian curve, most do not. These values of a_y calculated in our simulations show that although the surface step causes a significant variation in the values of σ_y for normalized distances less than 1.5, this variation does not necessarily show a downward trend as $|d/a_y|$ approaches zero, as seen in Figure 3.5.

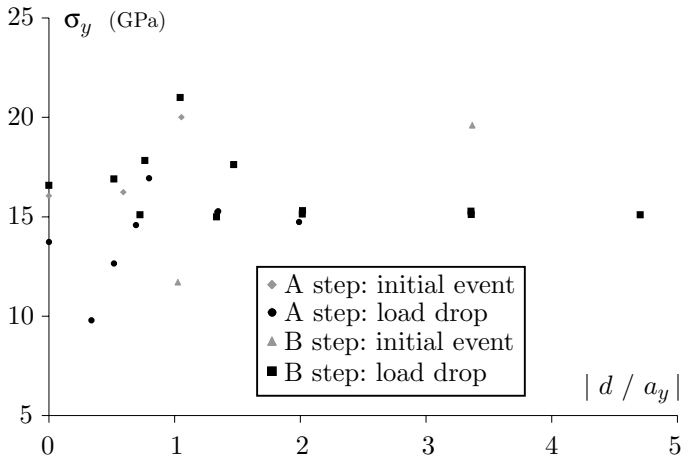

Figure 3.5: Mean pressure beneath the indenter at the yield load as a function of distance from the step normalized by contact radius.

The experiments mentioned above used steps that varied in height from 5 to 30 Å. The distance from the step at which a spherical indenter first contacts both the planar surface and the step edge, d_c, can be geometrically estimated to equal $d_c = \sqrt{2Rh - h^2}$, where h denotes the step height. The purpose of determining d_c is to show that if a step effect, such as a load drop, is noticed at $d < d_c$, the effect is due to direct contact between the indenter and the step. If such an effect is noticed at $d > d_c$, then contact alone cannot account for it. For our simulations, if the undeformed value of $h = 2.36$ Å is used, $d_c = 13.5$ Å. However, if an "effective" height $h_e \equiv h + \delta_y$ is used and $\delta_y = 4.4$ Å, then $d_c = 22.2$ Å. This agrees with the observations of both step types in Figure 3.2 which show no contact at $d = -30$ Å but some contact at $d = -20$ Å. When $d \approx d_c$, $a_y \approx 15$ Å and $|d_c/a_y| = 1.48$. Experimental values of $R = 2300$ Å, $h = 28$ Åand $\delta_y = 34$ Åfor the near-step indentation shown in Figure 2(b) of [65] yield $d_c = 358$ Å using h and 530 Å using h_e, both of which are larger than the measured distance $d = 300$Å. Thus, the estimate of d_c shows that the indenter actually hits the step, acting as a stress concentrator, rather than the step having a long-range effect. Using the Hertzian relation produces $a_y = 280$ Å and $|d_c/a_y| = 1.28$ if h is used or $|d_c/a_y| = 1.9$ if h_e is used.

3.2.3 Dislocation structure

Analysis of the dislocation structures produced during indentation leads to a greater understanding of their nucleation. Figure 3.6 displays typical dislocation loops produced after the load drop for indentation far from the steps. The slip vector magnitude in stacking fault regions, colored green, is 1.662 Å, which is very close to the value for a $\langle 112 \rangle$ partial dislocation in gold (1.666 Å), and the value in regions traversed by a full dislocation, colored red, lies between 2.7 and 3.0 Å, consistent with the magnitude of a $\langle 110 \rangle$ vector (2.885 Å). Slip vector components allow identification as to which specific partial dislocation is nucleated

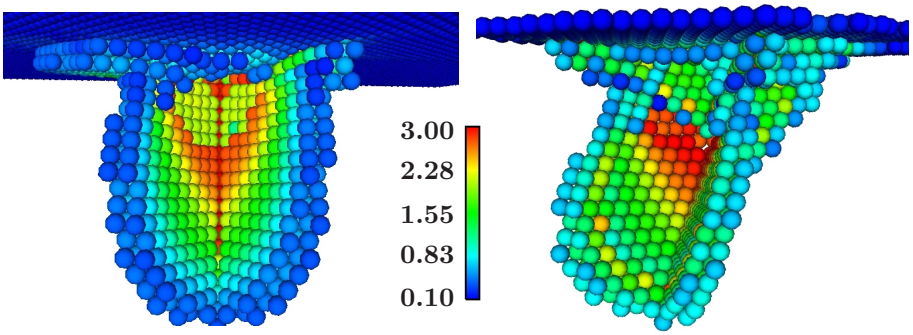

Figure 3.6: Dislocation loops nucleated for indentation far from the surface steps, with atoms colored by $|\boldsymbol{s}^{\alpha}|$.

on a $\{111\}$ plane. Alteration of indenter position results in some variation in the number and size of loops produced, as observed in Figure 3.7.

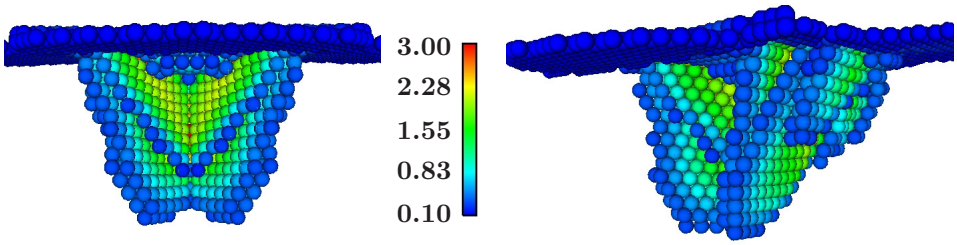

Figure 3.7: Dislocation loops nucleated for indentation far from the surface steps, with atoms colored by $|\boldsymbol{s}^{\alpha}|$.

The planes on which dislocation loops develop change as the indenter approaches the step. Figure 3.8 shows dislocation structures nucleated when the indenter is at $d = -5$ Å and at $d = 0$. Images for the A-step show a loop formed on the $(\overline{1}\overline{1}1)$ plane, the inclined plane intersecting the surface along the step edge direction, $[1\overline{1}0]$. Although loops grow on this plane for both distances, the slip direction is $[\overline{2}1\overline{1}]$ for $d = -5$ Å and $[1\overline{2}\overline{1}]$ for $d = 0$. For the B-step, the $(\overline{1}\overline{1}1)$ plane is oriented opposite to the way it is for the A-step. Thus, the resulting structures possess radically different shapes which are several atomic layers thick and oriented in the inclined $[\overline{1}\overline{1}0]$ direction, coinciding with most of the atoms' slip vectors. Clearly, the structures that have developed near the surface step are highly influenced by the crystal orientation. A complete record of which partial and full Burgers vectors are created for each simulation series can be found in Tables 3.1 and 3.2. For simplicity, the nomenclature of the Thompson tetrahedron [71] is used to represent the $(\bar{1}1\bar{1})$ $[\alpha]$, $(1\bar{1}\bar{1})$ $[\beta]$, $(\bar{1}\bar{1}1)$ $[\gamma]$ and (111) $[\delta]$ planes.

Table 3.1: Dislocations nucleated for the A-step simulations.

d (Å)	$\mathbf{b}_{\text{partial}}$	$\mathbf{b}_{\text{full}}$
-30	$\alpha\,[1\bar{1}\bar{2}]\,,\beta\,[\bar{1}1\bar{2}]$	
-20	$\alpha\,[\bar{2}\bar{1}1]\,,\beta\,[\bar{1}1\bar{2}]\,,\beta\,[\bar{1}\bar{2}1]$	$\alpha\beta\,[\bar{1}\bar{1}0]$
-10	$\alpha\,[1\bar{1}\bar{2}]\,,\alpha\,[\bar{2}\bar{1}1]\,,\beta\,[\bar{1}1\bar{2}]\,,\beta\,[\bar{1}\bar{2}1]$	
-5	$\gamma\,[\bar{2}1\bar{1}]$	
0	$\alpha\,[1\bar{1}\bar{2}]\,,\gamma\,[1\bar{2}\bar{1}]$	$\alpha\gamma\,[0\bar{1}\bar{1}]$
5	$\alpha\,[1\bar{1}\bar{2}]\,,\gamma\,[1\bar{2}\bar{1}]$	$\alpha\gamma\,[0\bar{1}\bar{1}]$
10	$\beta\,[\bar{1}1\bar{2}]\,,\gamma\,[\bar{2}1\bar{1}]$	$\beta\gamma\,[\bar{1}0\bar{1}]$
20	$\alpha\,[1\bar{1}\bar{2}]\,,\alpha\,[\bar{2}\bar{1}1]\,,\beta\,[\bar{1}1\bar{2}]\,,\beta\,[\bar{1}\bar{2}1]$	$\alpha\beta\,[\bar{1}\bar{1}0]$
30	$\alpha\,[1\bar{1}\bar{2}]\,,\alpha\,[\bar{2}\bar{1}1]\,,\beta\,[\bar{1}1\bar{2}]\,,\beta\,[\bar{1}\bar{2}1]$	$\alpha\beta\,[\bar{1}\bar{1}0]$

Table 3.2: Dislocations nucleated for the B-step simulations.

d (Å)	$\mathbf{b}_{\text{partial}}$	$\mathbf{b}_{\text{full}}$
-70	$\alpha\,[1\bar{1}\bar{2}]\,,\alpha\,[\bar{2}\bar{1}1]\,,\beta\,[\bar{1}1\bar{2}]\,,\beta\,[\bar{1}\bar{2}1]\,,\delta\,[\bar{1}\bar{1}2]$	$\alpha\beta\,[\bar{1}\bar{1}0]\,,\beta\delta\,[0\bar{1}1]$
-50	$\alpha\,[1\bar{1}\bar{2}]\,,\alpha\,[\bar{2}\bar{1}1]\,,\beta\,[\bar{1}1\bar{2}]\,,\beta\,[\bar{1}\bar{2}1]\,,\delta\,[\bar{1}\bar{1}2]$	$\alpha\beta\,[\bar{1}\bar{1}0]\,,\beta\delta\,[0\bar{1}1]$
-30	$\alpha\,[1\bar{1}\bar{2}]\,,\alpha\,[\bar{2}\bar{1}1]\,,\beta\,[\bar{1}1\bar{2}]\,,\beta\,[\bar{1}\bar{2}1]\,,\delta\,[\bar{1}\bar{1}2]$	$\alpha\beta\,[\bar{1}\bar{1}0]\,,\beta\delta\,[0\bar{1}1]$
-20	$\alpha\,[1\bar{1}\bar{2}]\,,\alpha\,[\bar{2}\bar{1}1]\,,\beta\,[\bar{1}1\bar{2}]\,,\beta\,[\bar{1}\bar{2}1]\,,\delta\,[\bar{1}\bar{1}2]$	$\alpha\beta\,[\bar{1}\bar{1}0]$
-10	$\alpha\,[1\bar{1}\bar{2}]\,,\alpha\,[\bar{2}\bar{1}1]$	$\alpha\beta\,[\bar{1}\bar{1}0]\,,\alpha\delta\,[\bar{1}01]$
-5		$\boldsymbol{s}\sim[\bar{1}\bar{1}0]$
0		$\boldsymbol{s}\sim[\bar{1}\bar{1}0]$
5	$\alpha\,[\bar{2}\bar{1}1]\,,\beta\,[\bar{1}\bar{2}1]$	$\alpha\beta\,[\bar{1}\bar{1}0]\,,\gamma\delta\,[1\bar{1}0]$
10	$\alpha\,[\bar{2}\bar{1}1]\,,\beta\,[\bar{1}\bar{2}1]\,,\delta\,[\bar{1}2\bar{1}]\,,\delta\,[2\bar{1}\bar{1}]$	$\alpha\beta\,[\bar{1}\bar{1}0]$
20	$\alpha\,[\bar{2}\bar{1}1]\,,\beta\,[\bar{1}\bar{2}1]$	$\alpha\beta\,[\bar{1}\bar{1}0]$
30	$\alpha\,[\bar{2}\bar{1}1]\,,\beta\,[\bar{1}1\bar{2}]\,,\gamma\,[\bar{1}\bar{1}\bar{2}]$	
50	$\alpha\,[\bar{2}\bar{1}1]\,,\beta\,[\bar{1}\bar{2}1]\,,\gamma\,[\bar{2}1\bar{1}]$	

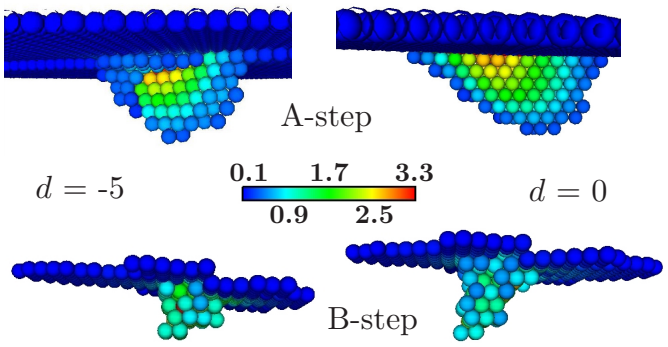

Figure 3.8: Dislocation loops nucleated for indentation close to the surface steps, with atoms colored by $|\boldsymbol{s}^{\alpha}|$.

3.2.4 Dislocation nucleation

The slip vector is used with the atomic stress tensor to estimate the CRSS required for dislocation nucleation. Most nanoindentation research has used either the maximum RSS or the largest RSS for a $\langle 110 \rangle$ or $\langle 112 \rangle$ direction. However, the slip vectors measured in our simulations show that while slip does occur in $\langle 112 \rangle$ directions, the direction of slip rarely corresponds to the direction of the largest RSS. For indentation far from a step, the atomic RSS for slip directions reaches a maximum of 3.26 GPa prior to dislocation nucleation, even though a higher value of 6.32 GPa occurs for a different $\langle 112 \rangle$ direction. Slip occurs in the lower RSS direction due to a lower energy barrier for sliding of atomic layers past one another. The height of this barrier, known as the unstable stacking fault energy γ_{us} [72], has been shown to be asymmetric with regard to the direction of slip [73]. The orientation of our crystal is such that slip occurs when the RSS is 3.26 GPa in the direction of this lower energy barrier. Thus, any nucleation criteria within a material model should not only contain a critical amount of stress, but also the direction and sense of the slip.

The CRSS observed far from a step is nearly constant for distances as close as 5 to 10 Å from the step. This can be observed in Figure 3.9. Data for the A-step show a decrease in this value, down to 2.21 GPa, for the simulations where $|d| \leq 5$ Å, which may be caused by the very large deformations which affect γ_{us} [74], or by image force effects that are more prominent when dislocation nucleation occurs at a step edge [73]. Near the step, the B-step data show a higher CRSS for cases in which the slip direction is not a $\langle 112 \rangle$ direction, as depicted in Figure 3.8. Nevertheless, our observations show that the value of CRSS remains roughly constant for similar types of slip directions even though the specific combination of slip plane and Burgers vectors changes.

The value of CRSS far from the step is very close to the theoretical shear strength of this EAM potential, $\frac{\mu}{2\pi} = 3.66$ GPa. Experimentally determined estimates of the CRSS range from 1.5 to 2 GPa [62, 63], roughly half the value observed in simulation. This level of agreement is significant considering that experimental dimensions and loads are 2 to 3 orders of magnitude higher than those used in simulation. Any discrepancy may be

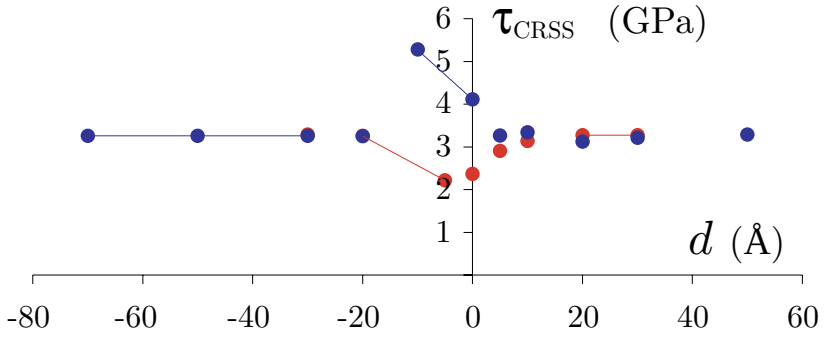

Figure 3.9: Critical atomic resolved shear stress as a function of distance from the step. A-step data is shown in red, while B-step data is blue.

due to a size scale effect, which would lead to a more inhomogeneous deformation state beneath the indenter, and influence the degree that image forces affect nucleation. Our simulations were performed at zero temperature, whereas the experiments referenced were done at room temperature. The effect of temperature on the dislocation nucleation process is not well-understood. In both experimental [75] and theoretical [76, 77] studies, stacking fault energies show little dependence on temperature below 400 K. However, theoretical models of dislocation emission from a crack tip show a definitive relationship between activation energy and temperature [76, 34]. Although further study of finite temperature dislocation formation is warranted, our results can be considered a successful first attempt at understanding the mechanics of dislocation emission during nanoindentation, and how surface geometry affects this process.

Some of our simulations were repeated using EAM potentials[78] that produce a value for intrinsic stacking fault energy, γ_{sf}, closer to the experimental value of 32–33 mJ/m^2 [79, 80, 81]. These simulations show little difference, $\lesssim 13$ %, in the experimentally relevant quantities of F_y and δ_y as compared with the original runs, and display the same step effect. This is because the value for γ_{us} is almost identical for the two potentials, 103 and 102 mJ/m^2, both of which compare well with the density functional theory prediction of 140 mJ/m^2. Only characteristics related to γ_{sf}, such as partial dislocation loop size, differ between simulations. This can be observed in Figures 3.10 and 3.11, which show dislocation structures for both the original and the modified potential.

3.2.5 Comparison of atomistic and continuum simulations of nanoindentation

Finite element simulations of indentation of a flat surface were performed in order to determine the accuracy of nonlinear constitutive models. A thorough study of nanoindentation requires simulating systems with the same dimensions as in experiment. One way to treat larger systems while still retaining the ability to represent the underlying crystal structure is to couple atomistic and continuum simulation methods [82, 83], provided the continuum

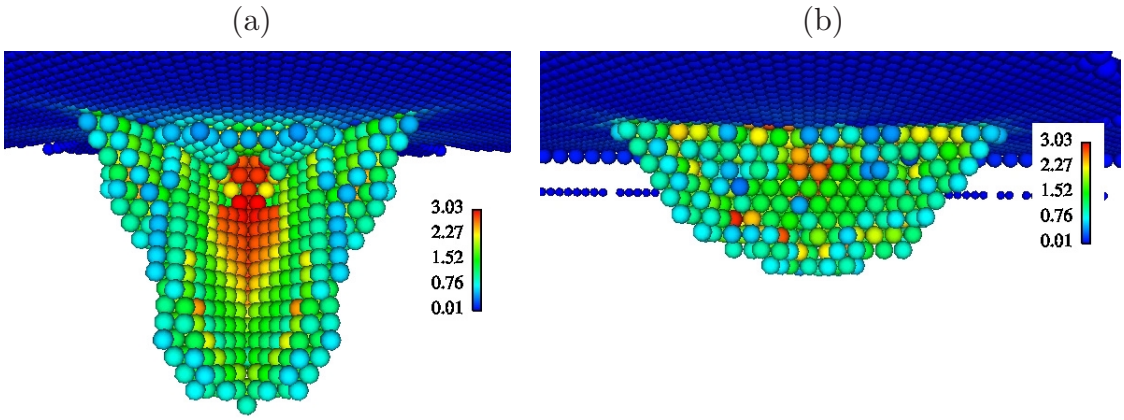

Figure 3.10: Dislocation loops due to indentation far from the A-step using the (a) original and (b) modified EAM potentials.

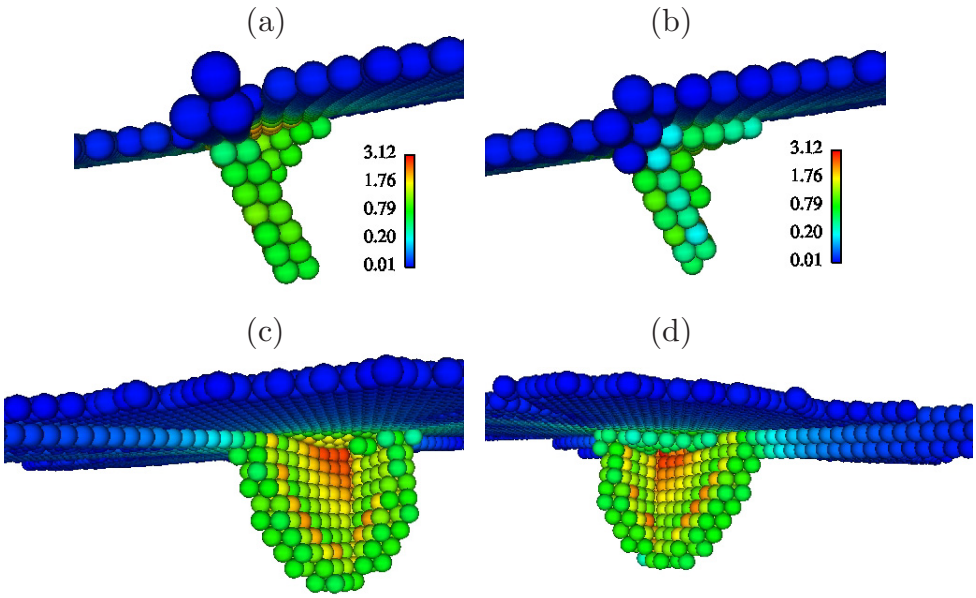

Figure 3.11: Dislocation loops due to indentation on the A-step using the (a),(c) original and (b),(d) modified EAM potentials. (a),(b) show the initial loops to form while (c),(d) show the loops created upon additional loading.

mechanical model can produce deformations consistent with those in the atomistic region. This is accomplished by using a nonlinear elastic constitutive model incorporating the same embedded atom potentials used in the atomistic simulation. Determining energies, stresses and elastic moduli is done by using the Cauchy-Born (C-B) rule [40, 42], which equates the strain energy density at the continuum scale with the energies of interatomic bonds present in a unit cell of the deformed underlying microstructure. The continuum scale deformation gradient prescribes the deformation of the interatomic bonds and is assumed to be homogeneous over the representative unit cell.

Figure 3.12 compares the finite element calculations with the atomistic simulations of nanoindentation far from a surface step. Figure 3.12(a) shows that the load-indentation

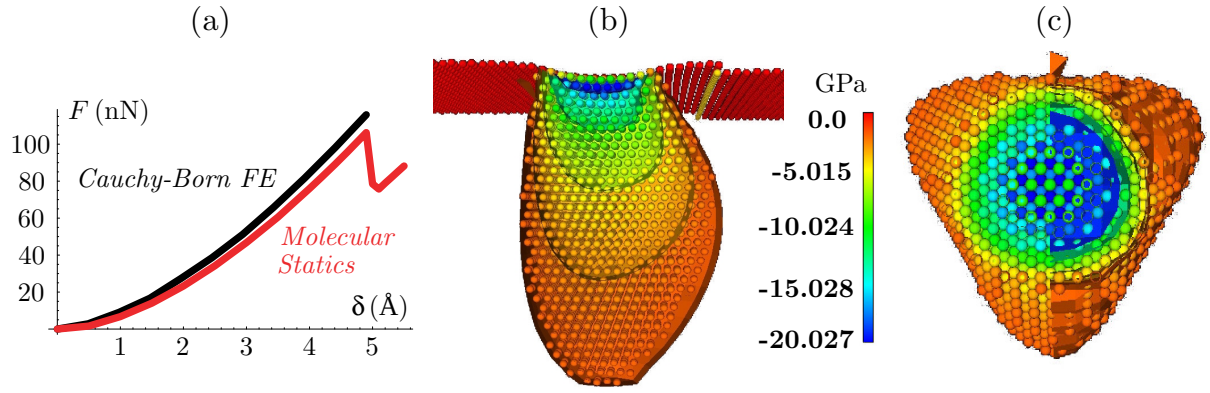

Figure 3.12: (a) Indentation force as a function of depth for Cauchy-Born finite element and atomistic simulations. (b) Cross-sectional and (c) top, excluding surface atoms, views of superposed atomistic and finite element contours of the normal component of the stress tensor in the indentation direction.

depth curves are very similar to one another, only deviating significantly for loads close to dislocation nucleation. For example, the continuum analysis predicts a load of 116 nN at the same depth for which the atomistic calculation yields $F_y = 105$ nN, a difference of only 10 %. This deviation may be due to the fundamental assumption of the C-B rule that the deformation is homogeneous for the crystal lattice that underlies each continuum point. This condition is violated in the highly deformed region beneath the indenter. The element dimension in this region is the roughly the same as the lattice constant for gold, 4.08 Å, and further mesh refinement would be inconsistent with the assumptions used to derive the constitutive relations.

Contours of the normal stress in the indentation direction are shown in Figures 3.12(b) and (c). The finite element calculation is observed to reproduce the anisotropic character of the stress contours as well as the values of stress for very close distances to the contact area. There is some disagreement in the maximum stress, as the atomic stress is at its largest values for atoms in the second atomic layer rather than at the free surface itself. A better

measure of stress at free surfaces in atomistic simulations is needed in order to determine the accuracy of the finite element calculation.

3.3 Indentation of Au(001)

We can verify that our simulation methods produce reasonable results by comparing dislocation structures appearing in simulations with equivalent structures observed in experiments. Comparison between the two is only possible by increasing the experimental resolution around a nanoindentation point down to the atomic scale.

The experiments used to evaluate our simulation methods were performed in ultra high vacuum conditions on a Au(001) crystal cleaned by repeated sputtering and annealing in a system described in more detail elsewhere [2]. Nanoindentations were done pushing the tungsten tip against the sample for distances of a few nanometers from the stable tunnel distance with the control feedback switched off. The last layer of the Au(001) surface is reconstructed with the well known "hex" 5×20 reconstruction which appears in STM images as fringes oriented along a $\langle 110 \rangle$ direction. These fringes arise from a Moiré-like effect between the topmost layer with an hexagonal arrangement and the lower bulk-like layer with square symmetry.

A typical image of the surface of the crystal after performing nanoindentations is shown in Figure 3.13. Indentations themselves are imaged as multi-storied pits, and some material

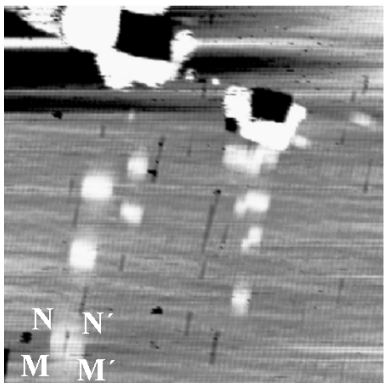

Figure 3.13: (98×98 nm^2) STM image of two nanoindentations in the Au(001) surface. Rows of hillocks stemming from the nanoindentation points and following a $\langle 110 \rangle$ direction are visible. Bumps of pile-up material surround nanoindentation points (the contrast in these bumps is saturated to enhance the visibility of the hillocks). Capital letters on one of the hillocks are used to compare their orientations with the ones in Figure 3.14.

is shown as a pile-up surrounding the pits. Rows of bump-like features with a height of 0.6 ± 0.1 Å, called from now on hillocks, are apparent along the compact $\langle 110 \rangle$ directions on the (001) surface, at distances of hundreds of nanometers from the indentation points.

We have also observed similar hillocks in the course of ion irradiation on both Au(001) and Ag(001) followed by gentle annealing: in these cases the hillock distribution is random, with no alignments in rows as the ones surrounding nanoindentations.

Close-up STM images of hillocks are shown in Figure 3.14 together with an interpretation of their sub-surface structure[2], which consists of two stacking faults on intersecting {111} planes each bounded by two parallel Shockley partial dislocations. The whole configuration

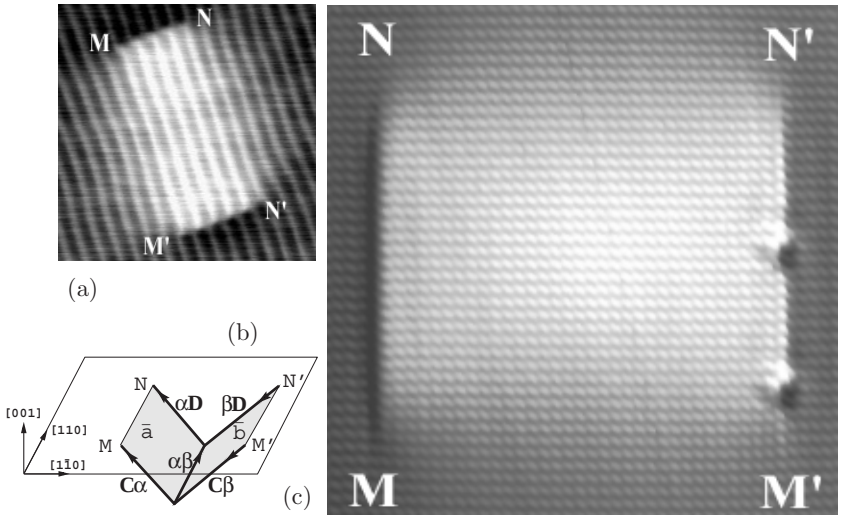

Figure 3.14: (a) (25×25 nm^2) STM image in Au(001) of a hillock, such as seen near nanoindentation points. (b) Scheme of the dislocation configuration proposed for dissociated loops. Burgers vectors in the Thompson tetrahedron notation and line directions are shown for each segment. (c) (11.6×11.6 nm^2) A hillock in a Ag(001) surface previously ion-bombarded and annealed. Note the atomic resolution and the positions of the emerging partial dislocations.

is held up by a stair-rod dislocation parallel to the surface. We argue that the origin of the hillocks can be traced to perfect dislocation loops that are punched into the crystal by the tip displacement into the surface [84]. In our case, a family of such dislocation loops would consist of V-shaped half-loops intersecting the surface with Burgers vector parallel to the latter. They would, on energetic grounds, be split into two pairs of Shockley partials giving rise to the configuration shown in Figure 3.14b, *i.e.* resulting in hillocks[85]. We can ascertain that these loops are of interstitial character based on the fact that for Au (Figure 3.14(a)) we observe a missing reconstruction fringe on top of the hillock. As the interatomic spacing of the substrate is larger than the one of the uppermost reconstructed layer, the position of the missing fringe in the Moiré-like pattern[86] corresponds to the position of the extra row of interstitial atoms below. Furthermore, for the Ag(001) atomic resolution image of Figure 3.14c, it is clear that each partial dislocation produces a mismatch of one half interatomic unit between the rows on both sides of each stacking fault, the two mismatches adding up to one extra row of atoms in the inner side of the hillock.

To gain insight into the atomic processes involved in the creation of these hillocks, atomistic simulations[87] were carried out. A repulsive potential[35] was used to model a spherical indenter of radius 40 Å penetrating the surface of a Au(001) crystal modeled with the embedded atom method potential [23]. The reconstructed layer is thought to behave like a floating layer [88]. Thus, it is not expected to affect dislocation generation and behavior during nanoindentation and was not included in the simulations. A top view of the surface after quasistatic nanoindentation is shown in Figure 3.15. In agreement with experiment, it

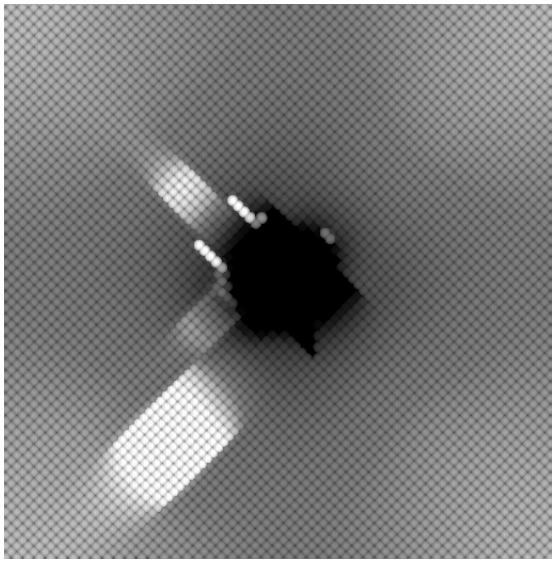

Figure 3.15: Top view of the nanoindentation simulation. The dark region in the middle of the picture corresponds to the indentation point. Two hillocks are emitted along ⟨110⟩ directions. Note the striking similarity of these simulated defects with the experimental image of Figure 3.14c.

is observed that two hillocks have been generated around the nanoindentation trace.

The spatial distribution of the slip vectors moduli $|\mathbf{s}_i|$ around the nanoindentation trace, with a suitable color scale, is shown in Figure 3.16. The configuration shown in Figure 3.16, with a height displacement for the topmost atoms of 0.6 Å, strikingly reproduces the previously proposed subsurface structure of a hillock.

A dynamical picture of the process is obtained by recording successive frames of the simulated atomic events, as shown in Figure 3.17. To obtain the sequence, the indenter is first lowered in increments of 0.1 Å down to a depth of 5.8 Å in a quasistatic way at zero temperature. At this point dislocation loops are observed below the indenter, in agreement with previous results[35]. Then, a constant energy molecular dynamics simulation follows the evolution of the system for 36 ps. A different dislocation configuration is created close to the tip and, then, glides away in a ⟨110⟩ direction. We stress that, although the experimentally observed hillocks are usually much larger than the simulated ones and the indentation itself is

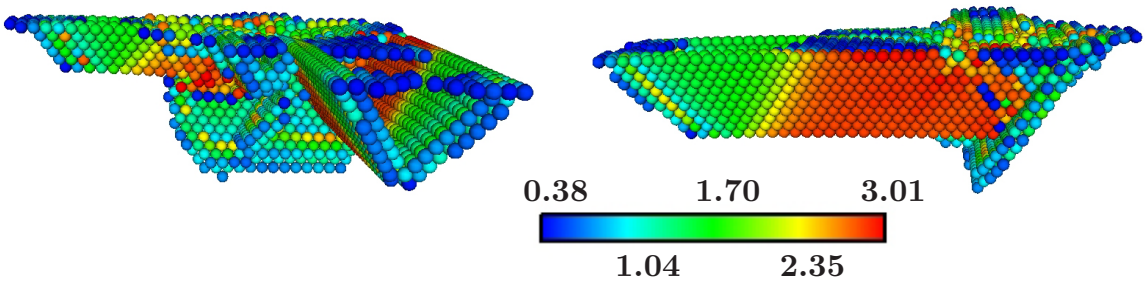

Figure 3.16: 3D simulation views from different orientations of the dissociated dislocation loop, corresponding to the sub-surface configuration of Figure 3.15, colored according to the slip vector. Atoms which signify a stacking fault plane are colored green. Blue and yellow atoms define the core of the leading and trailing partial dislocations, respectively. Red designates atoms which have slipped a full $\langle 110 \rangle$ vector.

also much deeper, we do observe hillocks of the same size in both experiment and simulation.

Hillocks are seen to glide as a whole unit. This behavior can be understood on the grounds that Shockley partial dislocations bounding a stacking fault are expected to glide easily on the {111} gliding planes. In our simulation they indeed glide away dragging with them the stair-rod dislocation. The motion of structures formed by stair-rod dislocations and Shockley partial dislocations in thin films has been recently reported [89]. We argue that the rows of hillocks appearing in the STM image of Figure 3.13 are the result of successive emission of loops that glide away from the nanoindentation trace. Once started into motion due to the high stress close to the indentation, the hillocks would glide away from the indentation point until they collide or interact with other defects in the crystal. The simulation cell is too small to observe in detail this effect, although the hillocks move with a constant velocity within the unit cell once they are far enough from the indentation point. Hillock like structures, although interpreted in a different way, have been observed to drift in highly stressed regions[90]. The creation of hillocks following ion irradiation can also be explained in terms of the above model: after long ion irradiation and further annealing, the surface is known to exhibit a multi-storied pit structure [91], whereas the presence of a large supersaturation of adatoms, isolated atoms lying on the crystal's surface, and, probably, subsurface interstitials, is suspected. These extra-atoms can cluster on crystallographic planes and, after relaxation, give rise to perfect loops that start the above mechanism.

In the course of the many simulations performed, a variety of hillock structures has been found. They differ in the exact arrangement of the loop below the surface: more complex configurations than the simplest one observed in Figure 3.16, an edge V-shaped loop dissociated along {111} planes, are possible. But the defining characteristics are the same for all of them: the Burgers vector of the undissociated loop is a lattice vector, all the sections of the loop appear dissociated along {111} planes, and the loop glides as a whole

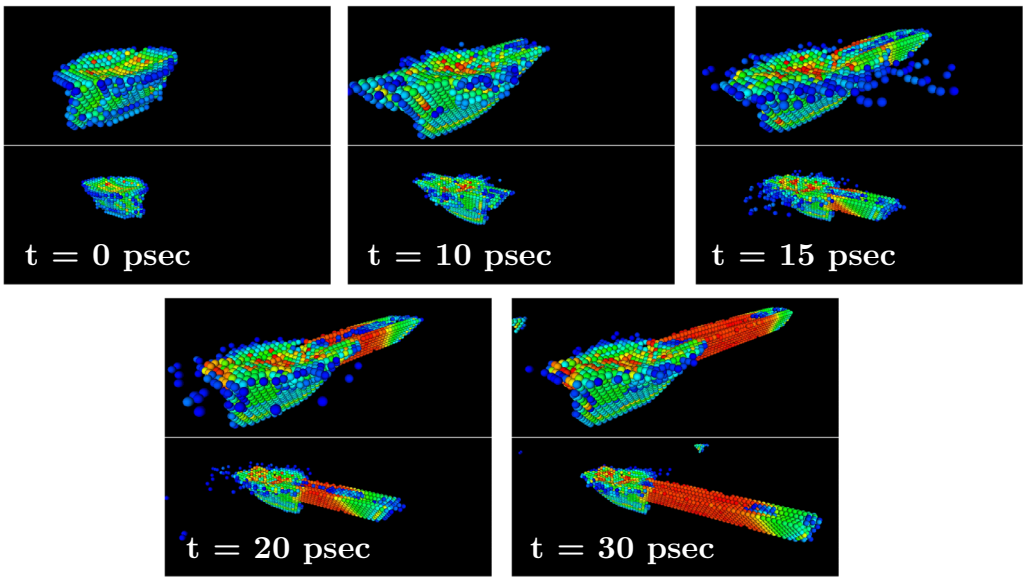

Figure 3.17: Frames from the molecular dynamics simulation showing the creation and movement of the extended dislocation.

unit in a $\langle 110 \rangle$ direction. It is also worth remarking that, in the simulations, the hillocks remain in place once the tip is retracted from the surface, in agreement with the experiment.

Comparing different experimental images, it is observed that the size distribution of both the span s, the distance between stacking faults at the surface, and width w, the separation between partial dislocations again at the surface, of the observed hillocks is rather broad, ranging from a lowest resolvable size of about one reconstruction period ($\sim$ 14 Å) to a size of several ones. However, the parameter w, the width of the extended dislocation, is experimentally seen to level off with increasing span s of the hillock. The repulsive interaction force between two Shockley partial dislocation segments, at a given distance, increases initially with segment length, proportional to the observed span, but attains a constant value when this length becomes much larger than the distance between the segments. Within a model using elemental dislocation theory[71] and taking into account image dislocations to include the effect of the free surface, the exact form of the $w(s)$ curve can be predicted and is found to be in agreement with the experimental data. It is worth emphasizing that the parameters of Burgers vectors, geometry, etc., of this new configuration can be explained in terms of continuum dislocation theory.

Chapter 4

Nanoindentation of Glass

The IFM has been used in a nanoindentation mode only for ductile metals coated with self-assembled monolayers. In order to gain some experience with the nanoindentation behavior of a brittle material, we chose to make initial measurements on a sodium silicate glass. This material is known for its slow crack-growth behavior in the presence of water, *i.e.* stress-corrosion cracking, and was considered a good starting point for experimentation. The experiments were done in liquid water with a tungsten probe electrochemically etched to have a parabolic end form, which turned out to have a tip radius of $\sim$ 4000 Å. Initial measurements were in the form of force profiles, or loading curves, which involved hovering on the surface at a light load, pulling back about 250 Å and then approaching the surface at a constant rate of approximately 50 Å/sec up to a predetermined load, after which, the tip was withdrawn at the same rate. A typical example is shown in Figure 4.1, taken to a maximum load of 120 μN, which results in an average applied stress of 6 GPa. Any kind of

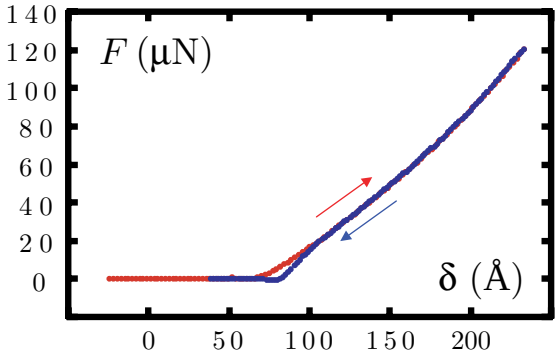

Figure 4.1: A force profile taken to 120 μN at a speed of 50 Å/sec. The red curve is for approach and the blue for retraction. No hysteresis is seen between the two curves indicating no permanent deformation has occurred

load relaxation during this profile, like cracking, would result in a hysteresis loop between the approach and withdrawal curves. No such hysteresis is seen in Figure 4.1, except for a

region of about 25 Å near the initial contact. This behavior is probably due to the viscous draining of the water from under the tip as it approaches compared to the similar draining drag in replacing it as it retracts.

Slow crack-growth systems, however, usually require some nucleation time. Thus, we decided to change strategy and look at extended-time creep experiments. This measurement involves initially hovering on the surface at a light load and then suddenly increasing the normal force to a selected value while recording the tip position required to maintain the load. The technique allows a direct measure of the relaxation process. An example of this type of measurement for several maximum-load values is shown in Figure 4.2. These curves, surprisingly, indicate that after the tip displaced into the sample by about 75Å in order to

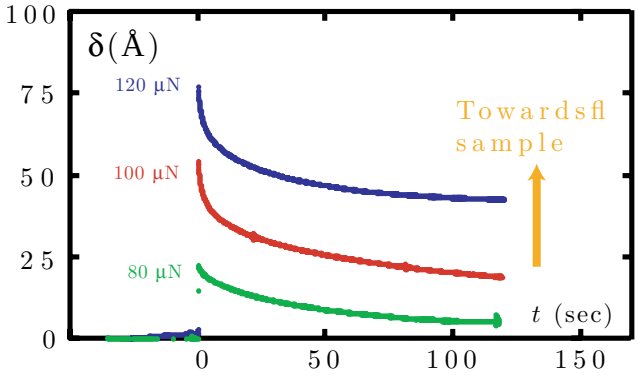

Figure 4.2: Creep curves for three values of constant maximum load. The tip's vertical position needed to maintain the load is recorded as a function of time. Positive values indicate that the tip is moving into the sample.

initially establish the 120 μN load, it retracted by about 25 Å over a period of approximately 120 sec. Ordinarily, as the sample relaxes, by crack or dislocation nucleation, the tip moves further into the sample in order to maintain the constant load. However, in this case, it pulls back by about one third of the initial deformation. Regardless of this peculiar behavior, the results clearly indicate that some relaxation phenomena process has taken place. In order to visualize just what has happened, we take constant repulsive-force images of the surface after each relaxation event shown in Figure 4.2 and these results are shown in Figure 4.3.

Figure 4.3 represents the constant repulsive images of the surface after each of the creep measurements shown in Figure 4.2. The lateral range is 5000 × 5000 Å and the vertical range of the skirt is 100Å. Figure 4.4 shows the result of a line scan across the middle of each crack. The approximate values of the widths and depths of each crack are indicated on the figure. The first thing to note is that the cracks all have the same orientation. This probably reflects some level of residual stress in the surface of the glass, which has a preferential direction. In addition, we see that there is a considerable swelling of the edges of the crack amounting to ∼25Å for the maximum load of 120 μN. This agrees reasonably well with the observation of the relaxation observed in Figure 4.2. It is clear that as the crack forms, there is considerable swelling of the material around the edges of the crack. This is a very strange

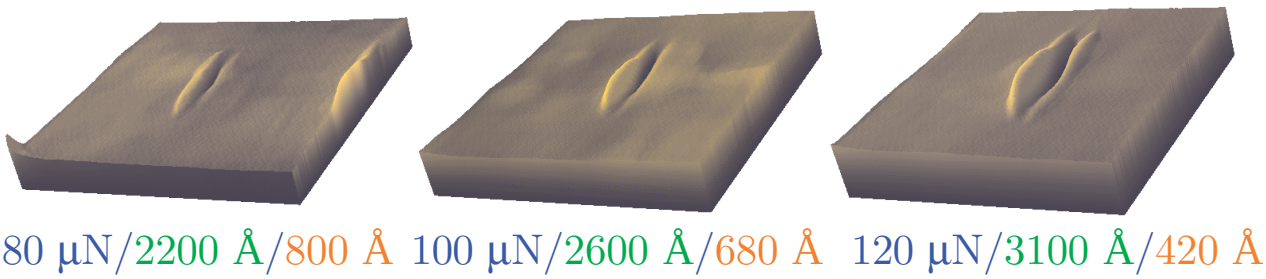

Figure 4.3: 5000 Å × 5000 Å constant repulsive-force images of the surface after each of the creep measurements shown in Figure 4.2. The vertical scale is 100 Å for the skirt. The label for each graph provides the applied force, the crack length and the contact diameter.

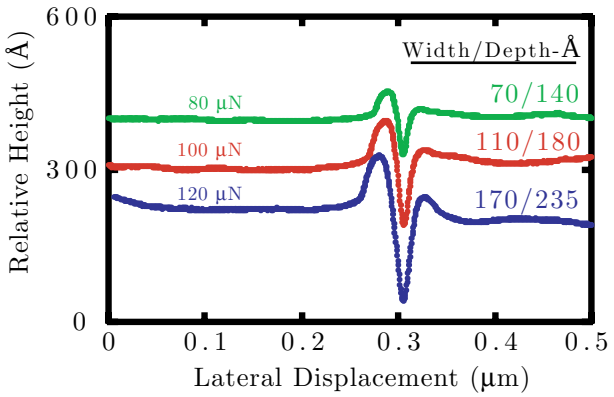

Figure 4.4: Constant repulsive-force line scans across the center of the cracks shown in Figure 4.3. The approximate widths and depths are indicated for each crack.

effect that has not been observed before, as far as we know.

It is clear from these results that this choice of material was not a good one for comparison with sophisticated theoretical modeling. First, because the effect observed is largely a chemical one and second because the crack nucleation and growth involves a second-order process, the swelling effect. While the results are fascinating, they are not appropriate for comparison between atomistic and continuum calculations of the cracking phenomenon. A second material, MgO, was chosen because cracking under nanoindentation had already been observed by others and adequate potentials for atomic-level modeling were available. The modeling results are covered in the next section of this report.

This page intentionally left blank.

Chapter 5

Nanoindentation of MgO

Chapter 3 showed that the simulation of nanoindentation on a metal surface produced $\langle 110 \rangle$ and $\langle 112 \rangle$ dislocations. These dislocations, as well as associated surface hillocks, are the only defects to appear in atomistic simulations. Our original thought was that surface steps would act as stress concentrators and lead to fracture within the material. Since this was found not to be true, we turned our attention to the nanoindentation of a brittle material. Examples of materials that exhibit brittle behavior, fracture to form free surfaces, rather than ductile deformation, plasticity-the production and motion of dislocations, at moderate temperatures include ceramics, *e.g.* SiO_2, Al_2O_3, and Si_3N_4, and ionic crystals, *e.g.* MgO, NaCl, and CsCl. It was decided that further experimental and simulation efforts would study the nanoindentation of MgO in order to examine the mechanisms operating at the initiation of brittle fracture.

5.1 Background

The initiation of cracks by means of indentation of a glass or ceramic material is a complex picture. The structure of these cracks have dependencies not only on the indented material, but also indenter shape, indentation rate, ambient temperature and loading/unloading sequence. A review of experimental indentation cracking can be found in [92]. Crack structures typically observed have been categorized by the following labels: conical, radial, half-penny, median and lateral. Figure 5.1 shows radial cracks formed by micro-scale indentation of a float glass [93]. This indentation was performed using a Vickers indenter at room temperature. Cracks also appeared for cases where the ambient temperature was as high as 600°C. Additionally, permanent depressions are formed on the glass surface. Similar experiments [92] have shown that for amorphous glasses, fracture occurs during unloading rather than loading of the indenter. For crystalline materials, radial cracks are noticed to form during loading of the indenter. Other experiments indicate that the shape of the indenter also plays a role in determining crack structure. Sharp indenters form radial cracks, while blunt indenters initially form conical cracks and, upon excessive loading, radial cracks.

Indentation of MgO crystals has been performed at both the micro- and nano-scales

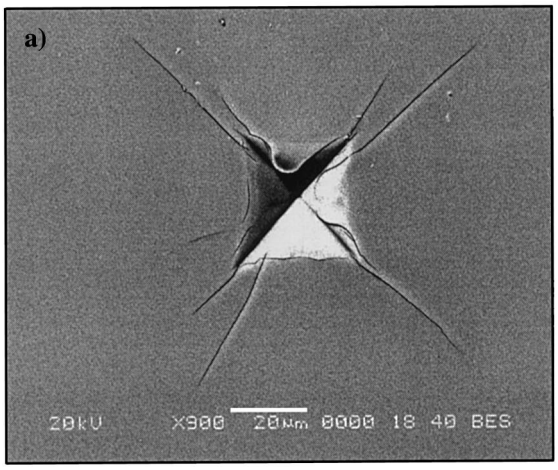

Figure 5.1: Indentation of standard float glass (SiO_2 72; Na_2O 13.4; CaO 9.6; MgO 4; Al_2O_3 0.6 wt.%) at room temperature. [Le Bourhis & Metayer, 2000]

[94, 95, 96, 97, 98, 99, 100]. MgO is a compound formed by ionic bonding, crystals in which the dominant mode of bonding is the transference of a valence, *i.e.* outer shell, electron and electrostatic attraction exists between + and − charged ions. Its structure, depicted in Figure 5.2, is referred to as the NaCl lattice type and consists of an FCC lattice of Mg

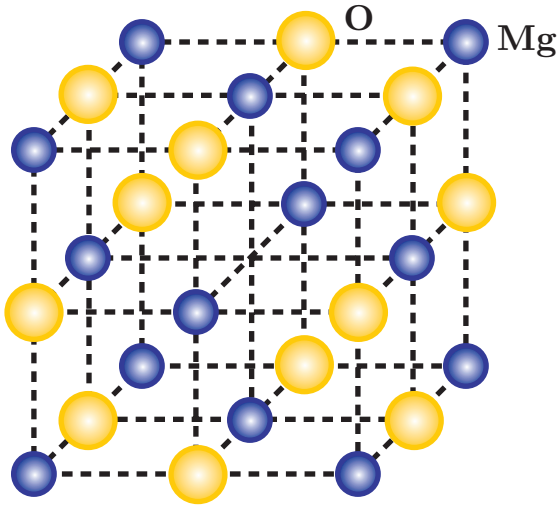

Figure 5.2: Crystal lattice of MgO, a NaCl-lattice type.

atoms, with interstitial O atoms located on side edges of the unit cell. In this arrangement, each atom "sees" six nearest neighboring atoms, all of the opposite type. Severe deformation of MgO crystals causes the creation of both dislocations and cracks. For microindentation, radial cracks are noticed to form along $\langle 110 \rangle$ directions with the crack face forming on a $\{110\}$

plane [95]. Additionally, slip bands are observed along $\langle 100 \rangle$ directions. Nanoindentation experiments primarily show the formation of bands of dislocations [94]. The primary slip systems for NaCl lattices are $\{110\} / \langle 110 \rangle$ and $\{110\} / \langle 100 \rangle$, although other slip directions are sometimes observed, such as $\langle 120 \rangle$ [100]. Other modes of material failure are sometimes observed, such as the pile-up and expulsion of atomic layers of material around the indenter [99]. The variety of modes and structures of material defects seen in experiments shows that nanoindentation of MgO should provide fundamental information on the formation and propagation of these defects.

5.2 Atomistic Simulation

In order to perform the simulation in a reasonable timespan, the potential was changed slightly to reduce the number of interactions calculated. The original form, presented in section 2.1.4, used a value of $R_c = 12.63$ Å. This resulted in $\alpha_D = 3.5/R_c = 0.2772$ $\mathring{A}^{-1}$. Since $a_0 = 4.129795$ Å, $\alpha_D = 1.144/a_0$. Our altered form uses $R_c = 8.5$ Å, reducing the number of neighbors per atom from 957 to 290. Since $\alpha_D = 3.5/R_c$, $\alpha_D = 0.4118$ $\mathring{A}^{-1}$. The new equilibrium lattice parameter is observed to be $a_0 = 4.133122129$ $\mathring{A}$, so $\alpha_D \approx 1.7/a_0$. Wolf *et al.* [27] note that this type of alteration has virtually no effect on the value of the fully converged energy per atom. The change in elastic moduli is small, yielding the new values of $C_{11} = 393.3$ GPa, $C_{12} = C_{44} = 86.3$ GPa and bulk modulus = 189 GPa.

This modified potential was used to do a nanoindentation simulation of a hard sphere of radius 20 Å to indent the (001) surface of a MgO crystal. The size of the crystal was approximately 103 Å × 103 Å × 81 Å (25 × 25 × 20 unit cells of 8 atoms per cell, a total of 100,000 atoms), with periodic boundary conditions used in the "in-plane" dimensions, a fixed surface at the bottom and a free surface at the top of the "out-of-plane" dimension. The indentation is performed dynamically at an effective rate of 0.1 Å/psec, the indenter was lowered 0.1 Å every 10,000 timesteps, with a time step of 0.0001 psec. The force *vs.* depth curve for the dynamic simulations is shown in Figure 5.3. The value at each depth is the average force over the 10,000 steps between depth increments. It can be observed that somewhere between depths of 2.7 Å and 3.0 Å, a failure of the crystal occurs. The atomistic variables of centrosymmetry parameter and slip vector were used to analyze the failed material. Unfortunately, neither dislocations nor crack-like flaws were apparent. Figure 5.4 shows the simulated, nanoindented MgO crystal with atoms colored by centrosymmetry parameter, for only those atoms with a value greater than 0.01. Other than the surface atoms, the atoms that appear have only marginally higher values than 0.01, and no specific type of defects are clearly visible. Examination of the simulation data also included visualizing the top few layers of the crystal. The front and top views of the crystal are shown in Figure 5.5, for which atoms are colored according to height. Although the indentation region is clearly observed, no dislocations can be discerned within the material. Further simulated nanoindentation until definitive defect structures are produced is warranted as future work, and improvement in the atomistic variables of centrosymmetry parameter and slip vector is needed to resolve defects created during dynamic simulations. Time-averaging of these

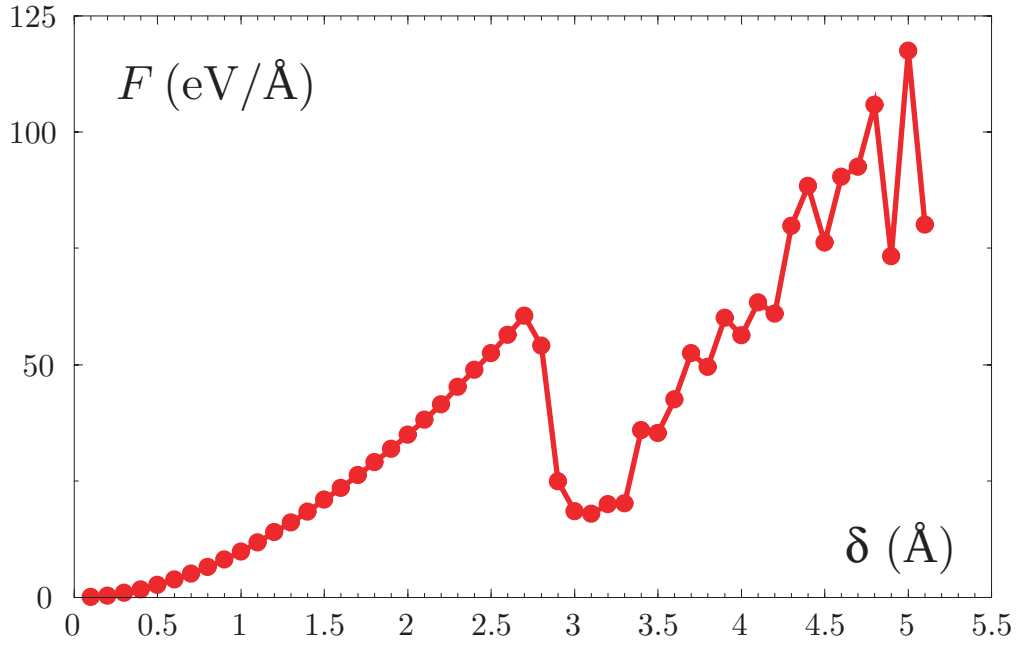

Figure 5.3: Indentation force *vs.* depth curve for the simulated nanoindentation of MgO(100). The rate of indentation $\dot{\delta}$ is 0.1 Å/psec.

quantities will be implemented in future research.

5.3 Experimental Nanoindentation

Single-crystal samples of MgO were obtained and experiments were performed in a dry-air ($\sim$ 5 % RH) environment. MgO is quite hard and it was found that the sharp tungsten tips used for nanoindentation of Au were not strong enough to cause fracture in these samples. A diamond tip was subsequently obtained from a commercial vendor, which was advertised to have a tip radius of 1000 Å.

In actual use, it became obvious that the tip was not only of a larger radius than advertised, but had a more complex shape. Examination of the force *vs.* indentation depth curve, shown in Figure 5.6, shows that the loading appears to be non-Hertzian, and does not produce fracture in this brittle material within the loading limits of the interfacial force microscope (IFM). Analysis of the indenter tip was performed using scanning electron microscopy (SEM). At a magnification of 364× normal size, shown in Figure 5.7, there appears to be irregular facets and bumps on the diamond tip. The complex shape of the indenter is even more apparent at a higher magnification of 25,000×, shown in Figure 5.8. These irregularities effectively make the diamond tip of a much higher radius. The overall result was that our IFM sensor was not able to develop the force necessary to cause fracture.

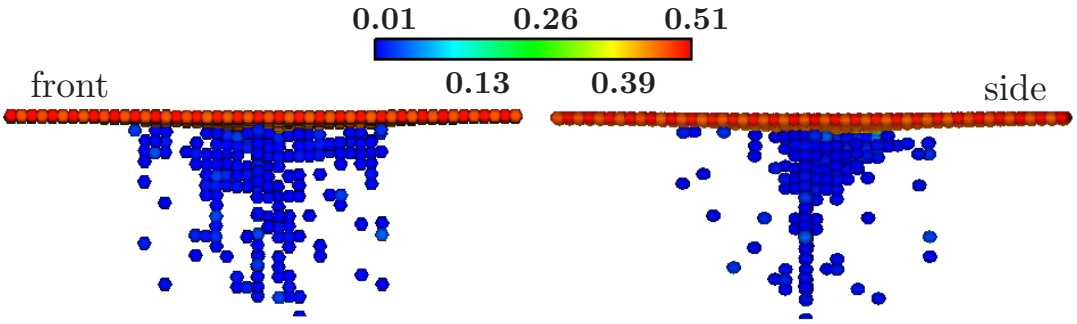

Figure 5.4: Front and side views of top half of the nanoindented MgO crystal. Atoms are colored according to their value of centrosymmetry parameter.

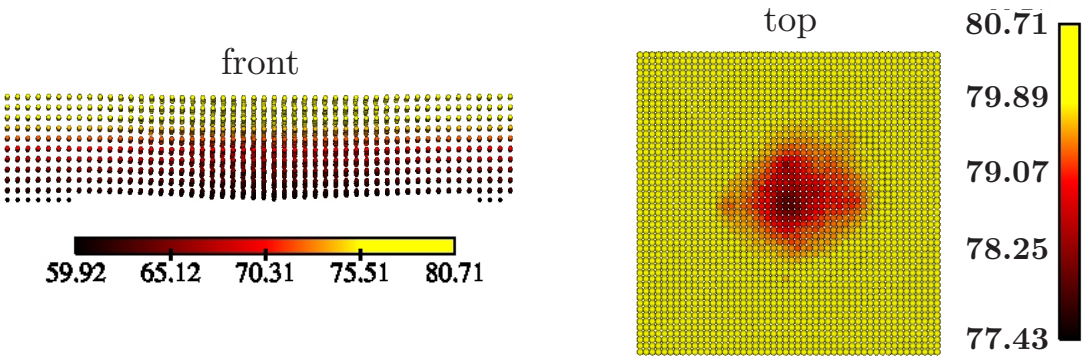

Figure 5.5: Front and top views of uppermost layers of the nanoindented MgO crystal. Atoms are colored according to their height. Note the different scales used for the two figures.

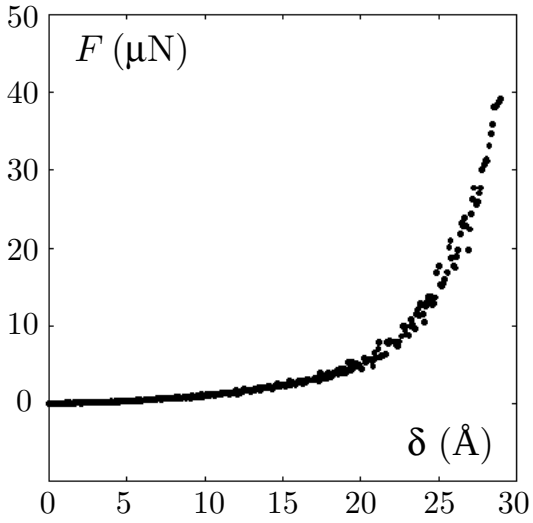

Figure 5.6: Indentation force *vs.* depth curve for nanoindentation of MgO.

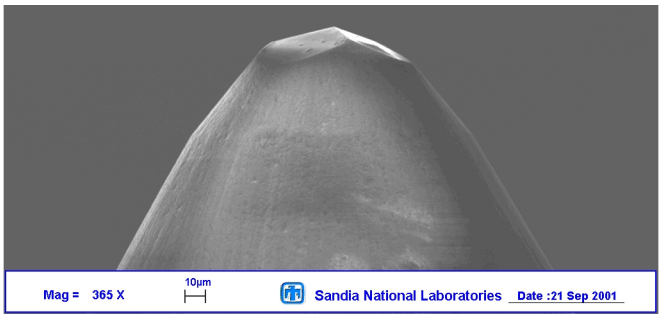

Figure 5.7: A SEM image of the diamond tip used to nanoindent MgO, magnification = 365×.

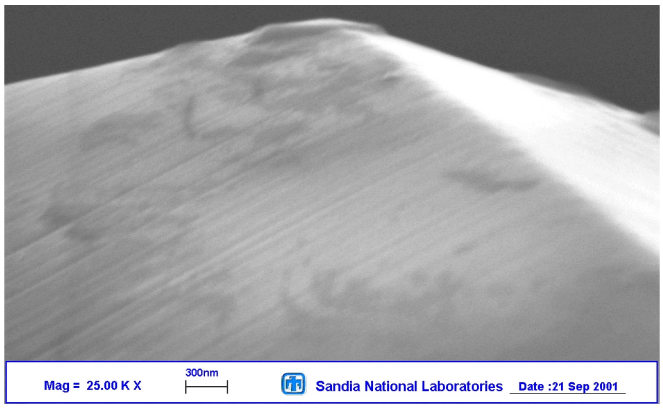

Figure 5.8: A SEM image of the diamond tip used to nanoindent MgO, magnification = 25,000×.

Chapter 6

Steady-State Crack Growth

In this chapter, we compare continuum simulations using a cohesive modeling approach with the predictions of atomistic simulations. As previously stated, cohesive approaches to modeling fracture differ from classical approaches by embedding the physics of the fracture process by means of a traction-separation relationship to provide the constitutive relations for the localized failure mode of deformation. These relations can either be applied to all the material in the system, as in Cauchy-Born elasticity, or as traction-separation relations between discrete material elements, otherwise known as cohesive surface elements. For modeling brittle fracture, the form of these traction-separation relations are typically based on simple physical arguments and motivation from semi-empirical atomistic potentials. First, we derive the parameters for the cohesive relations based on evaluation of Griffiths condition with an atomistic system. We then compare the fracture behavior predicted by this cohesive model with the results of atomistic simulations under quasistatic and dynamic loading conditions. We will discover that while cohesive approaches adequately reproduce the atomistic results under quasistatic loading, dynamic conditions reveal the significant effects dispersion has on the behavior of dynamically propagating cracks.

6.1 Background

6.1.1 Crack propagation in materials

The primary purpose of this project is to model the nucleation and growth of cracks in materials. This subject is not trivial, and has been the focus of studies in experimental, computational and theoretical arenas. Ravi-Chandar and Knauss [101, 102, 103, 104] observed the propagation of cracks in a clear, brittle polymer called "Homalite", noting how the fracture surface has a "mirror-mist-hackle" appearance – first, the crack propagates smoothly (mirror), then begins to oscillate once a speed of approximately 30 % of the Rayleigh wave speed c_R is reached (mist), and finally, oscillates wildly and begins branching once the crack is going a speed approximately 50 % of c_R (hackle). This surface appears in Figure 6.1. Other studies, such as those by Fineberg *et al.* [105, 106], have also examined the behavior

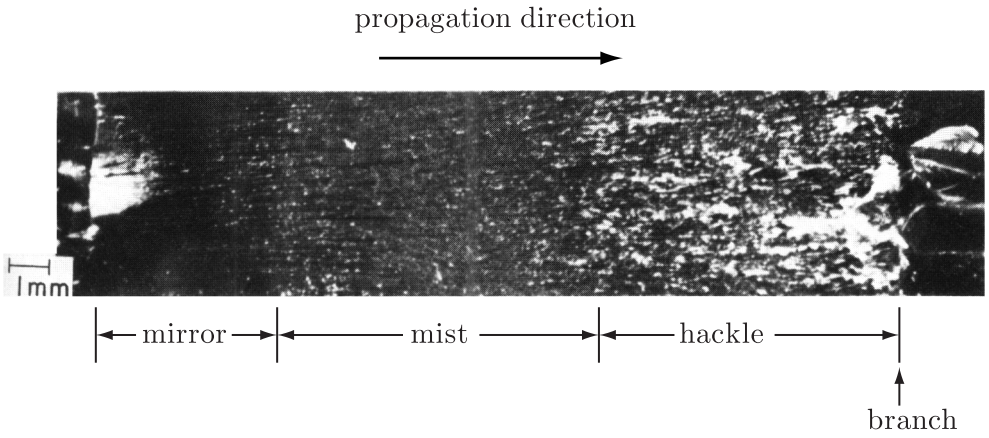

Figure 6.1: "Mirror-mist-hackle" appearance of a fracture surface in Homalite, observed by Ravi-Chandar and Knauss [1984].

and propagation speeds of cracks in brittle solids. Computational studies include those by Abraham *et al.* [3, 4, 5, 6, 7], who present atomistic simulations of crack growth in two and three dimensional solids. They observe oscillation and branching of the fracture plane, accompanied by the creation of dislocations. These calculations show similar speed characteristics to the aforementioned experiments, although the length scales of the oscillation and branching behavior are significantly smaller.

6.1.2 Theories of limiting speeds

Theoretical analysis of crack propagation has been centered on the prediction of limiting speeds, the maximum speed at which the crack grows. The earliest such analyses were done by Yoffe [107], who predicted that smooth crack propagation, the crack growing in the direction of its original orientation, can occur up to speeds of 60 % of c_R, beyond which the point of maximum hoop stress around the crack tip moves from a point directly ahead of the tip to a point 60° off axis. Later work was done by considering the balance of energy around the crack tip region. Freund's analysis [108] showed that the energy release rate goes to zero as the crack approaches c_R,

$$G(a, \dot{a}) = \left[1 - \frac{\dot{a}}{c_R}\right] G(a, 0) . \tag{6.1}$$

Presumably, the strain energy arriving at the tip from regions ahead is consumed by some combination of kinetic energy radiated from the moving tip or is being consumed in the stress field surrounding the moving crack tip. The energy required for continued propagation is constant, Γ, so the zero velocity crack driving force must overcome the effect of the crack

propagating at a finite speed,

$$G\left(a,0\right) \approx \frac{\Gamma}{\left[1-\frac{\dot{a}}{c_R}\right]}. \tag{6.2}$$

Thus, Freund's results predict that the terminal speed of the crack will approach c_R asymptotically with increasing driving force. Liu and Marder [109] also begin from an energy balance perspective, but arrive at the conclusion that as long as the driving force exceeds the fracture energy, the crack speed will continue to accelerate towards c_R:

$$\ddot{a} \sim \left[1-\frac{\Gamma(\dot{a})}{G\left(a,\dot{a}\right)}\right]\left[1-\left(\frac{\dot{a}}{c_R}\right)^2\right]. \tag{6.3}$$

The analyses of both Freund and Liu and Marder do not consider the possibility of off-axis crack propagation.

More recent work by Gao has been able to explain the limiting speeds observed in experiments and simulations being below c_R. In 1993, Gao [1] used a wavy crack model to predict a crack propagation speed of 50 % of c_R. Considering the relation (6.2) by Freund, it is a straightforward calculation to show that the energy dissipated by a moving crack tip is maximal at 50 % of c_R,

$$\dot{\Gamma}\left(a,\dot{a}\right) = \dot{a}G\left(a,\dot{a}\right) = \dot{a}\left[1-\frac{\dot{a}}{c_R}\right]G\left(a,0\right). \tag{6.4}$$

By taking a microscopically wavy path, a nominally straight crack propagating at half the Rayleigh wave speed has the ability to dissipate more energy through an increase in apparent fracture energy, as depicted in Figure 6.2. Higher propagation speeds are unfavorable,

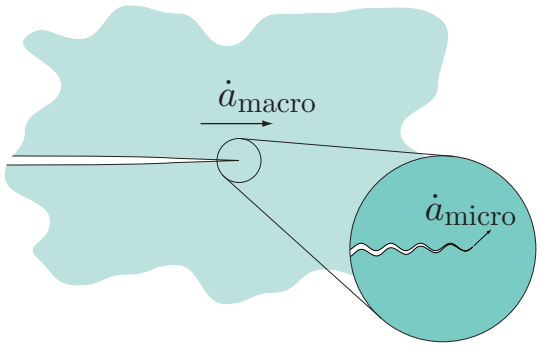

Figure 6.2: The wavy behavior of crack propagation required to maximize dissipated energy during the fracture process, as theorized by Gao [1].

as they reduce the energy release rate. This analysis focuses on the multiscale nature of the mechanisms governing the macroscopically observed fracture behavior. The wavy crack

model allows the local crack speed to increase, to allow more dissipation, while the macroscopic crack speed remains at approximately 1/2 of c_R to maximize the crack tip energy flux, $\dot{\Gamma}$. Although the crack trajectory changes with respect to the orientation of the macroscopic loading, this model is assumed to be independent of the mode of loading in the microscopic, near tip view. Later, Gao used the concept of local limiting speed to predict terminal crack speeds at approximately one third of c_R, assuming a cohesive strength of $E/30$ [110]. This estimation was based on the bottleneck state for the propagation of the bond breaking signal on a hyperelastic, cohesive medium. Gao's analysis shows that the characteristic wave speed of a solid depends on both its material tangent modulus and its current states of stress and deformation. At the cohesive limit, the tangent modulus approaches zero, and the material's wave speed depends solely on the cohesive strength of the underlying constitutive model. Unlike the previous analysis, the local limiting speed concept relies on the hyperelastic, nonlinear properties of the material in the vicinity of the crack tip. Additionally, the mechanism controlling the crack's limiting speed is less a function of the driving force and more a function of the rate limited processes surrounding the moving crack tip.

As we have already discussed, depending on the material system, the fracture processes may be numerous and complicated. Here, we consider only brittle fracture, which we define to mean that all dissipation during the fracture process is associated directly with the creation of new free surfaces. Accordingly, our continuum simulations employ a rate and history independent bulk constitutive model. The atomistic system used in this study is similar to the one considered by Abraham *et al.* [3] to study the behavior of crack growth under severe loading conditions. Although this system activates several mechanisms of dissipation during fracture given sufficient driving force, in this study, crack driving forces are maintained below a level at which these dissipation mechanisms are activated. Therefore, we expect to understand the fracture behavior in terms of the surface dissipation and the transport of strain energy by elastic waves or dispersion by phonons for the atomistic system.

6.2 Models and Methods

The problem we're considering is crack growth in a "long" strip. The strip needs to be long enough to allow the crack to reach steady state propagation conditions. The strip geometry used in this study is illustrated in Figure 6.3. If the strip is sufficiently long in the lateral

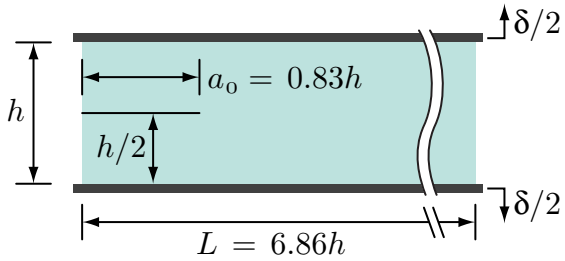

Figure 6.3: Geometry of the two-dimensional strip.

dimension, a J-integral analysis can be used to determine the static crack driving force under plane stress,

$$J_1 = \int_C \left(\mathcal{W} n_1 - \sigma_{ij} n_j \frac{\partial u_i}{\partial x_1} \right) ds \tag{6.5}$$

where the crack propagation direction is taken as x_1, $\mathcal{W}$ is the strain energy density of the material, and C denotes, in two dimensions, a line contour which surrounds the crack tip. This driving force can also be calculated by using the definition of the energy release rate as the derivative of the potential energy,

$$G = -\frac{\partial \mathcal{U}}{\partial a} = \frac{\mathcal{U}^{(1)} - \mathcal{U}^{(2)}}{\mathrm{w}}, \tag{6.6}$$

where (1) and (2) refer to thin strips of width w ahead of, and behind the crack tip, respectively, as shown in Figure 6.4. Using this relation, and assuming small strain isotropic

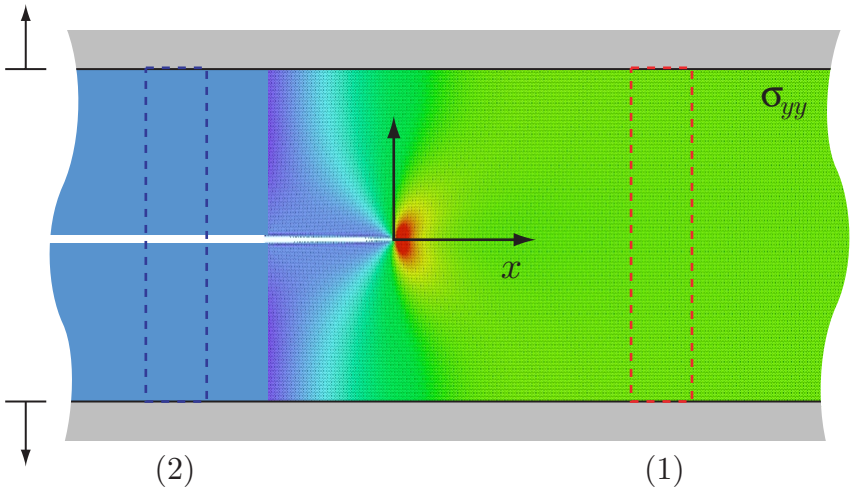

Figure 6.4: The steady-state crack. The crack driving force is estimated from the difference in potential energy between regions (1) and (2).

elasticity, the energy release rate is

$$G = \frac{E\, h\, \epsilon^2}{2\,(1-\nu^2)}, \tag{6.7}$$

where E is Young's modulus, ν is Poisson's ratio, and $\epsilon = \frac{\delta}{h}$ is the nominal applied strain. This quasistatic analysis only applies to the onset of crack growth. Accurate predictions of the response of either the continuum or atomistic system during dynamic propagation remains a challenge for analysis.

We simulated growth in the strip using atomistics and using the finite element method, with a layer of cohesive surface elements along the cleavage plane. The models used for

both the atomistic and continuum calculations have intentionally been kept as simple as possible. The atomistic calculations use a simple pair interaction, while the continuum calculations use a standard small strain finite element formulation to model the behavior of the bulk. Fracture is introduced by seeding the cleavage plane with a layer of cohesive elements. Unlike the atomistic calculations, this seeding predefines the fracture path for the continuum simulations.

Over a domain Ω with a boundary C, the variational form of the dynamic equation of equilibrium in the absence of body forces may be written as

$$\int_{\Omega} \rho \frac{\partial^2 \mathbf{u}}{\partial t^2} \cdot \delta \mathbf{u} \, d\Omega + \int_{\Omega} \boldsymbol{\sigma} : \delta \boldsymbol{\epsilon} \, d\Omega + \int_{C_{\text{int}}} \mathbf{T}(\boldsymbol{\Delta}) \cdot \delta \boldsymbol{\Delta} \, ds = \int_{C_h} \mathbf{T} \cdot \delta \mathbf{u} \, ds, \tag{6.8}$$

where ρ is the mass density, $\mathbf{u}$ is the displacement field, $\boldsymbol{\epsilon} = \frac{1}{2}\left(\nabla \mathbf{u} + (\nabla \mathbf{u})^{\mathrm{T}}\right)$ is the infinitesimal strain tensor, and the Cauchy stress $\boldsymbol{\sigma}$ and traction $\mathbf{T}$ are related through the normal $\mathbf{n}$ as $\mathbf{T} = \boldsymbol{\sigma}\mathbf{n}$. Contributions from surface tractions in (6.8) appear over regions of the boundary $C_h \subseteq C$ with externally applied tractions and over pairs of internal surfaces C_{int} due to the variation in the surface opening displacement $\delta\boldsymbol{\Delta}$. For this study, we use a model traction-separation relation similar to the one introduced by Tvergaard and Hutchinson [111]. The magnitude of the cohesive traction is expressed as a function of a nondimensional effective opening displacement

$$\Lambda = \sqrt{(\Delta_t/\delta_t)^2 + (\Delta_n/\delta_n)^2}, \tag{6.9}$$

where δ_t and δ_n represent the characteristic tangential and normal opening displacements, respectively. The total displacement vector $\boldsymbol{\Delta}$, is given as $\boldsymbol{\Delta} = \{\Delta_t, \Delta_n\}$. As illustrated in Figure 6.5, the tri-linear magnitude of the traction $\hat{T}(\Lambda)$ depends on a single shape factor

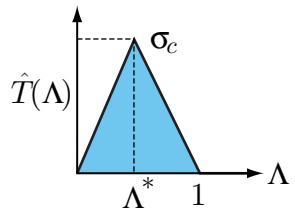

Figure 6.5: The traction-separation relation used for this work.

Λ^*. The traction response is assumed to be reversible up to $\Lambda = 1$, after which the surface is assumed to have failed. Defining a traction potential

$$\varphi(\boldsymbol{\Delta}) = \delta_n \int_0^{\Lambda} \hat{T}(\xi) \, d\xi \tag{6.10}$$

yields the rate-independent, mixed-mode traction-separation relation

$$\mathbf{T}(\boldsymbol{\Delta}) = \frac{\partial \varphi(\boldsymbol{\Delta})}{\partial \boldsymbol{\Delta}} = \delta_n \hat{T}(\Lambda) \frac{\partial \Lambda}{\partial \boldsymbol{\Delta}} \tag{6.11}$$

and a fracture energy

$$G_c = \frac{1}{2}\sigma_c \delta_n. \tag{6.12}$$

The cohesive surface relation (6.11) is not intended to represent the response of any specific material. Surrounded by an elastic medium, the detailed shape of the relationship is not expected to have a significant effect. The relationship simply introduces a well-defined fracture energy into the simulation procedure with a clear point of complete failure in a form that facilitates analytical study. The stress response of the bulk is defined by

$$\sigma_{ij} = \left[\mu\, \delta_{ij}\delta_{rs} + \lambda\, (\delta_{ir}\delta_{js} + \delta_{is}\delta_{jr})\right] \epsilon_{rs}, \tag{6.13}$$

where μ and λ are Lamé constants.

The approach for the atomistic simulations similarly makes use of a model system. The single crystal sample is constructed from a two-dimensional, hexagonal lattice bound by the Lennard-Jones 6-12 potential

$$U_{LJ}(r) = 4\,\varepsilon \left[-(\sigma/r)^6 + (\sigma/r)^{12}\right], \tag{6.14}$$

where σ sets the length scale of the potential and $-\varepsilon$ is the depth of the potential well. In order to allow us to control the range of influence of the potential without introducing abrupt behavior at a cut-off distance, we use the modified potential

$$U(r) = U_{LJ}(r) - U_{LJ}(r_c) - (r - r_c)\, U'_{LJ}(r_c), \tag{6.15}$$

where r_c is the distance at which the potential and its first derivative pass through zero. This cut-off distance is selected to include up to the fifth nearest neighbors in the undeformed configuration. The crystal is a triangular lattice with an interatomic spacing a_0. We choose $\frac{h}{a_0} = 212$ to distance the fracture process zone from the rigidly imposed boundary conditions. The characteristic dimension of the finite elements near the cleavage plane is $h_{\min} = a_0$.

6.3 Simulation Results

The parameters for the continuum and atomistic systems are selected to correspond with each as closely as the differing descriptions permit. Due to the centrosymmetry of the undeformed lattice, the initial elastic properties of the crystal display Cauchy symmetry, for which $\lambda = \mu$. The shear modulus μ is matched to the elastic properties calculated for the crystal, and the density ρ is selected to correspond with the atomic mass and volume of the undeformed lattice. The fracture properties of the systems cannot be compared so directly. The fracture energy ϕ is not solely dependent on ε, the energy of a single bond, and the effective opening displacement Λ (6.9) does not correspond to the bond length r.

6.3.1 Quasistatic fracture

The fracture parameters in the cohesive relation $\mathbf{T}(\boldsymbol{\Delta})$ (6.11) are selected in order to match the traction distribution on the cleavage plane of the strip model at the critical boundary displacement. The critical displacement is identified by applying Griffith's condition to the atomistic system. The boundaries are displaced until the uncleaved configuration of the strip is no longer energetically favored. Comparing the bond energy per undeformed volume "far" ahead of the pre-crack with the reference energy of the crystals yields the fracture energy G_c. G_c is estimated from the atomistic system by observing that fracture occurs during quasistatic loading exactly when the potential energy available ahead of the crack tip reaches the level of the surface energy needed to propagate the crack by creating new surfaces, as seen in Figure 6.6. In general, strain energy remaining within the material after

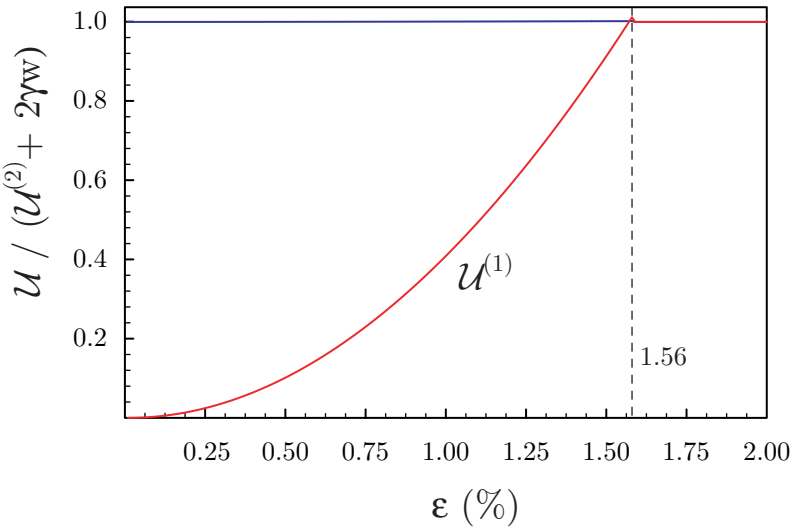

Figure 6.6: Bond potential energy in the atomistic system as a function of applied strain.

cracking $\left(\mathcal{U}^{(2)} \neq 0\right)$, as well as any energy associated with dissipation mechanisms, *e.g.* a plastic zone, will require that the potential energy $\mathcal{U}^{(1)}$ be greater than 2γw.

The traction distribution for the atomistic system is calculated from the force in all bonds crossing the cleavage plane, averaged over segments of length a_0 along the fracture surface. This calculation yields a peak traction, σ_c, of approximately $E/18$, where E is Young's modulus of the crystal. The cohesive surface parameters σ_c and $G_c = 2\gamma$ are chosen to match the atomistic results, producing $\sigma_c = 0.3635$ eV/Å^2 and $G_c = 0.708$ eV/Å. The values for δ_t, δ_n and Λ^* were chosen to equal 3.8955 Å, 3.8955 Å and 0.1839, respectively. These calculations are subject to plane stress, however the elastic modulus is matched to the atomistic system's properties. The traction distributions produced are illustrated in Figure 6.7. Quasistatic analysis of the strip configuration yields a failure strain $\epsilon_c = \frac{\delta}{h} \approx$ 1.5 %. The continuum simulation cleaves at a strain within 1 % error of the predicted

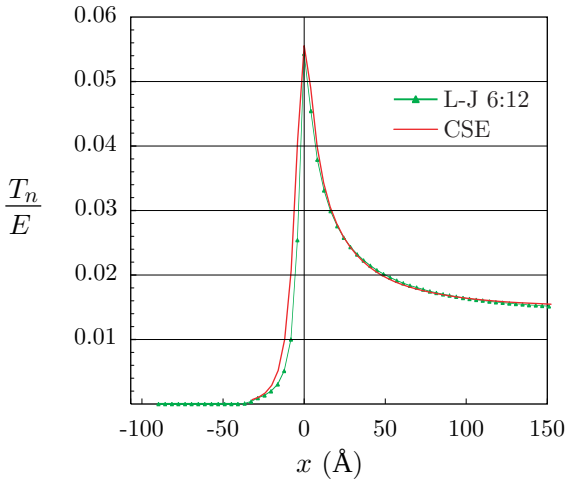

Figure 6.7: A comparison of the traction distribution on the cleavage plane.

value. Correcting the Griffith analysis to account for the compliance of the cohesive surface layer reveals that the continuum simulation reproduces the expected failure strain to within an error of nearly 0.1 %. These results indicate that the model has sufficient extent both ahead and behind the crack tip to match the steady-state cracking assumptions and that the tractions are well resolved over the elements in the fracture process zone.

The atomistic model cleaved at a strain of 1.56 %, approximately 4% higher than that predicted by the Griffith analysis, which we attribute to the nonlinear response of the interatomic potentials. Figure 6.7 illustrates that the region on the traction distribution behind the peak is a tail that decays over a distance of approximately $10\,a_0$, and the stresses ahead of the tip stay well above the far field values to a distance of nearly $25\,a_0$.

We wished to determine the influence of the cut-off radius r_c on the atomistic model with regard to both quasistatic and dynamic crack propagation. As such, we compared the model already introduced which includes out to fifth nearest neighbor interactions, for which $r_c \approx 4.01\ a_0$, with a shorter-range interaction that goes out only to second nearest neighbors, $r_c \approx 2.36\ a_0$. We adjusted the parameters of the potential in order to preserve the values of Young's modulus and fracture energy

$$\frac{E^{5th}}{E^{2nd}} = \frac{G_c^{5th}}{G_c^{2nd}} = 1. \tag{6.16}$$

The change in r_c alters the value of the lattice parameter,

$$\frac{a_0^{5th}}{a_0^{2nd}} = 0.81, \tag{6.17}$$

although the system geometry is scaled with lattice parameter to make our analyses self-similar. In changing from a fifth to a second neighbor interaction range, the fracture process zone, which we associate with the "tail" following to the left of the peak, shrinks by about

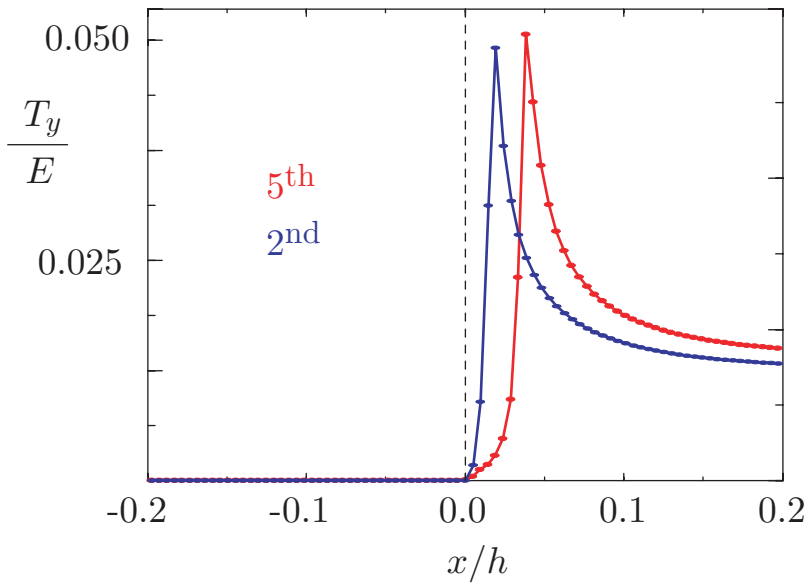

Figure 6.8: Traction distribution along the crack plane for the atomistic models. Fifth and second nearest neighbor interaction ranges are colored in red and blue, respectively.

a factor of two, as seen in Figure 6.8. Gao's analysis of the cohesive state wave speed [110] includes an estimate of the effect of dispersion on the speed at which the bond-breaking signal can propagate ahead of the moving tip. The rate at which energy propagation occurs is known as the group velocity v_g. Since v_g is a function of wavelength in a dispersive medium, we wanted to alter the length scale of the shape of the bond-breaking zone with the intention of altering the wavelength of the so-called "bond-breaking wave". From this alteration, the Cauchy-Born elasticity expression for the equibiaxial cohesive stress increases by a factor of about 3 % when a second neighbor interaction range is used. This is not in agreement with the atomistic calculations shown in Figure 6.8, which show σ_c^{5th} slightly greater than σ_c^{2nd}. However, the atomistic simulation used to generate Figure 6.8 does posses a level of computational uncertainty, caused by the sharp peak or the rapidly varying traction, which could explain this discrepancy. The larger lattice spacing leads to a lower density and a higher value of c_R. This modification to c_R more than compensates for the reduced cohesive stress, predicting the limiting speed for the fifth neighbor case to be slightly faster than for the second neighbor case, which is not in agreement with the cohesive state wavespeed analysis.

6.3.2 Dynamic crack propagation

Next, we examine the dynamic response of the continuum system subject to a fixed crack driving force. This fixed driving force was achieved by first loading the system quasistatically, then applying a final short, but smooth, displacement of the boundaries to achieve the final

level of driving force. The continuum calculations, like the atomistic ones, are done with explicit dynamics. In Figure 6.9, we compare the calculated variation of the terminal speed

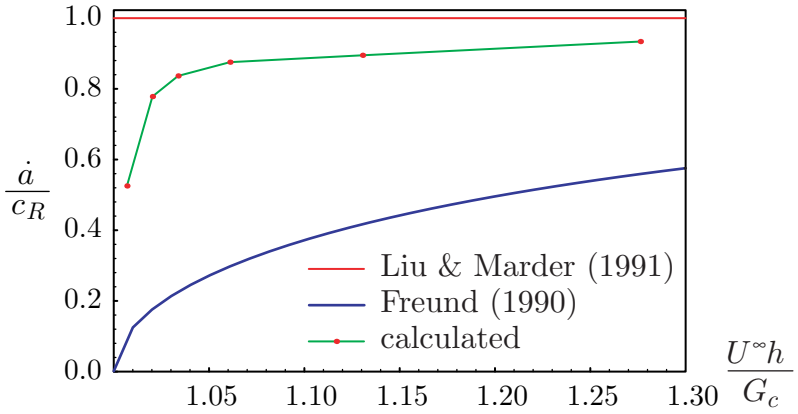

Figure 6.9: Terminal, or limiting speed of a dynamic crack as a function of overload, the ratio of energy remotely applied to the system to the fracture energy required for quasistatic crack growth.

with driving force with Freund's and Liu and Marder's predictions. Our calculations show the terminal speed does vary with driving force, as predicted by Freund; however, the asymptotic approach to an upper limit occurs more quickly with increasing driving force than predicted by Freund. We would expect some differences here because Freund's calculations do not accurately account for the finite height of the strip. The asymptotic terminal speed also appears to be somewhat lower than c_R, an effect that may also be a result of finite strip size. Figure 6.10 looks at the history of the crack speed with crack length. We observe

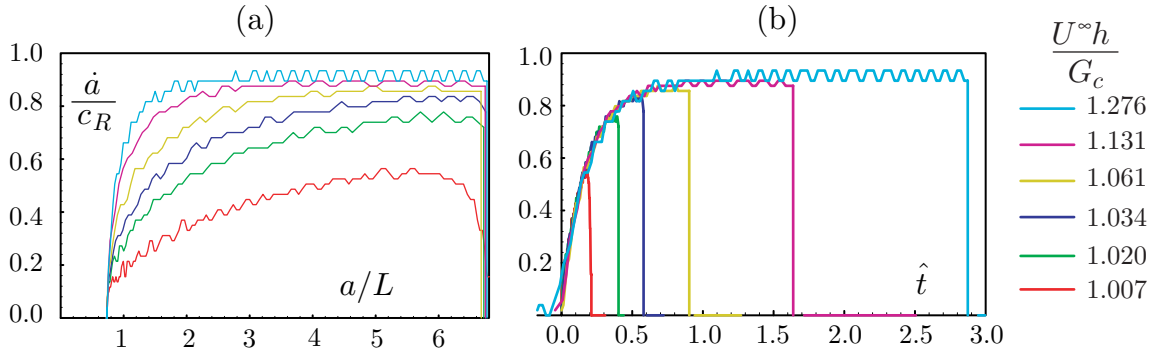

Figure 6.10: Crack speed history as functions of (a) normalized crack length and (b) Liu and Marder's time scaling factor.

that not only does the terminal speed vary with driving force, but the time to reach this terminal speed also depends on the driving force. Figure 6.10(b) shows that although Liu

and Marder's solution does not seem to capture the variation in terminal speed with driving force, their time scaling factor of $\hat{t}$,

$$\hat{t} = t \, \frac{c_d}{h} \left[1 - \frac{G_c h}{U^\infty} \right], \tag{6.18}$$

does seem to describe the transient portion of the crack history very well. With this scaling applied, all the curves for the different driving forces overlap, though each curve reaches a different terminal value. It is important to note that in Liu and Marder's solution, all cracks will eventually propagate at c_R, but those with lower driving force will take longer to reach this speed.

We compared fracture behavior of the atomistic and continuum systems subject to constant velocity displacement of the upper and lower surfaces. The stress component σ_{yy} for the continuum system, shown in Figure 6.11, shows the expected behavior: the crack is restricted to propagate along the cleavage plane and the stress field appears as if the tip field

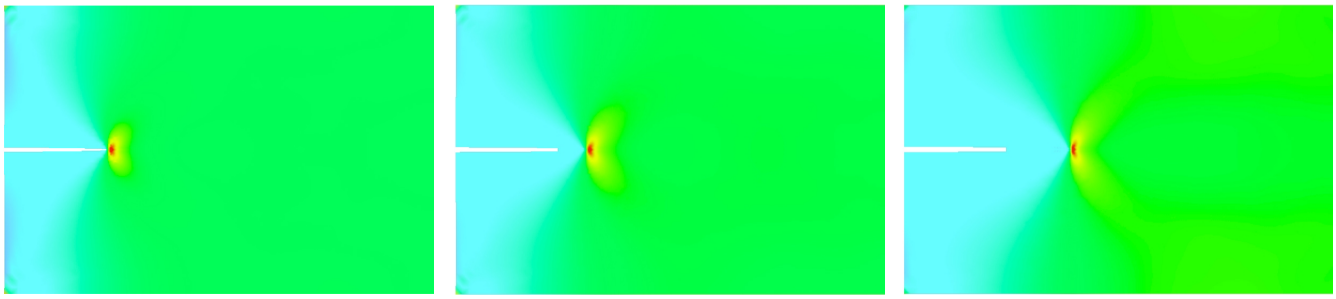

Figure 6.11: Frozen time frames of the propagating continuum crack stress component σ_{yy}.

is translating through the body as the crack grows. The constitutive models used for this simulation are rate independent, thus, so are the results. Figure 6.12 shows the results for the atomistic simulations at two different displacement rates. At the slower rate, the crack propagates without any kinking in the fracture path and without emitting any dislocations. At the higher rate, the fracture path does vary from straight-ahead propagation every time a dislocation is emitted. We concentrate the remainder of our analysis to the former case, since the behavior is potentially more straightforward to explain. One feature that is immediately obvious in Figure 6.12 is the fine scale wavelength content in the atomic stress field. This fine scale behavior is entirely missing from the continuum calculations. We will investigate this further with the next series of calculations. Notice that elastic waves do not appear in Figure 6.11, due to the scale of the stress contours.

In order to compare the continuum and atomistic models of smooth crack propagation, the systems were loaded from a strain near to their critical strains with a constant velocity of $c_d/\dot{\delta} = 7500$, where c_d is the dilatational wave speed in the material. The variation of the crack velocity as a function of crack length is shown in Figure 6.13(a). The velocity

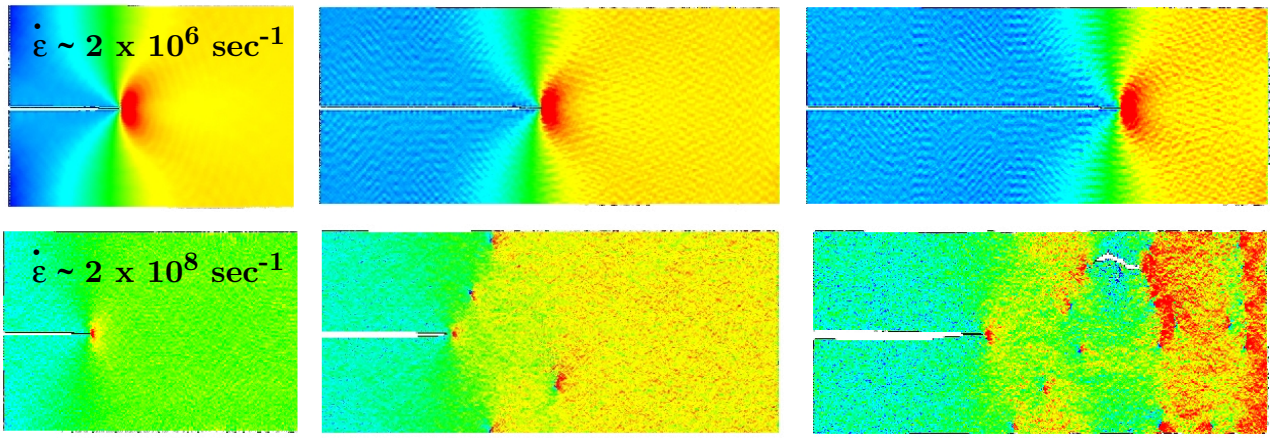

Figure 6.12: Frozen time frames of the propagating atomistic crack stress component σ_{yy}. Two different loading rates are shown.

is normalized by the Rayleigh wave speed c_R, the limit speed for cracks propagating under mode I loading. While the crack speed in the continuum simulation steadily climbs towards the limiting speed with increasing driving force, the crack speed in the atomistic simulation does not exceed approximately 20% of c_R. In contrast to expectations from the cohesive state wave speed, the crack limiting speed in the second neighbor interaction model, 23 % of c_R, slightly exceeds the speed in the fifth neighbor interaction model, 21 % of c_R, giving a ratio of

$$\frac{(\dot{a}/c_R)^{5th}}{(\dot{a}/c_R)^{2nd}} \approx 0.91, \tag{6.19}$$

rather than the ratio estimated from Gao's local limiting speed theory,

$$\frac{(\dot{a}/c_R)^{5th}}{(\dot{a}/c_R)^{2nd}} = 1.02. \tag{6.20}$$

Figure 6.13(b) reveals the markedly different energetics associated with crack growth for each system. The figure shows the rate of kinetic energy generation with crack extension $\frac{\Delta \mathcal{T}}{\Delta a}$ as a function of crack length. The continuum simulation shows that approximately 3% of the strain energy required for quasistatic crack growth is converted to kinetic energy for $1 < \frac{a}{h} < 4$, corresponding to $0.2 < \frac{\dot{a}}{c_R} < 0.7$. For $\frac{a}{h} > 4$, acceleration of the crack slows and the rate of kinetic energy generation decreases although the driving force continues to increase. The smoothed results from the atomistic simulation, the dark, solid line in Figure 6.13(b), reveal a rate of kinetic energy generation that initially increases linearly. This rate of generation levels off as the crack tip approaches the strip's far boundary. The results suggest that the terminal crack speed for the continuum simulation is determined largely by limits in the driving strain energy release rate, while the terminal crack speed in the atomistic system is controlled by an intrinsic limit on the rate of bond breaking at the

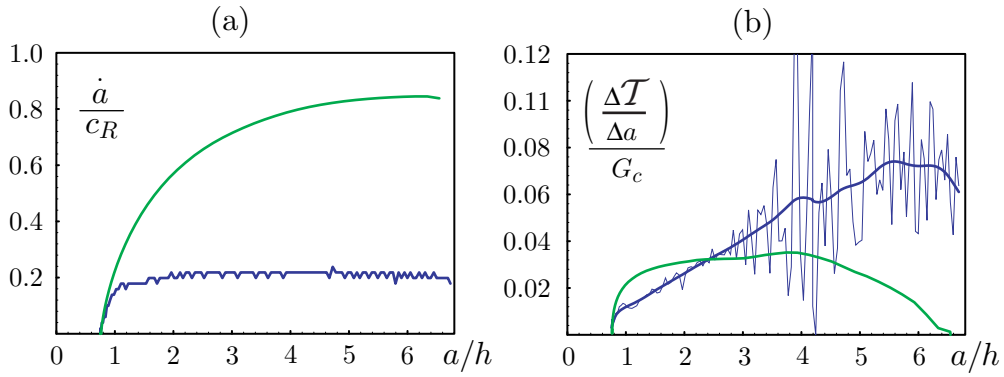

Figure 6.13: Comparison of the continuum simulations with a cohesive surface interface (colored green) with atomistic simulations (colored blue). (a) normalized crack speed *vs.* crack length (b) kinetic energy generation rate.

crack tip. Excess energy is converted to kinetic energy rather than increasing the speed of fracture.

We can get another view of the differing behavior in each system's tendency to transform stored energy to kinetic energy by choosing a vertical strip of observation and monitoring the kinetic energy in this strip as the moving crack passes. The graph of this kinetic energy variation is shown in Figure 6.14(a) for the continuum calculation and in Figure 6.14(b)

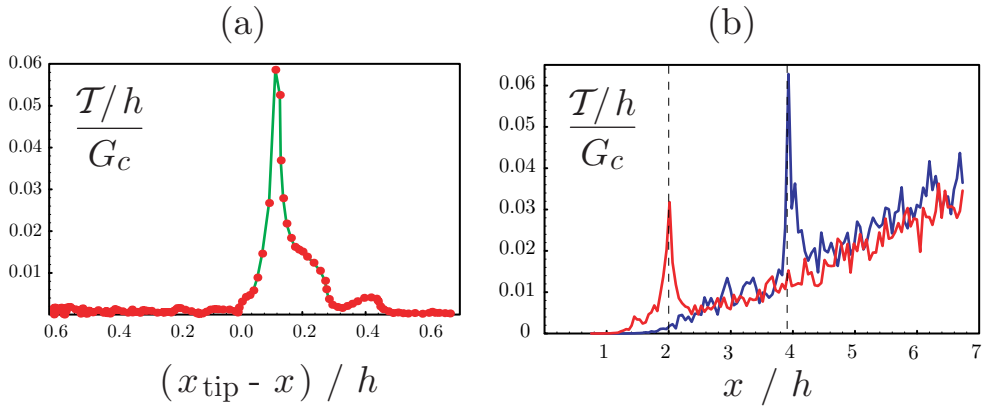

Figure 6.14: Kinetic energy history for (a) a strip of material ahead of the initial crack tip for the continuum simulation and (b) two strips of material ahead of the initial crack tip for the atomistic simulation.

for the atomistic calculation. The continuum simulation shows very little kinetic energy in the strip of observation before the crack arrives. As the crack passes, the kinetic energy jumps, but returns to the same quiescent state after the crack tip has passed. The lack of kinetic energy in the wake of the crack seems to indicate that the energy generated is

tied to the moving crack tip and is not radiated as the crack propagates. However, there must be some residual kinetic energy behind the crack tip. In Figure 6.9, it is observed that the crack speed as a function of overload does not approach c_R, but rather, some lower value. This implies that the energy must be shed by some other means, even though kinetic energy is not apparent in Figure 6.14. Two points of observation are shown for the atomistic simulation. Like its continuum counterpart, the kinetic energy peaks and then drops quickly as the moving tip passes. However, the atomistics do show an increase in a "background" kinetic energy with seemingly random character that we associate with thermal vibrations.

6.3.3 Discussion and analysis

Modeling dispersion as viscous dissipation

We have observed that some significant amount of strain energy reaching the moving crack tip is transformed into random vibrations of the lattice that we might interpret as heat. From a continuum point of view, we may ask if this lost energy can be modeled as viscous dissipation. Viscous dissipation could be added to the bulk material, the cohesive zone relation, or both. We chose to restrict the viscous dissipation to the cohesive zone in order to make it easier to control and monitor. From a physical point of view, we justify this modeling assumption by imagining that the random thermal vibrations are generated in or near the fracture process zone and then propagate out into the crystal. For the continuum simulation, this energy is simply removed from the cohesive zone rather than being allowed to propagate away. The viscous traction in the cohesive zone, $\boldsymbol{T}^{visc}$, is related to the opening displacement rate by a viscosity parameter that decreases linearly from an initial value to zero as the nondimensional opening parameter varies from 0 to 1,

$$\boldsymbol{T}^{visc} = \eta\left(\lambda\right)\dot{\boldsymbol{\Delta}} = \eta_0\left(1-\lambda\right)\dot{\boldsymbol{\Delta}}. \tag{6.21}$$

The energy removed by this viscous dissipation can be quantified by

$$\Gamma_{visc} = \int_0^{\delta_n} \boldsymbol{T}^{visc} \cdot d\boldsymbol{\Delta}. \tag{6.22}$$

These relations can be combined with the Tvergaard-Hutchinson cohesive zone relation. The assumption of a constant opening rate yields

$$\Gamma_{visc} = \frac{1}{2}\,\eta_0\,\delta_n\,\dot{\Delta} = \frac{1}{2}\,\eta_0\,\delta_n^2\,\frac{\dot{a}}{\ell_{zone}}. \tag{6.23}$$

The parameters of this model were selected such that a viscous dissipation rate of 5 % of the rate independent, quasistatic fracture energy would occur for a crack moving at 20 % c_R. Using a cohesive zone length, ℓ_{zone}, equal to $5a_0 = 20.4$ Å, equation (6.23) yields a value of 0.01166 for η_0. The crack propagation history and viscous dissipation rate are shown in Figure 6.15. We see that the crack does accelerate more slowly, but still appears to be approaching a much higher terminal speed than seen in the atomistic simulations. The crack

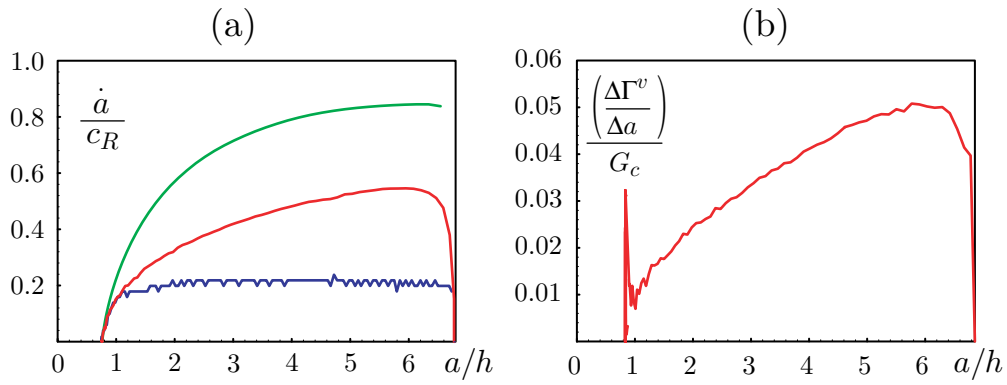

Figure 6.15: (a) Crack speed history for the continuum simulation that includes viscous dissipation. The damped calculation is shown in red, with the original cohesive zone and atomistic simulations shown in their original colors (green and blue, respectively) for comparison. (b) Viscous dissipation rate for the damped simulation.

accelerates so slowly that the strip is not long enough for it to reach its terminal speed. The plot of viscous dissipation rate shows that the rate increases with crack speed and length; however, the additional dissipation does not allow the continuum simulations to reproduce the behavior of the atomistic system. Instead, the additional dissipation appears to have the effect of slowing the approach to the terminal speed in a manner suggested by the time scaling proposed by Marder and Liu.

Spectral analysis of the moving crack tip

Because wave propagation in the lattice is dispersive, we focus in on the characteristic wavelengths in the motions of the atoms around the moving crack tip. In order to remove the gross displacement of the lattice from the spectral analysis, we first apply a low-pass filter to the motions of the atoms and remove this content from the displacements,

$$\psi_y(x,a) = u_y(x) - \int \phi_a(x-y)\, u_y(y)\, dy. \tag{6.24}$$

We then look at the Fourier spectrum ($\Im(\psi_y)$) of the y-direction displacements of the atoms in a region behind and a region ahead of the moving crack tip. These spectra are shown in Figure 6.16. Ahead of the crack, we see a fairly broad spectrum of vibrations. Behind the moving tip, we see a clear concentration of the displacements at a wavelength approximately five times the lattice parameters. Surprisingly, nearly the same wavelength appears for both the second and fifth neighbor cases, showing an insensitivity to the fracture process zone size. The appearance of this strong peak is relatively insensitive to the location of the sampling window behind the crack tip, indicating the spatial extent and stability of this crack surface feature. The origins of this 5 a_0 wave as well as its relation to the terminal speed of the crack are still unclear.

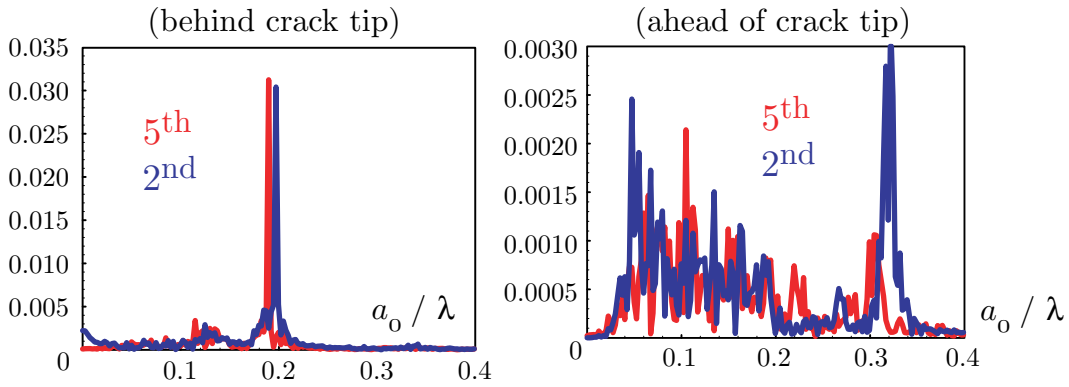

Figure 6.16: Fourier spectra of the crack-plane displacements behind, and ahead of, the crack tip.

We did investigate whether any characteristic wavelengths are predicted by simple analogs to the moving crack in solutions for linear elastic media. Although the near tip region is highly deformed, most of the strip away from the tip is in a relatively mild state of deformation. Additionally, we had seen some period features in the stress field trailing a moving tip in other continuum simulations. As shown in the Figure 6.17, the σ_{yy} component of the stress field trailing the moving crack tip shows periodic fluctuations [112]. In this

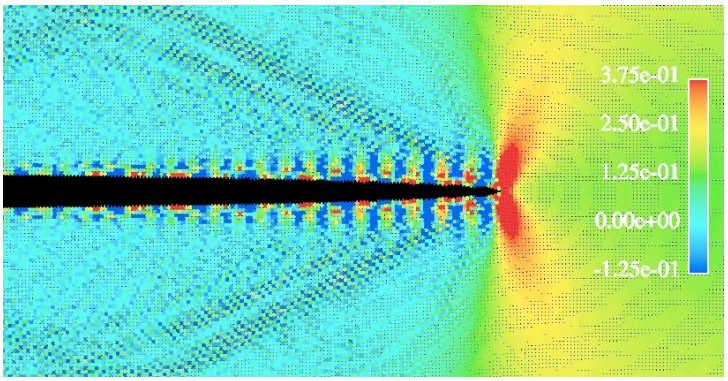

Figure 6.17: σ_{yy} stress field for a cohesive zone simulation at a high loading rate.

case, the crack is driven significantly harder than in the simulations done for this study. These calculations showed that these oscillations in the stress field developed only after the crack had achieved its limiting speed while subject to large driving forces. We have not verified that the oscillations in the stress field shown in the figure are indeed related to the y-displacement oscillations displayed by the moving crack in the atomistic calculations. Notably, the oscillations appear at different crack tip speeds, though limiting speeds in both cases.

Propagation of energy through a lattice

Following Gao, our assumption about the terminal speeds seen in the atomistic calculations is that it is governed by the rate of propagation of the bond breaking signal. We have mentioned that propagation of waves through a lattice is dispersive. This behavior can be quantified by calculating the dispersion curves. This is done by linearizing the equations of motion,

$$m^{\alpha}\delta\ddot{\mathbf{u}}^{\alpha} = \sum_{\beta\neq\alpha}^{N} \frac{\partial \mathbf{F}^{\alpha}}{\partial \mathbf{u}^{\beta}}\delta\mathbf{u}^{\beta}, \tag{6.25}$$

where

$$\mathbf{F}^{\alpha} = -\frac{\partial \mathcal{U}}{\partial \mathbf{u}^{\alpha}}. \tag{6.26}$$

We then use the Brillouin solution for a moving plane wave,

$$\delta\mathbf{u}\left(\mathbf{X},t\right) = \mathbf{A}\exp i\left(\mathbf{k}\cdot\mathbf{X}-\omega t\right), \tag{6.27}$$

and substitute into (6.25) to obtain an expression for $\omega^{\alpha}\left(\mathbf{k}\right)$ where ω is defined as the circular frequency and $\mathbf{k}$ is the wave vector. The group velocity v_g is defined as

$$v_g^{\alpha} = \left|\frac{\partial \omega^{\alpha}}{\partial \mathbf{k}}\right|. \tag{6.28}$$

For the triangular lattice, we find the second and fifth neighbor potentials display identical dispersion relations in the undeformed configuration, as shown in Figure 6.18. For this

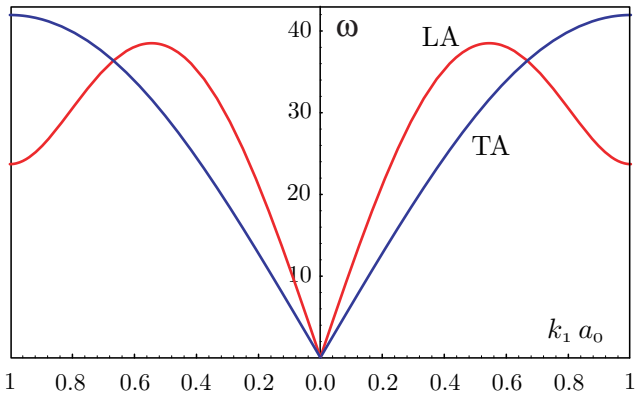

Figure 6.18: Longitudinal Acoustic (LA) and Transverse Acoustic (TA) dispersion curves for plane wave propagation for a 2-dimensional, triangular lattice. Here, k_2 is fixed at a value of $4\pi/\left(\sqrt{3}a_0\right)$.

2-dimensional case, the curves show the dispersion relations for the longitudinal (LA) and

transverse (TA) acoustic modes. As mentioned earlier, the speed at which energy propagates through the lattice is v_g. As the wave vector approaches zero, the group velocities for the longitudinal and transverse normal modes should approach the macroscopic dilatational and shear wave speeds, respectively. This analysis can be done using either the undeformed lattice, as in (6.27), or using the deformed lattice by substituting $\mathbf{x}$ for $\mathbf{X}$.

In order to explain the low limiting speeds observed in the atomistic simulations, and looking for any insight into the strong peak of the Fourier spectrum behind the crack tip, we are now left with a search for the rate limiting process. Considering the propagation of phonons through a lattice we can expect three effects: ballistic propagation, the effects of elastic scattering and the effects of inelastic scattering. Ballistic propagation is the propagation of phonons without any alteration in their frequency or wave vector. Elastic scattering describes a change in the phonon wave vector without altering its frequency, while inelastic scattering results from coupling between the normal modes that leads to changes in both the frequency and wave vectors of phonons. Figure 6.19 shows two sets of curves describing

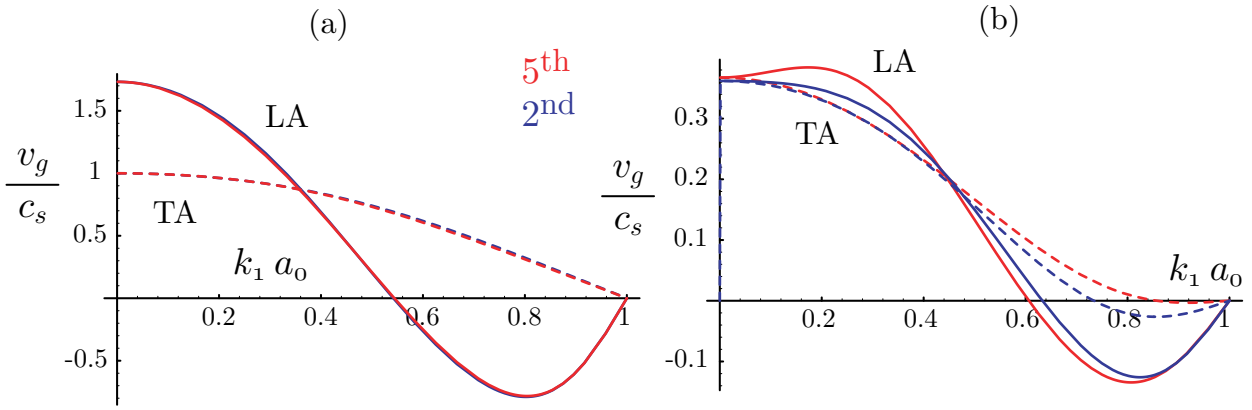

Figure 6.19: Group velocity as a function of the dimensionless wave vector $k_1 a_0$ for (a) the undeformed lattice and (b) the lattice at the equibiaxial cohesion limit.

the wavelength-dependent group velocities for the second and fifth neighbor lattices. In the undeformed configuration, Figure 6.19(a), the group velocities are the same. At the equibiaxial cohesive limit, Figure 6.19(b), the curves do show some differences. The speeds of the LA and TA modes are more similar at the cohesive point than in the undeformed configuration. The differences are bigger for the fifth neighbor case than for the second. Even at the cohesive state, the group velocity curves indicate speeds from zero to almost 40 % of the shear wave speed. There also does not seem to be anything especially outstanding about either the speed associated with a $k_1 a_0 = 1/5$, or the wavelength associated with $v_g = 0.2 c_R$.

As mentioned, elastic scattering alters the wave vector of phonons without affecting the frequency. A diffuse distribution of mass defects can produce this type of scattering. For this case, the rate of scattering has a strong ω^4 frequency dependence. Elastic scattering converts a coherent set of wave vectors into a more random distribution. As a result, scattering

leads to diffusive transport of phonon energy where the diffusion constant can be related to the scattering rate and the group velocity, usually ignoring dispersion. In the steady state cracking simulations, the system contains no mass or other defects, aside from the newly created free surfaces. Strain centers, like dislocation cores, are known to produce both elastic and inelastic scattering. For the most part, this effect has only been analyzed by treating the dislocations statistically and only within the context of trying to calculate the effect on a material's thermal conductivity. We have not seen any analysis of the elastic scattering of phonons around the highly deformed region around a crack tip.

Spontaneous phonon decay by inelastic scattering is due to the coupling in the vibrational modes of the crystal resulting from anharmonicity in the interatomic potentials. The large gradient in bond stretches surrounding a crack tip suggests inelastic scattering may be important. We could not find any references discussing inelastic scattering from inhomogeneous strain fields. On a related topic, we do not know what happens when phonons propagate through a medium with varying dispersive properties. As already shown, the dispersion behavior of the lattice changes dramatically from the lattice in its undeformed state to the lattice stretched to the equibiaxial cohesive limit. Phonons moving from the near tip region may experience both elastic and inelastic transformations. Even in the absence of large strains or highly inhomogeneous deformations, phonons decay anharmonically.

This process has a strong ω^5 frequency dependence, becoming more likely for higher energy phonons. For simple 3-phonon reactions, the rate of spontaneous decay is a function of the phonon wave vectors and the 3rd order elastic moduli [113]. Calculation of the scattering rate involves considering all sets of 3 phonons whose frequencies and wave vectors satisfy restrictions on the conservation of energy and momentum. These restrictions have a clear graphical representation on the dispersion curve, as is illustrated for the decay of a LA phonon into a pair of TA phonons, shown in Figure 6.20.

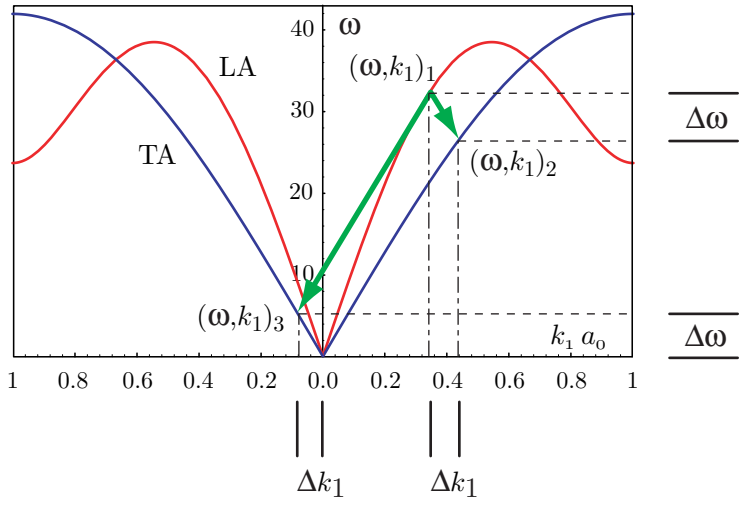

Figure 6.20: The decay of a LA phonon into a pair of TA phonons for the undeformed triangular lattice.

We have not calculated the scattering rate in our Lennard-Jones crystal; however, results for Si are available in the literature [114]. We find that the lifetime of very high energy phonons is on the order of the bond breaking rate, if we assume the crack is propagating at 20 % of the Rayleigh wave speed. This suggests that if very high energy phonons are generated by the bond breaking process, we would need to account for their decay when trying to predict the rate at which this bond breaking information is propagated to regions ahead of the crack tip. To verify this anharmonic process acts in the vicinity of the crack tip for our case, we need to calculate the scattering rate given the dispersion relations we already have. Additionally, we need to develop a method for directly identifying the phonons generated in the bond breaking zone, observing how they evolve as they propagate.

In summary, we have compared the response of a continuum and atomistic system under conditions of quasistatic and dynamic fracture. Under quasistatic conditions, the cohesive surface approach reproduces the predicted response of the strip model. This result is expected since the traction potential, with a simple change of variables, is equivalent to the J-integral evaluated on a contour over crack surfaces surrounding the tip. Under dynamic conditions, simply adopting a cohesive approach cannot reproduce crack dynamics of an atomistic system even when restricted to purely brittle propagation. At this point, we still know relatively little about what limits the speed at which the crack can propagate in our atomistic system or how the bond energy is transformed into kinetic energy or heat. However, understanding this limit could provide insight into the origins of crack tip instability and, ultimately, crack branching.

This page intentionally left blank.

Chapter 7

Conclusion

We have conducted a coordinated project in which experimental investigation of prototypical fracture events was used in conjunction with atomistic and continuum simulation techniques. Our goals were to merge ideas of atomistic and continuum analyses, to determine the areas in which continuum models need to be enriched to reflect atomic-scale processes, and to validate these methods by comparison with nano-scale experiments.

We have investigated the relationship between atomic-level processes and the longer-range behavior of the stress field through the analysis of nanoindentation near steps on a metal surface. The stress concentration at the step is by its nature an atomic-level property while the behavior of the stress field away from the step is better characterized by a continuum approach. We discovered that contact between the step edge and the indenter is sufficient to explain any seemingly "long-range" effect of the load needed to initiate yield. Efforts were then made to study nanoindentation of brittle materials, specifically sodium silicate glass and MgO. The experimental nanoindentation of the glass proved to be too complex for the current state of our modeling methods. Although experiments and atomistic simulation of nanoindentation of MgO has been performed, both need to be enhanced before meaningful information about crack nucleation and growth processes can be obtained. Finally, we have also analyzed and compared the static and dynamic responses of atomistic and continuum models of steady-state, 2-dimensional crack propagation. Specific characteristics have been quantified for both systems such as the limiting propagation speed and the generation rate of kinetic energy. Additionally, the atomistic system displays a concentration of kinetic motion into specific wavelengths. All of this analysis will help elucidate the origins of crack tip instabilities. This model problem allowed us identify specific directions in which continuum simulation needs to be enhanced by using a non-local description of material behavior.

Publications

The following publications have been produced as a result of the work for this project, and have either been published or are awaiting publication:

"Defect-dependent elasticity: Nanoindentation as a probe of stress state", K.F. Jarausch, J.D. Kiely, J.E. Houston and P.E. Russell, *J. Mater. Res.*, Vol. 15, No. 8, p. 1693 (2000).

"Surface Step Effects on Nanoindentation", J.A. Zimmerman, C.L. Kelchner, P.A. Klein, J.C. Hamilton and S.M. Foiles, *Phys. Rev. Lett.*, Vol. 87, No. 16, p. 165507 (2001).

"In-Situ STM Studies of Strain Stabilized Thin Film Dislocation Networks Under Applied Stress", O. Schaff, A.K. Schmid, N.C. Bartelt, J. de la Figuera and R.Q. Hwang, *Mater. Sci. Engin. A*, in press (2001).

"Dislocation Emission around Nanoindentations on a (001) fcc Metal Surface Studied by STM and Atomistic Simulations", O. Rodríguez de la Fuente, J.A. Zimmerman, M.A. González, J. de la Figuera, J.C. Hamilton, W.W. Pai and J.M. Rojo, *Phys. Rev. Lett.*, in review (2001).

"Lattice dispersion explanation for limiting speeds in steady-state crack propagation", P.A. Klein, J.A. Zimmerman and E.P. Chen, in preparation (2001).

"Effect of Surface Steps on Dislocation Structure During Nanoindentation", J.A. Zimmerman, P.A. Klein and S.M. Foiles, **Mater. Res. Soc. Symp. Proc.**, Vol. 649 (Fall 2000 MRS meeting).

"Development of cohesive models from the study of atomic scale fracture processes", P.A. Klein, J.A. Zimmerman and E.P. Chen, **10th International Conference on Fracture**, December 2-6, 2001.

Bibliography

[1] H. Gao. Surface roughening and branching instabilities in dynamic fracture. *Journal of the Mechanics and Physics of Solids*, 41:457–486, 1993.

[2] J. de la Figuera, M.A. González, R. García-Martínez, J.M. Rojo, O.S. Hernán, A.L. Vázquez de Parga, and R. Miranda. Stm characterization of extended dislocation configurations in au(001). *Phys. Rev. B*, 58:1169, 1998.

[3] F.F. Abraham, D. Brodbeck, R.A. Rafey, and W.E. Rudge. Instability dynamics of fracture : a computer simulation investigation. *Phys. Rev. Lett.*, 73:272–275, 1994.

[4] F.F. Abraham, D. Schneider, B. Land, D. Lifka, J. Skovira, J. Gerner, and M. Rosenkrantz. Instability dynamics in three-dimensional fracture : an atomistic simulation. *J. of the Mech. Phys. Solids*, 45:1461–1471, 1997.

[5] F.F. Abraham. On the transition from brittle to plastic failure in breaking a nanocrystal under tension (NUT). *Europhysics Letters*, 38:103–106, 1997.

[6] F.F. Abraham and H. Gao. Anomalous ductile-brittle fracture behavior in fcc crystals. *Philosophical Magazine Letters*, 78:307–312, 1998.

[7] F.F. Abraham, D. Brodbeck, W.E. Rudge, J.Q. Broughton, D. Schneider, B. Land, D. Lifka, J. Gerner, M. Rosenkrantz, J. Skovira, and H. Gao. *Ab initio* dynamics of rapid fracture. *Modelling and Simulation in Materials Science and Engineering*, 6:639–670, 1998.

[8] C.W. Gear. *Numerical Initial Value Problems in Ordinary Differential Equations*. Prentice-Hall, Englewood Cliffs, New Jersey, 1971.

[9] J.M. Haile. *Molecular Dynamics Simulation Elementary Methods*. John Wiley & Sons, Inc., New York, 1992.

[10] G.N. Vanderplaats. *Numerical Optimization Techniques for Engineering Design*. McGraw-Hill, Inc., New York, 1984.

[11] W.H. Press. *Numerical Recipes: the art of scientific computing*. Cambridge University Press, New York, 1989.

[12] J.R. Shewchuk. An introduction to the conjugate gradient method without the agonizing pain, 1994.

[13] H.C. Andersen. Molecular dynamics simulations at constant pressure and/or temperature. *J. Chem. Phys.*, 72:2384–93, 1980.

[14] W.G. Hoover. Canonical dynamics: Equilibrium phase-space distributions. *Phys. Rev. A*, 31:1695–7, 1985.

[15] S. Nosé and M.L. Klein. Constant pressure molecular dynamics for molecular systems. *Molecular Physics*, 50:1055–76, 1983.

[16] S. Nose. A unified formation of the constant temperature molecular dynamics methods. *J. Chem. Phys.*, 81:511–9, 1984.

[17] M.P. Allen and D.J. Tildesley. *Computer Simulation of Liquids*. Clarendon Press, Oxford, 1987.

[18] J.E. Lennard-Jones. The determination of molecular fields I. From the variatio nof the viscosity of a gas with temperature. *Proc. Roy. Soc. (London)*, 106A:441, 1924.

[19] J.E. Lennard-Jones. The determination of molecular fields II. From the equation of state of a gas. *Proc. Roy. Soc. (London)*, 106A:463, 1924.

[20] F.H. Stillinger and T.A. Weber. Computer simulation of local order in condensed phases of silicon. *Phys. Rev. B*, 31:5262–5270, 1985.

[21] M.S. Daw and M.I. Baskes. Semiempirical, quantum mechanical calculation of hydrogen embrittlement in metals. *Phys. Rev. Lett.*, 50:1285–8, 1983.

[22] M.S. Daw and M.I. Baskes. Embedded-atom method: Derivation and application to impurities, surfaces and other defects in metals. *Phys. Rev B*, 29:6443–53, 1984.

[23] S.M. Foiles, M.I. Baskes, and M.S. Daw. Embedded-atom-method functions for the FCC metals Cu, Ag, Au, Ni, Pd, Pt, and their alloys. *Phys. Rev. B*, 33:7983–7991, 1986.

[24] M.S. Daw. Model of metallic cohesion: The embedded-atom method. *Phys. Rev. B*, 39:7441–52, 1989.

[25] J.H. Rose, J.R. Smith, F. Guinea, and J. Ferrante. Universal features of the equation of state of metals. *Phys. Rev. B*, 29:2963–2969, 1984.

[26] D. Wolf. Reconstruction of NaCl surfaces from a dipolar solution to the Madelung problem. *Phys. Rev. Lett.*, 68:3315–3318, 1992.

[27] D. Wolf, P. Keblinski, S.R. Phillpot, and J. Eggebrecht. Exact method for the simulation of coulombic systems by spherically truncated, pairwise r^{-1} summation. *J. Chem. Phys.*, 110:8254–8282, 1999.

[28] C. Mundy. Private communication., 2001.

[29] M. Matsui. A transferable interatomic potential model for crystals and melts in the system CaO – MgO –Al_2O_3 – SiO_2. *Minerol. Mag.*, 58A:571–572, 1994.

[30] M. Matsui. Molecular dynamics simulation of structures, bulk moduli, and volume thermal expansivities of silicate liquids in the system CaO – MgO –Al_2O_3 – SiO_2. *Geophys. Res. Lett.*, 23:395–398, 1996.

[31] M. Wilson, P.A. Madden, N.C. Pyper, and J.H. Harding. Molecular dynamics simulations of compressible ions. *J. Chem. Phys.*, 104:8068–8081, 1996.

[32] R.J.E. Clausius. On a mechanical theorem applicable to heat. *Philosophical Magazine*, 40:122, 1870.

[33] J.C. Maxwell. On reciprocal figures, frames and diagrams of forces. *Transactions of the Royal Society Edinborough*, XXVI:1, 1870.

[34] K.S. Cheung, A.S. Argon, and S. Yip. Activation analysis of dislocation nucleation from crack tip in α-Fe. *J. Appl. Phys.*, 69:2088, 1991.

[35] C.L. Kelchner, S.J. Plimpton, and J.C. Hamilton. Dislocation nucleation and defect structure during surface indentation. *Phys. Rev. B*, 58:11085–8, 1998.

[36] L.H. Van Vlack. *Elements of Materials Science and Engineering.* Addison-Wesley Publishing Co., Massachusetts, 1980.

[37] R. W. Ogden. *Non-linear Elastic Deformations.* John Wiley and Sons, Inc., New York, 1984.

[38] J. E. Marsden and T. J. R. Hughes. *Mathematical Foundations of Elasticity.* Dover Publications, Inc., New York, 1983.

[39] M. Born. On the stability of crystals, I. *Proceedings of the Cambridge Philosophical Society*, 36:160–172, 1940.

[40] K. Huang. On the atomic theory of elasticity. *Proc. Roy. Soc. London*, A203:178–94, 1950.

[41] I. Stakgold. The Cauchy relations in a molecular theory of elasticity. *Quarterly of Applied Mechanics*, 8:169–186, 1950.

[42] M. Born and K. Huang. *Dynamical Theories of Crystal Lattices.* Clarendon Press, Oxford, 1956.

[43] R. Hill. On the elasticity and stability of perfect crystals at finite strain. *Mathematical Proceedings of the Cambridge Philosophical Society*, 77:225–240, 1975.

[44] R. Hill and F. Milstein. Principles of stability analysis of ideal crystals. *Physical Review B*, 15:3807–3096, 1977.

[45] F. Milstein and R. Hill. Theoretical properties of cubic crystals at arbitrary pressure—I. density and bulk modulus. *Journal of the Mechanics and Physics of Solids*, 25:457–477, 1977.

[46] F. Milstein and R. Hill. Theoretical properties of cubic crystals at arbitrary pressure—II. shear moduli. *Journal of the Mechanics and Physics of Solids*, 26:213–239, 1978.

[47] F. Milstein and R. Hill. Theoretical properties of cubic crystals at arbitrary pressure—III. stability. *Journal of the Mechanics and Physics of Solids*, 27:255–279, 1979.

[48] F. Milstein and K. Huang. Theory of the response of an FCC crystal to [110] uniaxial loading. *Physical Review B*, 18:2529–2541, 1978.

[49] F. Milstein, R. Hill, and K. Huang. Theory of the response of cubic crystals to [111] loading. *Physical Review B*, 21:4282–4291, 1980.

[50] F. Milstein and B. Farber. A theoretical FCC $\rightarrow$ BCC transition under [100] tensile loading. *Physics Review Letters*, 44:277–280, 1980.

[51] E.B. Tadmor, M. Ortiz, and R. Phillips. Quasicontinuum analysis of defects in solids. *Philosophical Magazine A*, 73:1529–1563, 1996.

[52] F. Ercolessi and J.B. Adams. Interatomic potentials from first-principles calculations: the force-matching method. *Europhysics Letters*, 28:583–588, 1994.

[53] J.H. Weiner. Hellmann-Feynman theorem, elastic moduli, and the Cauchy relation. *Physical Review B*, 24:845–848, 1981.

[54] F. Milstein. Review: theoretical elastic behavior at large strains. *Journal of Materials Science*, 15:1071–1084, 1980.

[55] R. Hill. Acceleration waves in solids. *Journal of the Mechanics and Physics of Solids*, 10:1–16, 1962.

[56] F. Milstein. Crystal elasticity. In H.G. Hopkins and M.J. Sewell, editors, *Mechanics of Solids*, pages 417–452. Pergamon Press, 1982.

[57] L.A. Girifalco and V.G. Weizer. Application of the Morse potential function to cubic metals. *Physical Review*, 114:687–690, 1959.

[58] M.I. Baskes. Modified embedded-atom potentials for cubic materials and impurities. *Physical Review B*, 46:2727–2741, 1992.

[59] M.I. Baskes and R.A. Johnson. Modified embedded atom potentials for HCP metals. *Modeling and Simulation in Materials Science and Engineering*, 2:147–163, 1994.

[60] A.F. Voter and S.P. Chen. Accurate interatomic potentials for Ni, Al, and Ni_3Al. In *Proceedings of the 1987 MRS Fall Symposium*, volume 82 of *Characterization of Defects in Materials*, pages 175–180. Materials Research Society, 1987.

[61] K.L. Johnson. *Contact Mechanics*. Cambridge University Press, New York, 1985.

[62] S.G. Corcoran, R.J. Colton, E.T. Lilleodden, and W.W. Gerberich. Anomalous plastic deformation at surfaces: Nanoindentation of gold single crystals. *Phys. Rev. B*, 55:R16057–60, 1997.

[63] J.D. Kiely and J.E. Houston. Nanomechanical properties of Au (111), (001), and (110) surfaces. *Phys. Rev. B*, 57:12588–94, 1998.

[64] J.D. Kiely, K.F. Jarausch, J.E. Houston, and P.E. Russell. Initial stages of yield in nanoindentation. *J. Mater. Res.*, 14:2219–27, 1999.

[65] J.D. Kiely, R.Q. Hwang, and J.E. Houston. Effect of surface steps on the plastic threshold in nanoindentation. *Phys. Rev. Lett.*, 81:4424–7, 1998.

[66] C.F. Robertson and M.C. Fivel. A study of submicron indent-induced plastic deformation. *J. Mater. Res.*, 14:2251–58, 1999.

[67] E.B. Tadmor, R. Miller, and R. Phillips. Nanoindentation and incipient plasticity. *J. Mater. Res.*, 14:2233–50, 1999.

[68] V.B. Shenoy, R. Phillips, and E.B. Tadmor. Nucleation of dislocations beneath a plane strain indenter. *J. Mech. Phys. Solids*, 48:649–73, 2000.

[69] S.J. Zhou, D.M. Beazley, P.S. Lomdahl, and B.L. Holian. Large-scale molecular dynamics simulations of three-dimensional ductile failure. *Phys. Rev. Lett.*, 78:479–482, 1997.

[70] Z. Liu, S.and Zhang, G. Comsa, and H. Metiu. Kinetic mechanism for island shape variations caused by changes in the growth temperature. *Phys. Rev. Lett.*, 71:2967–2970, 1993.

[71] J.P. Hirth and J. Lothe. *Theory of Dislocations*. Krieger Publishing Company, Malabar, Florida, 2nd edition, 1992.

[72] J.R. Rice. Dislocation nucleation from a crack tip: an analysis based on the Peierls concept. *J. Mech. Phys. Solids*, 40:239, 1992.

[73] J.A. Zimmerman. *Continuum and Atomistic Modeling of Dislocation Nucleation at Crystal Surface Ledges*. PhD thesis, Stanford University, 2000.

[74] J.A. Zimmerman, H. Gao, and F.F. Abraham. Generalized stacking fault energies for embedded atom FCC metals. *Modell. Sim. Mater. Sci. Eng.*, 8:103–115, 2000.

[75] T. Mura and H. Saka. *The Structure and Properties of Crystal Defects*. Elsevier, New York, 1983.

[76] Y.W. Zhang, T.C. Wang, and Q.H. Tang. The effect of thermal activation on dislocation processes at an atomistic crack tip. *J. Phys. D: Appl. Phys.*, 28:748, 1995.

[77] M. de Koning, A. Antonelli, M.Z. Bazant, E. Kaxiras, and J.F. Justo. Finite-temperature molecular-dynamics study of unstable stacking fault free energies in silicon. *Phys. Rev. B*, 58:12555–12558, 1998.

[78] D.L. Medlin, S.M. Foiles, and D. Cohen. A dislocation-based description of grain boundary dissociation: Application to a $90^o\langle 110\rangle$ tilt boundary in gold. *Acta Mater.*, 49:36893697, 2001.

[79] M.L. Jenkins. Measurement of the stacking-fault energy of gold using the weak-beam technique of electron microscopy. *Phil. Mag.*, 26:747, 1972.

[80] T.J. Balk and K.J. Hemker. High resolution transmission electron microscopy of dislocation core dissociations in gold and iridium. *Phil. Mag. A*, 81:1507–1531, 2001.

[81] The original potential used yields $\gamma_{sf} = 5$ mJ/m^2, while the one from [78] produces a value ≈ 31 mJ/m^2., 2001.

[82] S. Kohlhoff, P. Gumbsch, and H.F. Fischmeister. Crack propagation in BCC crystals studied with a combined finite-element and atomistic model. *Phil. Mag. A*, 64:851–78, 1991.

[83] J.Q. Broughton, F.F. Abraham, N. Bernstein, and E. Kaxiras. Concurrent coupling of length scales: Methodology and application. *Phys. Rev. B*, 60:2391–2403, 1999.

[84] R. Rodríguez de la Fuente, M.A. González, and J.M. Rojo. Dislocation configurations around nanoindentations in reconstructed Au(001). In *Fundamentals of Nanoindentation and Nanotribology II*, volume 649 of *Proceedings of the 2000 MRS Fall Symposium*. Materials Research Society, 2000.

[85] In terms of the thompson's tetrahedron notation,the perfect loop segment on the $\overline{a}$ plane would split in this plane under the reaction $\boldsymbol{CD} \rightarrow \boldsymbol{C\alpha} + \boldsymbol{\alpha D}$.the dissociation of both segments on the $\overline{a}$ and $\overline{b}$ planes, respectively, gives rise to the stacking faults intersecting at the stair-rod dislocation with burgers vector $\boldsymbol{\alpha\beta}$.

[86] P.B. Hirsch. *Electron microscopy of thin crystals*. Butterworths, London, 1965.

[87] The cell dimensions are 204 å × 204 å × 125 å with 300.000 atoms. the top surface is traction free, while the bottom is held fixed with periodic boundary conditions applied to the side surfaces.

[88] V. Fiorentini, M. Methfessel, and M. Scheffler. Reconstruction mechanism of FCC transition metal (001) surfaces. *Phys. Rev. Lett.*, 71:1051–1054, 1993.

[89] J. de la Figuera, K. Pohl, O. Rodríguez de la Fuente, A.K. Schmid, N.C. Bartelt, C.B. Carter, and R.Q. Hwang. Direct observation of misfit dislocation glide on surfaces. *Phys. Rev. Lett.*, 86:3819–3822, 2001.

[90] Z. Gai, Y. He, X. Li, J.F. Jia, and W.S. Yang. Application of Moire fringes in investigations of subsurface imperfections-a study of dislocations and strain fields under the reconstructed surface layer of Au(001) by scanning tunneling microscopy. *Surf. Sci.*, 365:96–102, 1996.

[91] O. Rodríguez de la Fuente, M.A. González, and J.M. Rojo. Ion bombardment of reconstructed metal surfaces: From two-dimensional dislocation dipoles to vacancy pits. *Phys. Rev. B*, 63:085420, 2001.

[92] R.F. Cook and G.M. Pharr. Direct observation and analysis of indentation cracking in glasses and ceramics. *J. Amer. Ceram. Soc.*, 73:787–817, 1990.

[93] E. Le Bourhis and D. Metayer. Indentation of glass as a function of temperature. *J. Non-Cryst. Sol.*, 272:34–38, 2000.

[94] J. Woirgard, C. Tromas, J.C. Girard, and V. Audurier. Study of the mechanical properties of ceramic materials by the nanoindentation technique. *J. Eur. Ceram. Soc.*, 18:2297–2305, 1998.

[95] M.M. Chaudhri and Y. Enomoto. In situ observations of indentation damage in single crystals of MgO. *Wear*, 233-235:717–726, 1999.

[96] C. Tromas, J. Colin, C. Coupeau, J.C. Girard, J. Woirgard, and J. Grilhé. Pop-in phenomenon during nanoindentation in MgO. *Eur. Phys. J. Appl. Phys.*, 8:123–128, 1999.

[97] K. Sangwal, P. Gorostiza, J. Servat, and F. Sanz. Atomic force microscopy study of nanoindentation deformation and indentation size effect in MgO crystals. *J. Mater. Res.*, 14:3973–3982, 1999.

[98] K. Higashida, N. Narita, S. Asano, and R. Onodera. Dislocation emission from a crack tip in MgO thin crystals. *Matls. Sci. & Engin. A*, A285:111–121, 2000.

[99] P.F.M. Terán Arce, G.A. Riera, P. Gorostiza, and F. Sanz. Atomic-layer expulsion in nanoindentations on an ionic single crystal. *App. Phys. Lett.*, 77:839–841, 2000.

[100] C. Tromas, J.C. Girard, and J. Woirgard. Study by atomic force microscopy of elementary deformation mechanisms involved in low load indentations in MgO crystals. *Phil. Mag. A.*, 80:2325–2335, 2000.

[101] K. Ravi-Chandar and W.G. Knauss. An experimental investigation into dynamic fracture: I. crack initiation and arrest. *International Journal of Fracture*, 25:247–262, 1984.

[102] K. Ravi-Chandar and W.G. Knauss. An experimental investigation into dynamic fracture: II. microstructural aspects. *International Journal of Fracture*, 26:65–80, 1984.

[103] K. Ravi-Chandar and W.G. Knauss. An experimental investigation into dynamic fracture: III. on steady state propagation and branching. *International Journal of Fracture*, 26:141–154, 1984.

[104] K. Ravi-Chandar and W.G. Knauss. An experimental investigation into dynamic fracture: IV. on the interaction of stress waves with propagating cracks. *International Journal of Fracture*, 26:189–200, 1984.

[105] J. Fineberg, S.P. Gross, M. Marder, and H.L. Swinney. Instability in dynamic fracture. *Physical Review Letters*, 67:457–460, 1991.

[106] J. Fineberg, S.P. Gross, M. Marder, and H.L. Swinney. Instability in the propagation of fast cracks. *Physical Review B*, 45:5146–5154, 1992.

[107] E.H. Yoffe. The moving Griffith crack. *Philosophical Magazine*, 42:739–750, 1951.

[108] B. Freund. *Dynamic Fracture Mechanics*. Cambridge University Press, New York, 1990.

[109] Liu X. and M. Marder. The energy of a steady-state crack in a strip. *Journal of the Mechanics and Physics of Solids*, 39:947–961, 1991.

[110] H. Gao. A theory of local limiting speed in dynamic fracture. *Journal of the Mechanics and Physics of Solids*, 44:1453–1474, 1996.

[111] V. Tvergaard and J.W. Hutchinson. The influence of plasticity on mixed mode interface toughness. *Journal of the Mechanics and Physics of Solids*, 41:1119–1135, 1993.

[112] P.A. Klein, J.W. Foulk, E.P. Chen, S.A. Wimmer, and H. Gao. Physics-based modeling of brittle fracture: cohesive formulations and the application of meshfree methods. Technical Report SAND2001 - 8099, Sandia National Laboratories, 2001.

[113] S. Tamura. Spontaneous decay rates of la phonons in quasi-isotropic solids. *Phys. Rev. B*, 31:2574, 1985.

[114] J.A. Shields and J.P. Wolfe. Measurement of a phonon hot spot in photoexcited si. *Z. Phys. B*, 75:11, 1989.

This page intentionally left blank.

Chapter 9

DISTRIBUTION:

1	MS 0188	D.L. Chavez, LDRD Office, 4001
1	MS 0310	G.S. Heffelfinger, 9209
1	MS 0316	J.B. Aidun, 9235
1		M.J. Stevens, 9235
1	MS 0841	T.C. Bickel, 9100
1	MS 0893	E.D. Reedy Jr., 9123
1	MS 1111	S.J. Plimpton, 9209
1	MS 1411	H.E. Fang, 1834
1		C.C. Battaile, 1834
1		S.M. Foiles, 1834
1		E.A. Holm, 1834
1		J.J. Hoyt, 1834
1		E.B. Webb III, 1834
5	MS 1415	J.E. Houston, 1114
1		P.J. Feibelman, 1114
1	MS 9001	M.E. John, 8000
		Attn:
		J. Vitko, 8100, MS 9004
		W.J. McLean, 8300, MS 9054
		D.R. Henson, 8400, MS 9007
		P.N. Smith, 8500, MS 9002
		K.E. Washington, 8900, MS 9003

1	MS 9042	B.R. Antoun, 8725
1	MS 9042	J.E. Robles, 8727
1		Y. Ohashi, 8727
1	MS 9108	S.L. Robinson, 8414
1		C.W. Pretzel, 8414
1		G.C. Story, 8414
1	MS 9161	E.P. Chen, 8726
1		R.E. Campbell, 8726
1		C.J. Kimmer, 8726
10		P.A. Klein, 8726
1		D.A. Zeigler, 8726
15		J.A. Zimmerman, 8726
1	MS 9161	J.C. Hamilton, 8721
1		D.L. Medlin, 8721
1		V. Ozolins, 8721
1	MS 9402	R.A. Causey, 8724
1		D.F. Cowgill, 8724
1		K.L. Hertz, 8724
1		B.P. Somerday, 8724
1	MS 9405	R.H. Stulen, 8700 Attn: R.Q. Hwang, 8721, MS 9161 K.L. Wilson, 8724, MS 9402 J.C.F. Wang, 8723, MS 9403 J.R. Garcia, 8725, MS 9042 J.L. Handrock, 8727, MS 9042 M.F. Horstemeyer, 8728, MS 9042 J.M. Hruby, 8702, MS 9401
1	MS 9404	S. Graham Jr., 8725
1		S.X. McFadden, 8725
1		N.R. Moody, 8725
1	MS 9405	S. Aubry, 8726
1		D.J. Bammann, 8726

1		A.A. Brown, 8726
1		J.W. Foulk, 8726
1		P.M. Gullett, 8726
1		Y. Hammi, 8726
1		D.A. Hughes, 8726
1		R.E. Jones, 8726
1		M.T. Lyttle, 8726
1		E.B. Marin, 8726
1		R.A. Regueiro, 8726
3	MS 9018	Central Technical Files, 8945-1
1	MS 0899	Technical Library, 9616
1	MS 9021	Classification Office, 8511/ Technical Library, MS 0899, 9616
1		DOE/OSTI via URL